5-2024

Domain Decomposition Methods for Fluid-Structure Interaction Problems Involving Elastic, Porous, or Poroelastic Structures

Hemanta Kunwar
hkunwar@clemson.edu

Domain Decomposition Methods for Fluid-Structure Interaction problems involving Elastic, Porous, or Poroelastic Structures

---

A Dissertation
Presented to
the Graduate School of
Clemson University

In Partial Fulfillment
of the Requirements for the Degree
Doctor of Philosophy
Mathematical and Statistical sciences

---

by
Hemanta Kunwar
May 2024

Accepted by:
Dr. Hyesuk Lee, Committee Chair
Dr. Qingshan Chen
Dr. Fei Xue
Dr. Shitao Liu

Abstract

We introduce two global-in-time domain decomposition methods, namely the Steklov-Poincare method and Schwarz waveform relaxation (SWR) method using Robin transmission conditions (or the Robin method), for solving fluid-structure interaction systems involving elastic, porous, or poroelastic structure. These methods allow us to formulate the coupled system as a space-time interface problem and apply iterative algorithms directly to the evolutionary problem. Each time-dependent fluid and the structure subdomain problem is solved independently, which enables the use of different time discretization schemes and time step sizes in the subsystems. This leads to an efficient way of simulating time-dependent multiphysics phenomena.

For the fluid-porous structure interaction system, we consider the SWR method. The coupled system is formulated as a time-dependent interface problem based on Robin-Robin transmission conditions, for which the decoupling SWR algorithm is proposed and proved for convergence. For the fluid-poroelastic structure interaction (FPSI) system, we use interface conditions to define Steklov-Poincare type operators. These operators are used to transform the coupled system into a non-linear space-time interface problem, which is then solved using a nested iteration algorithm. For the system that involves elastic structure, we implement both the Steklov-Poincare method and the SWR method.

Additionally, we present a temporal numerical discretization scheme for the interaction between a 3D fluid and a 2D plate structure. We show the stability of this scheme and propose a numerical algorithm that sequentially solves the fluid and plate subsystems through an effective decoupling approach. We perform numerical tests using P2Morley elements for the plate subproblem that involves the biharmonic operator.

Numerical tests are presented for both non-physical and physical problems with various mesh sizes and time step sizes to illustrate the accuracy and efficiency of the proposed methods.

Dedication

I dedicate this work to my daughter, **Hemanshi**, to my wife, **Santoshi**, who has been an incredible momma for Hemanshi, and to all those who supported us in raising our baby girl.

Acknowledgments

I would like to extend my heartfelt gratitude to Dr. Hyesuk Lee, my dedicated advisor, for her invaluable mentorship and support throughout my academic journey. Her guidance and encouragement have played a pivotal role in shaping my growth as a researcher. I am deeply thankful to Dr. Qingshan Chen, Dr. Fei Xue and Dr. Shitao Liu for being part of my dissertation committee and for providing valuable mentorship during my doctoral studies.

I am immensely grateful to my wife, Santoshi Pokharel Kunwar, for her unwavering belief in me and constant encouragement, which have been a source of strength throughout this journey. I am also indebted to my brothers, Dr. Ishwari J. Kunwar and Dr. Vijay J. Kunwar, whose passion for mathematics has inspired me greatly.

Special thanks to my parents, Bhesh Bahadur Kunwar and Amrita Devi Kunwar, my parents-in-law, Ram Chandra Pokharel and Sita Pokharel, and both of our families, for their endless support, love, and blessings. Additionally, I express my gratitude to Mr. Dhundiraj Pokharel and all my mathematics teachers for their role in shaping my mathematical expertise.

Table of Contents

Title Page . . . . . **i**

Abstract . . . . . **ii**

Dedication . . . . . **iii**

Acknowledgments . . . . . **iv**

List of Tables . . . . . **vii**

List of Figures . . . . . **ix**

1 Introduction **1**

I Fluid/Elastic Structure **7**

2 Model equations **8**
2.1 Weak formulation 10

3 Global-in-time domain decomposition schemes **12**
3.1 Time-dependent Steklov-Poincaré operator 12
3.2 Robin transmission conditions and the space-time interface problem 13
3.3 Schwarz waveform relaxation (SWR) algorithm and convergence analysis 15

4 Nonconforming time discretization **21**
4.1 Notation 21
4.2 Semi-discrete FSI system and discrete convergence analysis 22
4.3 Numerical results 27

II Fluid/Porous Structure **36**

5 Model Equations **37**
5.1 Function spaces and weak formulation 38

6 Global-in-time decoupling scheme **41**
6.1 Robin transmission conditions and the space-time interface problem 41
6.2 Schwarz waveform relaxation (SWR) algorithm and convergence analysis 43

7 The semi-discrete, nonconforming in time, SWR algorithm **50**
7.1 Notation 50

7.2 The semi-discrete Stokes-Darcy system and convergence analysis of SWR algorithm 51
7.3 Numerical results 57

III Fluid/Poroelastic Structure 65

8 Model equations 66
8.1 Function spaces and weak formulation 69

9 Space-time interface problem and nested iteration algorithm 71

10 Nonconforming discretization in time 74
10.1 Notation 74
10.2 The semi-discrete Stokes-Biot system 75
10.3 Numerical results 76

IV 3D Fluid/2D Plate interaction system 88

11 Model equations 89

12 Weak formulation and stability analysis 90

13 Second-order temporal discretization scheme 94

14 Working algorithm and Numerical results 98
14.1 Numerical results 100

15 Conclusions 106

Bibliography 108

List of Tables

4.1 Errors by the Steklov-Poincaré method using Taylor-Hood and $\mathbf{P}2$ elements, $\Delta t_f = 0.000025$ and $\Delta t_s = 0.000050$. 29
4.2 Errors by the Steklov-Poincaré method using MINI and $\mathbf{P}1$ elements, $\Delta t_f = 0.000025$ and $\Delta t_s = 0.000050$. 29
4.3 Errors by the Robin method ($\alpha_f = \alpha_s = 1$) using Taylor-Hood and $\mathbf{P}2$ elements, $\Delta t_f = 0.000050$, $\Delta t_s = 0.000025$. 29
4.4 Comparison of the computer running times (in seconds) of conforming and nonconforming time grids using Taylor-Hood and $\mathbf{P}2$ elements with $h = 1/32$. 30
4.5 Comparison of the computer running times (in seconds) of conforming and nonconforming time grids using MINI and $\mathbf{P}1$ elements with $h = 1/64$. 30
4.6 Number of GMRES iterations for $T = 0.2$ using $(\Delta t_f, \Delta t_s) = (0.025, 0.0125)$ and $\alpha_f = 1$. 30
4.7 Errors in the continuity of velocity between subsystems for $h_x = 0.1$cm. 35

7.1 Errors at $T = 0.01$ by Taylor-Hood elements for the Stokes and Darcy problems using $(\Delta t_f, \Delta t_p) = (0.002, 0.001)$ and $(\alpha_f, \alpha_p) = (0.1, 50)$. 58
7.2 Errors at $T = 0.01$ by MINI elements for the Stokes and RT1-P1 elements for Darcy problem using $(\Delta t_f, \Delta t_p) = (0.002, 0.001)$ and $(\alpha_f, \alpha_p) = (0.1, 50)$. 58
7.3 Comparison of the computer running times (in seconds) of conforming and nonconforming time grids with Taylor-Hood elements on fixed mesh $h = 1/32$ using $(\alpha_f, \alpha_p) = (0.1, 50)$. 60
7.4 Comparison of the computer running times (in seconds) of conforming and nonconforming time grids with MINI elements for the Stokes and RT1-P1 element for the Darcy problems on fixed mesh $h = 1/64$ using $(\alpha_f, \alpha_p) = (0.1, 50)$. 63
7.5 : Errors at $T = 1$ using $h = 1/64$ and $(\alpha_f, \alpha_p) = (0.1, 0.5)$. 63
7.6 : Errors for the Stokes problem at $T = 1$ using $h = 1/64$ and $(\alpha_f, \alpha_p) = (0.1, 0.5)$. . . 63
7.7 : Errors for the Darcy problem at $T = 1$ using $h = 1/64$ and $(\alpha_f, \alpha_p) = (0.1, 0.5)$. . . 63

10.1 Errors at $T = 0.0002$ by Taylorhood elements for the Stokes and $(\mathbf{P}_2, P_1, \mathbf{P}_2)$ for Biot problems using $(\Delta t_f, \Delta t_p) = (0.00002, 0.00001)$. 79
10.2 Physical parameters for the sensitivity analysis. 85
10.3 Comparison of the accumulated interface velocity errors in case I, II and III for $r_f = 1.5$. 85

14.1 Errors and convergence rates for $\mathbf{u}$ and p functions at final time $T_{\text{final}} = 0.01$ using time-step size $\Delta t = 0.001$ for different values of h. 101
14.2 Errors and convergence rates for w function at final time $T_{\text{final}} = 0.01$ using time-step size $\Delta t = 0.001$ for different values of h. 101
14.3 Flat errors for w function at final time $T_{\text{final}} = 0.2$ using mesh size $\frac{1}{12}$ using $\Delta t = \{0.2, 0.1, 0.05, 0.025\}$. 102

14.4 L^2 errors and convergence rates for w function at final time $T_{\text{final}} = 4$ using mesh size $\frac{1}{50}$ for different values of Δt while solving only 2D structure problem with weight 10^5. 102

List of Figures

2.1 Two-dimensional domain formed by FSI system 8

4.1 The fluid and structure domains 22
4.2 Nonconforming time grids 22
4.3 Projection of nonconforming time grids in two dimensions 22
4.4 Errors at $T = 0.2$ by the Steklov-Poincaré method using Taylor-Hood and $\mathbf{P}2$ elements with $h = 1/32$. 31
4.5 Errors at $T = 0.4$ by the Steklov-Poincaré method using MINI and $\mathbf{P}1$ elements with $h = 1/64$. 32
4.6 Errors at $T = 0.2$ by the Robin method ($\alpha_f = \alpha_s = 1$) using Taylor-Hood and $\mathbf{P}2$ elements with $h = 1/32$. 33
4.7 Domain and boundary conditions for Test2 34
4.8 Vertical displacement at three points on the interface with: (1) $h_x = 0.1$ cm, $h_y = 0.1$ cm, (2) $h_x = 0.1$ cm, $h_y = 0.05$ cm, and (3) $h_x = 0.1$ cm, $h_y = \frac{1}{30}$ cm 34

5.1 Stokes-Darcy domain 37

7.1 Nonconforming time grids. 51
7.2 Errors for the Stokes and Darcy problems at T = 0.2 by Taylor-Hood elements using $(\alpha_f, \alpha_p) = (0.1, 50)$. 60
7.3 Errors by MINI elements for the Stokes and RT1-P1 elements for the Darcy problems at $T = 0.8$ using $(\alpha_f, \alpha_p) = (0.1, 50)$. 61
7.4 H^{div} errors of Darcy velocity at T = 0.2 by Taylor-Hood elements using $\alpha_p = 50$ for different values of α_f. 61
7.5 H^{div} errors of Darcy velocity at T = 0.2 by Taylor-Hood elements using $\alpha_f = 0.1$ for different values of α_p. 62
7.6 H^{div} errors of Darcy velocity at T = 0.2 by Taylor-Hood elements using $\alpha_f = 0.001$ for different values of α_p. 62
7.7 [Test case 2] Velocity magnitude and velocity vector at T = 1 for $\nu_p = 50$. 64
7.8 [Test case 2] Velocity magnitude and velocity vector near interface at T = 1 for $\nu_p = 10^5$. 64

8.1 Fluid-poroelastic domain in $\mathbb{R}^2$ 66

10.1 Errors at $T = 0.2$ with Taylor-Hood elements for the Stokes and $(\mathbf{P}_2, P_1, \mathbf{P}_2)$ for the nonlinear Biot problem ($r_f = 1.5$). 80
10.2 Comparison of the computer running times (in seconds) of conforming and nonconforming time grids with Taylorhood elements for the Stokes and $(\mathbf{P}_2, P_1, \mathbf{P}_2)$ for linear (left) and nonlinear (right) Biot problems on fixed mesh $h = 1/32$. 81
10.3 Domain and boundary conditions for Test2 82
10.4 Pressure profiles at every 2 ms to visualize the propagation of an initial pressure pulse in a fluid (left) and poroelastic structure (right). 83

10.5 Vertical displacement of the fluid-structure interface at times 1.5 ms, 3.5 ms, and 4.5 ms from left to right. 83
10.6 Domain and boundary conditions for Test3 84
10.7 Velocities $\mathbf{u}_f$ and $\mathbf{u}_p + \partial_t \boldsymbol{\eta}$ (arrows) and their normal components (color) in their respective domains (left) and displacement profile in poroelastic structure (right) in case I, II and III respectively for $r_f = 2$. 86
10.8 Velocities $\mathbf{u}_f$ and $\mathbf{u}_p + \partial_t \boldsymbol{\eta}$ (arrows) and their normal components (color) in their respective domains (left) and displacement profile in poroelastic structure (right) in case I, II and III respectively for $r_f = 1.5$. 87

14.1 3D Fluid and 2D plate system domain in $\mathbb{R}^3$ 100
14.2 w_t-FEM (left) and w_t-Exact (right) for $h = 1/12$, $T_{\text{final}} = 0.01, \Delta t = 0.001$. 102
14.3 u_3-FEM (left) and u_3-Exact (right) for $h = 1/12$, $T_{\text{final}} = 0.01, \Delta t = 0.001$. 103
14.4 u_3 for $h = 1/12$, $T_{\text{final}} = 0.01, \tau = 0.001$ in $x = 0.5$ plane. 104
14.5 w_t(left) and u_3(right) for $h = 1/12$, $T_{\text{final}} = 0.01, \tau = 0.001$, $(m, n) = (1, 2)$ (top) and $(m, n) = (2, 2)$ (bottom). 105

Chapter 1

Introduction

Fluid-structure interaction (FSI) problems represent complex multiphysics phenomena that lie at the intersection of fluid dynamics and structural mechanics. The intricate interplay between these two disciplines gives rise to challenges and opportunities with far-reaching implications across diverse fields. Within FSI scenarios, the structures involved can exhibit a range of properties, including elasticity, porosity, or poroelasticity.

Modeling and applications In the FSI problems involving elastic structure, the fluid flow, and structure are coupled through the continuity of traction force and velocity on the interface. Such systems have a wide range of applications in various fields, including manufacturing, energy, aeroelasticity, defense, and biology [11, 17, 25, 34, 58, 62, 71, 91, 99]. In engineering, such models are considered in designing inkjet printers, blades for wind turbines, airplane wings, combustion chambers in engines, and offshore oil rigs. In biology, such systems are often considered in studying blood flow through vessels. Similarly, the FSI systems involving porous structure are modeled using Navier-Stokes (or Stokes)-Darcy system, where the Stokes equations represent an incompressible fluid and the Darcy equations represent a flow through a porous medium. Such models are often considered for studying groundwater flows problems [37, 39], filtration [93], flows in a vuggy porous medium [3, 4], and also for understanding impact of stream pollution in water supply [75] and other issues involving water contamination. In health sciences, the Stokes and Darcy equations are used to model filtrations involved in the pharmaceutical and chemical fields [57], biofluid-organ interactions or the movement of blood within vessels [36]. The interaction between free fluid and

a poroelastic structure is modeled using Stokes-Biot system and has a wide range of applications that include predicting gas and oil extraction from naturally or hydraulically fractured reservoirs, modeling groundwater flow, fluid flows through aquifers, blood flows through vessels, interfacial flow of aqueous humor and many more [24, 89, 87, 101, 50, 87].

Monolithic and decoupled schemes The FSI system is considered as a coupled monolithic system in [8, 60, 68, 81, 82]. In such an approach, the computational complexity arises from solving a large matrix system, necessitating the use of an efficient and suitable preconditioner for the discretized system [82]. An alternative approach involves decoupling the fluid and structure subsystems [6, 10, 15, 21, 20, 22, 43, 44, 73, 79, 88]. Implementing such methods, despite their advantages of using partitioned solvers and smaller matrices for each subsystem, can pose challenges in achieving efficient iteration between the two subsystems. The Stokes-Darcy system is studied as a coupled monolithic system in [3, 4, 57], and some decoupled algorithms are investigated in [14, 23, 26, 67, 94, 97]. Fully coupled approaches include the use of new finite element spaces [3, 4], Lagrange multiplier spaces [7, 42, 52, 75], or fully discontinuous approximations [95] to approximate the coupled Stokes-Darcy system. The FSI system involving poroelastic structure has been studied using a monolithic scheme in [2] where the Stokes equations are coupled with the quasi-static Biot system based on the Lagrange multiplier method. The proposed monolithic scheme was analyzed for stability and error estimation. A nonlinear Stokes-Biot system was considered for the analysis of well-posedness in [1], where stability and error estimates of its semi-discrete system were also proved. A coupled Navier-Stokes and Biot system was analyzed in [30] for the existence and stability of a weak solution under a small data assumption. Most decoupling strategies employ domain decomposition (DD) techniques to allow the use of optimized algorithms for the fluid and structure subproblems.

Classical domain decomposition(DD) methods There have been extensive studies on domain decomposition (DD) techniques for FSI involving elastic structure in the literature. Various approaches have been considered, including explicit schemes [22, 43] and semi-implicit schemes [10, 44, 92]. Many implicit DD methods have also been investigated for better stability of the numerical solution. For example, an implicit DD method based on optimization is considered in [88], for both linear and nonlinear elastic formulations for the structure. There, the stress force on the interface is used as a Neumann control, which is updated until the stress discontinuity on the

interface is sufficiently small, by enforcing the continuity of velocity through a Dirichlet boundary condition for the fluid subsystem. This process requires solving the subsystems in serial. Another optimization approach for FSI is explored in [73] by formulating the FSI problem as a least squares problem, where the jump in the velocities of the two substructures is minimized by a Neumann control enforcing the continuity of stress on the interface. In [98], the hybridizable discontinuous Galerkin (HDG) finite element method is used in the simulation of FSI. The coupling between an underlying incompressible fluid and an embedded solid is formulated through the overlapping domain decomposition method in conjunction with a mortar approach in [61]. A fictitious domain approach, where the fluid velocity and pressure are extended into the solid domain by introducing new unknowns, has been applied to study FSI in [6, 15, 79]. In [20] a splitting scheme based on Robin conditions is analyzed with an additional variable representing the structure velocity. However, the splitting method used in [20] does not discretize in space, giving several possibilities for spatial discretization. The splitting scheme utilizes a common Robin parameter is utilized for both fluid and structure sub-problems. This approach uses common time steps for the fluid and the structure sub-problems, and the loosely coupled subproblems are solved at each time step. For the stability analysis in the continuous case variable $\dot{\boldsymbol{\eta}}$ is introduced that represents the velocity of the fluid in the structure problem. In [21], the finite element approximation of the DD formulation introduced in [20] is analyzed, and an error estimate is derived for the fully discretized system. Loosely coupled schemes based on interface conditions of Robin type are also found in [54] for the time-discretized FSI system, where the choice of optimal Robin parameters is analyzed. The mortar space methods are considered in [14, 47, 51], where unmatched meshes on the interface and subdomains are used. Optimization-based DD methods are introduced in [41, 94], and two grid approaches are studied in [23, 85]. The boundary integral method and decoupled marching schemes are introduced in [16, 100] and [86], respectively. In [26, 33] DD methods using Robin-Robin conditions are discussed for the Stokes equations coupled with the Darcy equation in the primal form. There, iterative algorithms are analyzed for convergence and numerically tested with various Robin parameters. More DD works using Robin-Robin conditions for the stationary Stokes-Darcy system can be found in [38, 40, 49], where the decoupling schemes are based on the optimized Schwarz method. The non-stationary Stokes-Darcy problem is studied using the Crank–Nicolson method in [32]. Two parallel, non-iterative, multi-physics DD methods are proposed to solve a coupled time-dependent Stokes-Darcy system [27]. The FSI system involving poroelastic structures has also been studied

using various decoupling methods [9, 74, 19, 31, 103, 102, 56, 55]. Bukac et al. [19] have studied an explicit numerical algorithm based on an operator splitting approach for the interaction between a fluid and a multilayered poroelastic structure. In [31], a decoupling method was developed and analyzed for the Stokes-Biot system based on optimization. In that approach, the problem was formulated as a constrained optimization problem, and the first-order finite difference approximated the structure velocity in interface conditions. In [74], the second-order time discretization decoupling schemes were implemented in a nonlinear Stokes-Biot system. The fluid-poroelastic structure interaction (FPSI) system is studied by applying dual-mixed formulations in both fluid and structure domains in [28]. In this approach, the symmetry of the Stokes and poroelastic stress tensors is imposed by setting the vorticity and structure rotation tensors as auxiliary unknowns. The nonconforming Crouzeix–Raviart (C–R) element discretization is used for solving the stationary coupled Stokes–Biot flows in [104]. In [13], a staggered finite element procedure is developed for the coupling of a free viscous flow with a deformable porous medium, in which interface phenomena related to the skin effect can be incorporated. An augmented fully mixed formulation for the quasistatic Navier–Stokes–Biot model is studied in [77]. In [78], a mixed elasticity formulation is considered to study the FPSI system.

Motivation for global-in-time DD method In classical DD approaches for time-dependent problems, model equations are discretized in time first, and then DD methods are used at each time step. A uniform time step is usually considered in such approaches. Since the time scales in the fluid domain and structure domain could be largely different, it is inefficient to use a uniform time step throughout the entire time domain. Another approach used in some recent works for time-dependent problems is based on global-in-time or space-time DD methods in which iterative algorithms are directly applied to the evolutionary problem. Consequently, each time-dependent subdomain problem is solved independently, leading to an efficient way to simulate time-dependent phenomena as different time discretization schemes and time step sizes can be used in the subsystems. The space-time DD approach has been extensively investigated for the single physics porous medium flows (see [63, 65, 70] and the references therein) and recently studied for the Stokes-Darcy systems [66, 67]. In [67], a global-in-time DD method based on the physical transmission conditions is developed for the nonlinear Stokes-Darcy coupling. A time-dependent Steklov-Poincaré type operator was constructed, and non-matching time grids were implemented with the use of L^2 projection

functions to exchange data on the space-time interface between different time grids.

The content and structure of this Dissertation This dissertation mainly aims to study the global-in-time DD methods introduced in [67] for FSI systems using nonconforming time discretization. We consider two global-in-time domain decomposition methods [64], the Steklov-Poincare method and the Schwarz waveform relaxation (SWR) method based on Robin transmission conditions, also known as the Robin method.

In **part I** we study both global-in-time DD methods mentioned above for an FSI system with elastic structure using nonconforming time discretization. In the Steklov-Poincaré operator method, we introduce a Lagrange multiplier and derive the weak formulation of the fluid-structure system where one of the interface conditions is imposed through the use of a Lagrange multiplier. The remaining interface condition is used to define Steklov-Poincaré type operators that help in formulating a time-dependent interface problem which is solved using an iterative method. In the SWR method, the coupled system is formulated as a time-dependent interface problem based on Robin–Robin transmission conditions, for which the decoupling SWR algorithm is proposed and proved for convergence.

In **part II**, we study the SWR method with Robin transmission conditions, for the mixed formulation of the non-stationary Stokes-Darcy system using nonconforming time discretization. Similar to part I, the coupled system is formulated as a time-dependent interface problem based on Robin–Robin transmission conditions, for which the decoupling SWR algorithm is proposed and proved for convergence. Additionally, we discuss how the choice of the Robin coefficients affects the accuracy of numerical solutions in our numerical experiments. Further, we show that the problems with a large difference in local time scales, e.g., low permeability in the Darcy region, can be efficiently solved by the method under discussion.

In **part III**, we implement the Steklov-Poincare global-in-time domain decomposition approach to the FPSI system. We use interface conditions to define Steklov-Poincare type operators that transform coupled systems into a nonlinear space-time interface problem. Such a nonlinear space-time interface problem is then solved using a nested iteration algorithm. We present several computational experiments using a non-physical problem and problems from hemodynamic and geoscience applications to verify the convergence theory, illustrate the behavior of the method, and study the robustness of the method with respect to the physical parameters. It's worth highlighting that

the space-time domain decomposition approach is fully implicit in time, allowing for the utilization of not only different time steps but also significantly larger time step sizes without compromising stability.

Additionally, in **part IV**, we propose a temporal numerical discretization scheme for the 3D fluid - 2D plate structure interaction system. We show the stability of the scheme and propose a numerical algorithm that sequentially solves the fluid and plate subsystems through an effective decoupling strategy. The biharmonic operator within the plate model presents a numerical challenge that arises from the necessity of utilizing finite elements of class C^1 for accurate approximation. Such issues can be handled by either using mixed finite element methods or by using non-conforming methods using Morley elements [76, 83, 84]. We chose the latter by using $P2-$Morley elements[46] for the plate subproblem in all the numerical simulations. We perform the numerical experiments firstly using time-dependent manufactured solutions and secondly considering the free vibration of the plate to show the accuracy of the algorithm.

Finally, a conclusion is given summarizing the results of this dissertation and detailing future work and the areas that still need attention.

Part I

Fluid/Elastic Structure

Chapter 2

Model equations

The FSI problem involves coupling an incompressible Newtonian fluid with a linear elastic structure. To simplify the problem and conduct a rigorous analysis, we assume that the fluid is governed by the linear Stokes equations in a fixed domain. However, the proposed DD schemes can be extended to a nonlinear FSI system, as demonstrated in [67]. See Remark 3.1.1 for more details.

Suppose the domain under consideration comprises two bounded regions $\Omega_f, \Omega_s \in \mathbb{R}^d, d = 2, 3$, separated by the common interface Γ. See Figure 2.1. The free fluid occupies the first region Ω_f and has boundary $\partial\Gamma_f = \Gamma_f \cup \Gamma$. A saturated elastic structure occupies the second region Ω_s with the boundary $\partial\Gamma_s = \Gamma_s \cup \Gamma$.

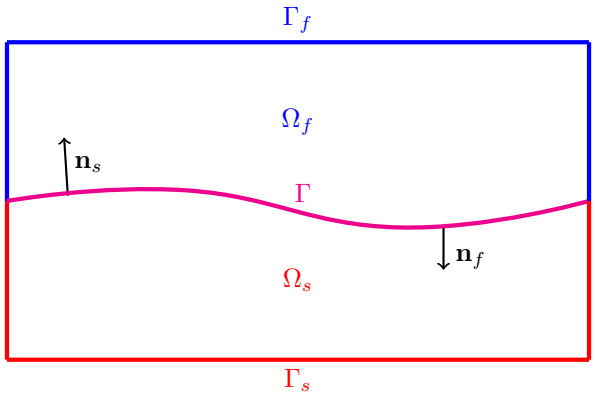

Figure 2.1: Two-dimensional domain formed by FSI system

Consider the fluid equations:

$$\begin{aligned}
\rho_f \partial_t \mathbf{u} - 2\nu_f \nabla \cdot D(\mathbf{u}) + \nabla p &= \mathbf{f}_f \quad \text{in } \Omega_f \times (0,T)\,, && (2.0.1)\\
\nabla \cdot \mathbf{u} &= 0 \quad \text{in } \Omega_f \times (0,T)\,, && (2.0.2)\\
\mathbf{u} &= \mathbf{0} \quad \text{in } \Gamma_f \times (0,T)\,, && (2.0.3)\\
\mathbf{u}(.,0) &= \mathbf{u}^0 \quad \text{in } \Omega_f, && (2.0.4)
\end{aligned}$$

where $\mathbf{u}$ denotes the velocity vector of the fluid, p the pressure of the fluid, ρ_f the density of the fluid, ν_f the fluid viscosity, and $\mathbf{f}_f$ the body force acting on the fluid. Here, $D(\mathbf{u})$ is the strain rate tensor

$$D(\mathbf{u}) = \frac{1}{2}\left(\nabla \mathbf{u} + (\nabla \mathbf{u})^T\right)$$

and the Cauchy stress tensor is given by

$$\boldsymbol{\sigma}_f = 2\nu_f\, D(\mathbf{u}) - p\mathbf{I}.$$

The equation (2.0.1) represents the conservation of linear momentum, while equation (2.0.2) represents the conservation of mass. The elastic system is represented by:

$$\begin{aligned}
\rho_s \partial_t^2 \boldsymbol{\eta} - 2\nu_s \nabla \cdot D(\boldsymbol{\eta}) - \lambda \nabla(\nabla \cdot \boldsymbol{\eta}) &= \mathbf{f}_s \quad \text{in } \Omega_s \times (0,T)\,, && (2.0.5)\\
\boldsymbol{\eta} &= \mathbf{0} \quad \text{in } \Gamma_s \times (0,T)\,, && (2.0.6)\\
\boldsymbol{\eta}(.,0) &= \boldsymbol{\eta}^0 \quad \text{in } \Omega_s\,, && (2.0.7)\\
\partial_t \boldsymbol{\eta}(.,0) &= \bar{\boldsymbol{\eta}}^0 \quad \text{in } \Omega_s\,, && (2.0.8)
\end{aligned}$$

where $\boldsymbol{\eta}$ is the displacement of the structure and $\mathbf{f}_s$ is the body force. The total stress tensor for the elastic structure is given by

$$\boldsymbol{\sigma}_s = 2\nu_s D(\boldsymbol{\eta}) + \lambda(\nabla \cdot \boldsymbol{\eta})\mathbf{I},$$

where ν_s and λ denote the Lamé constants. The density of the elastic structure is denoted by ρ_s.

The fluid and elastic models, (2.0.1)-(2.0.4) and (2.0.5)-(2.0.8), are coupled via the following

interface conditions:

$$\boldsymbol{\sigma}_f \mathbf{n}_f = -\boldsymbol{\sigma}_s \mathbf{n}_s \quad \text{on } \Gamma \times (0,T)\,, \tag{2.0.9}$$

$$\partial_t \boldsymbol{\eta} = \mathbf{u} \quad \text{on } \Gamma \times (0,T)\,, \tag{2.0.10}$$

where $\mathbf{n}_f$ and $\mathbf{n}_s$ denote outward unit normal vectors to Ω_f and Ω_s, respectively. These interface conditions suffice to precisely couple the Stokes system (2.0.1)-(2.0.4) to the structure system (2.0.5)-(2.0.8), imposing the balance of normal stresses and the continuity of velocity.

2.1 Weak formulation

To establish a weak formulation of the problem, we adopt standard notation for Sobolev spaces and their associated norms and seminorms. For $S \subset \mathbb{R}^d$, the norm for the Hilbert space $H^m(S)$ is denoted by $\|\cdot\|_{m,S}$. For $m = 0$, $(\cdot,\cdot)_S$ and $\|\cdot\|_S$ denote the inner product and the norm in $L^2(S)$ respectively. Moreover, if $S = \Omega_f$ or Ω_s, and the context is clear, S will be omitted, i.e., $(\cdot,\cdot) = (\cdot,\cdot)_{\Omega_f}$ or $(\cdot,\cdot)_{\Omega_s}$ for functions defined in Ω_f and Ω_s. For $F \subset \mathbb{R}^{d-1}$ such that $F \subset \partial\Omega_f \cap \partial\Omega_s$, we use $\langle\cdot,\cdot\rangle_F$ to denote the duality pairing between $H^{-1/2}(F)$ and $H^{1/2}(F)$.

Define the function spaces for the fluid velocity $\mathbf{u}$, the fluid pressure p, and the displacement $\boldsymbol{\eta}$ as

$$\begin{aligned}
\mathbf{X} &:= \{\mathbf{v} \in \mathbf{H}^1(\Omega_f) : \ \mathbf{v} = \mathbf{0} \quad \text{on } \Gamma_f\},\\
Q &:= L^2(\Omega_f),\\
\boldsymbol{\Sigma} &:= \{\boldsymbol{\xi} \in \mathbf{H}^1(\Omega_s) : \ \boldsymbol{\xi} = \mathbf{0} \quad \text{on } \Gamma_s\}.
\end{aligned}$$

We also define the *div-free* space for the fluid velocity,

$$\mathbf{V} := \{\mathbf{v} \in \mathbf{X} : (q, \nabla\cdot\mathbf{v}) = 0, \forall q \in Q\}\,.$$

The spaces $\mathbf{V}$ and Q satisfy the inf-sup condition,

$$\inf_{q\in Q} \sup_{\mathbf{v}\in\mathbf{V}} \frac{(q, \nabla\cdot\mathbf{v})}{\|q\|\|\nabla\mathbf{v}\|} \geq \beta > 0. \tag{2.1.1}$$

The variational formulation for the fluid-structure system (2.0.1)-(2.0.8) is given by: given the initial conditions, find $(\mathbf{u}, p, \boldsymbol{\eta}) \in (\mathbf{X}, Q, \boldsymbol{\Sigma})$, for a.e. $t \in (0, T)$, such that

$$\rho_f \left(\partial_t \mathbf{u},\, \mathbf{v}\right) + \left(2\nu_f D(\mathbf{u}), D(\mathbf{v})\right) - \left(p, \nabla \cdot \mathbf{v}\right)$$
$$= \left(\mathbf{f}_f, \mathbf{v}\right) + \left\langle \boldsymbol{\sigma}_f \mathbf{n}_f, \mathbf{v} \right\rangle_{\Gamma} \quad \forall \mathbf{v} \in \mathbf{X}\,, \tag{2.1.2}$$

$$\left(q, \nabla \cdot \mathbf{u}\right) = 0 \qquad \forall q \in Q\,, \tag{2.1.3}$$

$$\rho_s \left(\partial_t^2 \boldsymbol{\eta},\, \boldsymbol{\xi}\right) + 2\nu_s \left(D(\boldsymbol{\eta}), D(\boldsymbol{\xi})\right) + \lambda \left(\nabla \cdot \boldsymbol{\eta}, \nabla \cdot \boldsymbol{\xi}\right)$$
$$= \left(\mathbf{f}_s, \boldsymbol{\xi}\right) + \left\langle \boldsymbol{\sigma}_s \mathbf{n}_s, \boldsymbol{\xi} \right\rangle_{\Gamma} \quad \forall \boldsymbol{\xi} \in \boldsymbol{\Sigma}. \tag{2.1.4}$$

Chapter 3

Global-in-time domain decomposition schemes

This chapter discusses time-dependent interface problems for the fluid-structure system, from which global-in-time domain decomposition methods are developed.

3.1 Time-dependent Steklov-Poincaré operator

We introduce the Lagrange multiplier $\mathbf{g} \in \mathbf{\Lambda} := \mathbf{H}^{-1/2}(\Gamma)$ representing

$$\mathbf{g} := \boldsymbol{\sigma}_f \mathbf{n}_f = -\boldsymbol{\sigma}_s \mathbf{n}_s \quad \text{on } \Gamma \times (0,T)\,. \tag{3.1.1}$$

The equations (2.1.2)-(2.1.4) are then rewritten as

$$\begin{aligned} &\rho_f \left(\partial_t \mathbf{u},\, \mathbf{v}\right) + \left(2\nu_f D(\mathbf{u}), D(\mathbf{v})\right) - \left(p, \nabla \cdot \mathbf{v}\right) \\ &\qquad\qquad = \left(\mathbf{f}_f, \mathbf{v}\right) + \langle \mathbf{g}, \mathbf{v} \rangle_\Gamma \quad \forall \mathbf{v} \in \mathbf{X}\,, \end{aligned} \tag{3.1.2}$$

$$\left(q, \nabla \cdot \mathbf{u}\right) = 0 \qquad \forall q \in Q\,, \tag{3.1.3}$$

$$\begin{aligned} &\rho_s \left(\partial_t^2 \boldsymbol{\eta},\, \boldsymbol{\xi}\right) + 2\nu_s \left(D(\boldsymbol{\eta}), D(\boldsymbol{\xi})\right) + \lambda \left(\nabla \cdot \boldsymbol{\eta}, \nabla \cdot \boldsymbol{\xi}\right) \\ &\qquad\qquad = \left(\mathbf{f}_s, \boldsymbol{\xi}\right) - \langle \mathbf{g}, \boldsymbol{\xi} \rangle_\Gamma \quad \forall \boldsymbol{\xi} \in \mathbf{\Sigma}. \end{aligned} \tag{3.1.4}$$

Let $\mathbf{\Lambda}^*$ denote the dual space of $\mathbf{\Lambda}$ and define the following interface operators:

$$S_f : \mathbf{L}^2(0,T;\mathbf{\Lambda}) \longrightarrow \mathbf{L}^2(0,T;\mathbf{\Lambda}^*), \quad S_f(\mathbf{g}) = \mathbf{u}(\mathbf{g})|_\Gamma \,,$$

$$S_s : \mathbf{L}^2(0,T;\mathbf{\Lambda}) \longrightarrow \mathbf{L}^2(0,T;\mathbf{\Lambda}^*), \quad S_s(\mathbf{g}) = -\frac{\partial \boldsymbol{\eta}(\mathbf{g})}{\partial t}|_\Gamma,$$

where $\mathbf{u}(\mathbf{g})$ and $\boldsymbol{\eta}(\mathbf{g})$ are the solutions to the Stokes problem (3.1.2)-(3.1.3) and the structure problem (3.1.4). In (3.1.2)-(3.1.4), the interface condition (2.0.9) has been imposed through the use of a common $\mathbf{g}$, however, the interface condition (2.0.10) is not enforced. Therefore, the remaining condition (2.0.10) leads to the following time-dependent interface problem:
for a.e $t \in (0,T)$, *find* $\mathbf{g}(t) \in \mathbf{L}^2(0,T,\mathbf{\Lambda})$ *satisfying*

$$\int_0^T \big(\langle S_f(\mathbf{g}), \mathbf{v}\rangle + \langle S_s(\mathbf{g}), \mathbf{v}\rangle\big)\, ds = 0 \quad \forall\, \mathbf{v} \in \mathbf{L}^2(0,T,\mathbf{\Lambda}). \tag{3.1.5}$$

The evolutionary interface problem (3.1.5) can be solved using iterative methods, e.g., a Krylov method.

Remark 3.1.1. *If the nonlinear Stokes or the Navier-Stokes equations are considered for the FSI system, the interface operator is nonlinear, and an iteration formula for the nonlinear problem is defined using the linearized fluid equations. See [67].*

3.2 Robin transmission conditions and the space-time interface problem

The two-sided Robin interface conditions on Γ are established by linearly combining equations (2.0.9) and (2.0.10) with coefficients of $(\alpha_f, 1)$ and $(-\alpha_s, 1)$, respectively, where $\alpha_f, \alpha_s > 0$ [54]:

$$\mathbf{g}_f := \alpha_f \mathbf{u} + \boldsymbol{\sigma}_f \mathbf{n}_f = \alpha_f \partial_t \boldsymbol{\eta} - \boldsymbol{\sigma}_s \mathbf{n}_s \,, \tag{3.2.1}$$

$$\mathbf{g}_s := -\alpha_s \partial_t \boldsymbol{\eta} - \boldsymbol{\sigma}_s \mathbf{n}_s = -\alpha_s \mathbf{u} + \boldsymbol{\sigma}_f \mathbf{n}_f \,. \tag{3.2.2}$$

Assume that $\mathbf{g}_f$ and $\mathbf{g}_s$ have the L^2-regularity in space, to define an interface operator for the variables and analyze the DD algorithm discussed later in this section. If we let $\mathbf{g}_f$ be a Robin

condition for the Stokes equations with the parameter $\alpha_f > 0$ as in the left-hand side of (3.2.1), the corresponding weak formulation is given as follows: find $(\mathbf{u}, p) \in (\mathbf{X}, Q)$, for a.e. $t \in (0, T)$, such that

$$\rho_f(\partial_t \mathbf{u}, \mathbf{v}) + 2\nu_f(D(\mathbf{u}), D(\mathbf{v})) - (p, \nabla \cdot \mathbf{v}) \\ +\alpha_f(\mathbf{u}, \mathbf{v})_\Gamma \;=\; (\mathbf{f}_f, \mathbf{v}) + (\mathbf{g}_f, \mathbf{v})_\Gamma \quad \forall \mathbf{v} \in \mathbf{X}\,, \tag{3.2.3}$$

$$(q, (\nabla \cdot \mathbf{u}) \;=\; 0 \quad \forall q \in Q\,. \tag{3.2.4}$$

Similarly, considering $\mathbf{g}_s$ as a Robin condition for the elastic system with the parameter $\alpha_s > 0$ as in (3.2.2), we have the weak formulation given by: find $\boldsymbol{\eta} \in \boldsymbol{\Sigma}$, for a.e. $t \in (0, T)$ satisfying

$$\rho_s \left(\partial_t^2 \boldsymbol{\eta}, \boldsymbol{\xi}\right) + 2\nu_s(D(\boldsymbol{\eta}), D(\boldsymbol{\xi})) + \lambda(\nabla \cdot \boldsymbol{\eta}, \nabla \cdot \boldsymbol{\xi}) + \alpha_s(\partial_t \boldsymbol{\eta}, \boldsymbol{\xi})_\Gamma \\ = (\mathbf{f}_s, \boldsymbol{\xi}) - (\mathbf{g}_s, \boldsymbol{\xi})_\Gamma, \quad \forall \boldsymbol{\xi} \in \boldsymbol{\Sigma}. \tag{3.2.5}$$

Denote by $(\mathbf{u}, p) = \big(\mathbf{u}(\mathbf{g}_f, \mathbf{f}_f, \mathbf{u}_0), p(\mathbf{g}_f, \mathbf{f}_f, \mathbf{u}_0)\big)$ the solution to the Stokes problem (3.2.3)-(3.2.4), and $\boldsymbol{\eta} = \boldsymbol{\eta}(\mathbf{g}_s, \mathbf{f}_s, \boldsymbol{\eta}_0, \bar{\boldsymbol{\eta}}^0)$ the solution to the structure problem (3.2.5). To derive the interface problem associated with the Robin conditions (3.2.1)-(3.2.2), we first define the interface operator:

$$\mathcal{R} : \Big(L^2(0, T; \mathbf{L}^2(\Gamma))\Big)^2 \to \Big(L^2(0, T; \mathbf{L}^2(\Gamma))\Big)^2,$$

such that

$$\mathcal{R} \begin{bmatrix} \mathbf{g}_f \\ \mathbf{g}_s \end{bmatrix} = \begin{bmatrix} \mathbf{g}_s + (\alpha_s + \alpha_f) \left(\partial_t \boldsymbol{\eta}(\mathbf{g}_s, \mathbf{f}_s, \boldsymbol{\eta}_0, \bar{\boldsymbol{\eta}}_0)\right) |_\Gamma \\ \mathbf{g}_f - (\alpha_f + \alpha_s) \left(\mathbf{u}(\mathbf{g}_f, \mathbf{f}_f, \mathbf{u}_0)\right) |_\Gamma \end{bmatrix}. \tag{3.2.6}$$

The Robin transmission conditions (3.2.1)-(3.2.2) are then equivalent to the following space-time interface problem for two interface variables $\mathbf{g}_f$ and $\mathbf{g}_s$:

$$\mathcal{S}_\mathcal{R} \begin{bmatrix} \mathbf{g}_f \\ \mathbf{g}_s \end{bmatrix} = \chi_\mathcal{R} \quad \text{on } \Gamma \times (0, T), \tag{3.2.7}$$

where

$$\mathcal{S}_{\mathcal{R}} \begin{bmatrix} \mathbf{g}_f \\ \mathbf{g}_s \end{bmatrix} = \begin{bmatrix} \mathbf{g}_f \\ \mathbf{g}_s \end{bmatrix} - \begin{bmatrix} \mathbf{g}_s + (\alpha_s + \alpha_f)\left(\partial_t \boldsymbol{\eta}(\mathbf{g}_s, \mathbf{0}, \mathbf{0}, \mathbf{0})\right)|_\Gamma \\ \mathbf{g}_f - (\alpha_f + \alpha_s)\left(\mathbf{u}(\mathbf{g}_f, \mathbf{0}, \mathbf{0})\right)|_\Gamma \end{bmatrix}$$

and

$$\chi_{\mathcal{R}} = \begin{bmatrix} (\alpha_s + \alpha_f)\left(\partial_t \boldsymbol{\eta}(\mathbf{0}, \mathbf{f}_s, \boldsymbol{\eta}_0, \bar{\boldsymbol{\eta}}_0)\right)|_\Gamma \\ -(\alpha_f + \alpha_s)\left(\mathbf{u}(\mathbf{0}, \mathbf{f}_f, \mathbf{u}_0)\right)|_\Gamma \end{bmatrix}.$$

The weak form of (3.2.7) reads as: find $(\mathbf{g}_f, \mathbf{g}_s) \in \left(L^2(0,T;\mathbf{L}^2(\Gamma))\right)^2$, for a.e. $t \in (0,T)$, such that

$$\int_0^T \int_\Gamma \left(\mathcal{S}_{\mathcal{R}} \begin{bmatrix} \mathbf{g}_f \\ \mathbf{g}_s \end{bmatrix} \cdot \begin{bmatrix} \boldsymbol{\xi}_f \\ \boldsymbol{\xi}_s \end{bmatrix} \right) d\gamma\, dt = \int_0^T \int_\Gamma \left(\chi_{\mathcal{R}} \cdot \begin{bmatrix} \boldsymbol{\xi}_f \\ \boldsymbol{\xi}_p \end{bmatrix} \right) d\gamma\, dt \tag{3.2.8}$$

$\forall \left(\boldsymbol{\xi}_f, \boldsymbol{\xi}_p\right) \in \left(L^2(0,T;\mathbf{L}^2(\Gamma))\right)^2$.

The interface problem (3.2.8) is solvable by iterative methods such as GMRES and simple Jacobi-type methods. We consider a Schwarz waveform relaxation (SWR) algorithm based on Robin transmission conditions and show the convergence of the algorithm.

3.3 Schwarz waveform relaxation (SWR) algorithm and convergence analysis

Consider the following SWR algorithm based on Robin transmission conditions: at the kth iteration step we solve

$$\rho_f \partial_t \mathbf{u}^k - \nabla \cdot (2\nu_f D(\mathbf{u}^k) - p^k \mathbf{I}) = \mathbf{f}_f \quad \text{in } \Omega_f \times (0,T)\,, \tag{3.3.1}$$

$$\nabla \cdot \mathbf{u}^k = 0 \quad \text{in } \Omega_f \times (0,T)\,, \tag{3.3.2}$$

$$\alpha_f \mathbf{u}^k + \boldsymbol{\sigma}_f^k \mathbf{n}_f = \alpha_f \partial_t \boldsymbol{\eta}^{k-1} - \boldsymbol{\sigma}_s^{k-1} \mathbf{n}_s \quad \text{on } \Gamma \times (0,T)\,, \tag{3.3.3}$$

for $(\mathbf{u}^k, p^k)$ satisfying the initial and boundary conditions (2.0.4), (2.0.3), and

$$\rho_s \partial_t^2 \boldsymbol{\eta}^k - 2\nu_s \nabla \cdot D(\boldsymbol{\eta}^k) - \lambda \nabla(\nabla \cdot \boldsymbol{\eta}^k) = \mathbf{f}_s^k \quad \text{in } \Omega_s \times (0,T)\,, \tag{3.3.4}$$

$$-\alpha_s \partial_t \boldsymbol{\eta}^k - \boldsymbol{\sigma}_s^k \mathbf{n}_s = -\alpha_s \mathbf{u}^{k-1} + \boldsymbol{\sigma}_f^{k-1} \mathbf{n}_f \quad \text{on } \Gamma \times (0,T) \tag{3.3.5}$$

for $\boldsymbol{\eta}^k$ satisfying (2.0.6)-(2.0.8). The weak formulation of this decoupled system is written as: at the kth iteration, find $(\mathbf{u}^k, p^k, \boldsymbol{\eta}^k) \in (\mathbf{X}, Q, \boldsymbol{\Sigma})$, for a.e. $t \in (0,T)$, such that

$$\begin{aligned}\rho_f \left(\partial_t \mathbf{u}^k,\, \mathbf{v}\right) + (2\nu_f D(\mathbf{u}^k), D(\mathbf{v})) - (p^k, \nabla\cdot\mathbf{v}) + \alpha_f(\mathbf{u}^k, \mathbf{v})_\Gamma \\ = (\mathbf{f}_f, \mathbf{v}) + \left(\alpha_f \partial_t \boldsymbol{\eta}^{k-1} - \boldsymbol{\sigma}_s^{k-1}\mathbf{n}_s, \mathbf{v}\right)_\Gamma \qquad \forall \mathbf{v} \in \mathbf{X}\,, \end{aligned} \tag{3.3.6}$$

$$(q, \nabla\cdot\mathbf{u}^k) = 0 \qquad \forall q \in Q\,, \tag{3.3.7}$$

$$\begin{aligned}\rho_s \left(\partial_t^2 \boldsymbol{\eta}^k,\, \boldsymbol{\xi}\right) + 2\nu_s(D(\boldsymbol{\eta}^k), D(\boldsymbol{\xi})) + \lambda(\nabla\cdot\boldsymbol{\eta}^k, \nabla\cdot\boldsymbol{\xi}) + \alpha_s(\partial_t\boldsymbol{\eta}^k, \boldsymbol{\xi})_\Gamma \\ = (\mathbf{f}_s, \boldsymbol{\xi}) - (-\alpha_s \mathbf{u}^{k-1} + \boldsymbol{\sigma}_f^{k-1}\mathbf{n}_f, \boldsymbol{\xi})_\Gamma, \quad \forall \boldsymbol{\xi} \in \boldsymbol{\Sigma}. \end{aligned} \tag{3.3.8}$$

In the next theorem, we prove the convergence of the proposed algorithm.

Theorem 3.3.1. *Suppose $\mathbf{f}_f \in \boldsymbol{X}^*$, $\mathbf{f}_s \in \boldsymbol{\Sigma}^*$ and $\alpha_s \geq \alpha_f > 0$. If an initial $(\mathbf{u}^0, \boldsymbol{\eta}^0, \bar{\boldsymbol{\eta}}^0)$ is chosen such that the Robin-Robin conditions (3.2.1), (3.2.2) are well-defined in $\mathbf{L}^2(\Gamma)$ for a.e. $t \in (0,T)$, then the weak formulation (3.3.6)-(3.3.8) generates a convergent sequence of iterates*

$$(\mathbf{u}^k, \boldsymbol{\eta}^k) \in L^\infty(0,T;\boldsymbol{X}) \times L^\infty(0,T;\boldsymbol{\Sigma}).$$

With an additional regularity assumption for $\boldsymbol{\sigma}_s\mathbf{n}_s$ the pressure p^k also converges in $L^2(0,T;Q)$.

Proof. Since the equations (3.3.6)-(3.3.8) are linear, we show that the iterate $(\mathbf{u}^k, p^k, \boldsymbol{\eta}^k)$ converges to zero in suitable norms by setting $\mathbf{f}_f = \mathbf{u}^0 = \mathbf{0}$ and $\mathbf{f}_s = \boldsymbol{\eta}^0 = \bar{\boldsymbol{\eta}}^0 = \mathbf{0}$. Taking $\mathbf{v} = \mathbf{u}^k$ and $q = p^k$ in (3.3.6) and (3.3.7), we get

$$\begin{aligned}\rho_f \left(\partial_t \mathbf{u}^k,\, \mathbf{u}^k\right) + (2\nu_f D(\mathbf{u}^k), D(\mathbf{u}^k)) + \alpha_f(\mathbf{u}^k, \mathbf{u}^k)_\Gamma \\ = \left(\alpha_f \partial_t \boldsymbol{\eta}^{k-1} - \boldsymbol{\sigma}_s^{k-1}\mathbf{n}_s, \mathbf{u}^k\right)_\Gamma. \end{aligned} \tag{3.3.9}$$

Using the identity

$$(\boldsymbol{\sigma}_f^k\mathbf{n}_f + \alpha_f\mathbf{u}^k)^2 - (\boldsymbol{\sigma}_f^k\mathbf{n}_f - \alpha_s\mathbf{u}^k)^2 = 2(\alpha_f + \alpha_s)(\boldsymbol{\sigma}_f^k\mathbf{n}_f)(\mathbf{u}^k) + (\alpha_f^2 - \alpha_s^2)(\mathbf{u}^k)^2 \tag{3.3.10}$$

and the Robin condition (3.3.3), we can rewrite (3.3.9) as

$$\begin{aligned}
&\rho_f \left(\partial_t \mathbf{u}^k,\, \mathbf{u}^k\right) + 2\nu_f \left\| D(\mathbf{u}^k)\right\|_{\Omega_f}^2 + \frac{1}{2(\alpha_f+\alpha_s)} \int_\Gamma (\boldsymbol{\sigma}_f^k \mathbf{n}_f - \alpha_s \mathbf{u}^k)^2 \, d\gamma \\
&\quad = \frac{1}{2(\alpha_f+\alpha_s)} \int_\Gamma (\boldsymbol{\sigma}_f^k \mathbf{n}_f + \alpha_f \mathbf{u}^k)^2 \, d\gamma + \frac{1}{2}(\alpha_s - \alpha_f) \int_\Gamma (\mathbf{u}^k)^2 \, d\gamma \\
&\quad = \frac{1}{2(\alpha_f+\alpha_s)} \int_\Gamma (-\boldsymbol{\sigma}_s^{k-1} \mathbf{n}_s + \alpha_f \partial_t \boldsymbol{\eta}^{k-1})^2 \, d\gamma + \frac{1}{2}(\alpha_s - \alpha_f) \int_\Gamma (\mathbf{u}^k)^2 \, d\gamma. \qquad (3.3.11)
\end{aligned}$$

We then integrate over $(0,t)$ for a.e. $t \in (0,T]$. And, since $\mathbf{u}^k \in \mathbf{H}^1(\Omega_f)$, apply the trace theorem and Young's inequality to obtain,

$$\begin{aligned}
&\frac{\rho_f}{2} \left\|\mathbf{u}^k\right\|_{\Omega_f}^2 + 2\nu_f \int_0^t \left\| D(\mathbf{u}^k)\right\|_{\Omega_f}^2 ds + \frac{1}{2(\alpha_f+\alpha_s)} \int_0^t \int_\Gamma (\boldsymbol{\sigma}_f^k \mathbf{n}_f - \alpha_s \mathbf{u}^k)^2 d\gamma \, ds \\
&\leq \frac{1}{2(\alpha_f+\alpha_s)} \int_0^t \int_\Gamma (-\boldsymbol{\sigma}_s^{k-1} \mathbf{n}_s + \alpha_f \partial_t \boldsymbol{\eta}^{k-1})^2 d\gamma \, ds + \overline{C} \int_0^t \left\|\mathbf{u}^k(s)\right\|_{\Omega_f} \left\| D(\mathbf{u}^k(s))\right\|_{\Omega_f} d\gamma \, ds \\
&\leq \frac{1}{2(\alpha_f+\alpha_s)} \int_0^t \int_\Gamma (-\boldsymbol{\sigma}_s^{k-1} \mathbf{n}_s + \alpha_f \partial_t \boldsymbol{\eta}^{k-1})^2 d\gamma \, ds \\
&\qquad + \overline{C} \int_0^t \left(\frac{1}{4\epsilon} \left\|\mathbf{u}^k(s)\right\|_{\Omega_f}^2 + \epsilon \left\| D(\mathbf{u}^k(s))\right\|_{\Omega_f}^2 \right) ds \qquad (3.3.12)
\end{aligned}$$

for some constant $\overline{C} > 0$ and $\epsilon > 0$. Choosing $\epsilon = \nu_f / \overline{C}$, we have

$$\begin{aligned}
&\frac{\rho_f}{2} \left\|\mathbf{u}^k\right\|_{\Omega_f}^2 + \nu_f \int_0^t \left\| D(\mathbf{u}^k)\right\|_{\Omega_f}^2 ds + \frac{1}{2(\alpha_f+\alpha_s)} \int_0^t \int_\Gamma (\boldsymbol{\sigma}_f^k \mathbf{n}_f - \alpha_s \mathbf{u}^k)^2 d\gamma \, ds \\
&\leq \frac{1}{2(\alpha_f+\alpha_s)} \int_0^t \int_\Gamma (-\boldsymbol{\sigma}_s^{k-1} \mathbf{n}_s + \alpha_f \partial_t \boldsymbol{\eta}^{k-1})^2 d\gamma \, ds + C \int_0^t \left\|\mathbf{u}^k(s)\right\|_{\Omega_f}^2 ds, \qquad (3.3.13)
\end{aligned}$$

where $C = \overline{C}^2/(4\nu_f)$. Now, similarly for the structure part, taking $\boldsymbol{\xi} = \partial_t \boldsymbol{\eta}^k$ in (3.3.8),

$$\begin{aligned}
&\rho_s \left(\partial_t^2 \boldsymbol{\eta}^k,\, \partial_t \boldsymbol{\eta}^k\right) + 2\nu_s (D(\boldsymbol{\eta}^k), D(\partial_t \boldsymbol{\eta}^k)) + \lambda (\nabla \cdot \boldsymbol{\eta}^k, \nabla \cdot \partial_t \boldsymbol{\eta}^k) + \alpha_s (\partial_t \boldsymbol{\eta}^k, \partial \boldsymbol{\eta}^k)_\Gamma \\
&\qquad = -(-\alpha_s \mathbf{u}^{k-1} + \boldsymbol{\sigma}_f^{k-1} \mathbf{n}_f, \partial_t \boldsymbol{\eta}^k)_\Gamma. \qquad (3.3.14)
\end{aligned}$$

Using the identity

$$(-\boldsymbol{\sigma}_s^k \mathbf{n}_s - \alpha_s \partial_t \boldsymbol{\eta}^k)^2 - (-\boldsymbol{\sigma}_s^k \mathbf{n}_s + \alpha_f \partial_t \boldsymbol{\eta}^k)^2 = 2(\alpha_f + \alpha_s)(\boldsymbol{\sigma}_s^k \mathbf{n}_s)(\partial_t \boldsymbol{\eta}^k) + (\alpha_s^2 - \alpha_f^2)(\partial_t \boldsymbol{\eta}^k)^2 \quad (3.3.15)$$

and the Robin condition (3.3.5), (3.3.14) implies

$$\begin{aligned}
&\rho_s\left(\partial_t^2\boldsymbol{\eta}^k,\,\partial_t\boldsymbol{\eta}^k\right)+2\nu_s(D(\boldsymbol{\eta}^k),\partial_t D(\boldsymbol{\eta}^k))+\lambda(\nabla\cdot\boldsymbol{\eta}^k,\partial_t\nabla\cdot\boldsymbol{\eta}^k)\\
&+\frac{\alpha_s-\alpha_f}{2}\int_\Gamma(\partial_t\boldsymbol{\eta}^k)^2\,d\gamma+\frac{1}{2(\alpha_f+\alpha_s)}\int_\Gamma(-\boldsymbol{\sigma}_s^k\mathbf{n}_s+\alpha_f\partial_t\boldsymbol{\eta}^k)^2\,d\gamma\\
&\qquad\le\frac{1}{2(\alpha_f+\alpha_s)}\int_\Gamma(-\boldsymbol{\sigma}_s^k\mathbf{n}_s-\alpha_s\partial_t\boldsymbol{\eta}^k)^2\,d\gamma. \qquad (3.3.16)
\end{aligned}$$

Integrate over $(0,t)$ for a.e. $t\in(0,T)$ and apply the Robin boundary conditions (3.3.5) to obtain

$$\begin{aligned}
&\frac{\rho_s}{2}\left\|\partial_t\boldsymbol{\eta}^k\right\|_{\Omega_s}^2+\nu_s\left\|D(\boldsymbol{\eta}^k)\right\|_{\Omega_s}^2+\frac{\lambda}{2}\left\|\nabla\cdot\boldsymbol{\eta}^k\right\|_{\Omega_s}^2+\frac{\alpha_s-\alpha_f}{2}\int_0^t\left\|\partial_t\boldsymbol{\eta}^k\right\|_\Gamma^2\,ds\\
&\qquad+\frac{1}{2(\alpha_f+\alpha_s)}\int_0^t\int_\Gamma(-\boldsymbol{\sigma}_s^k\mathbf{n}_s+\alpha_f\partial_t\boldsymbol{\eta}^k)^2\,d\gamma\,ds\\
&\qquad\le\frac{1}{2(\alpha_f+\alpha_s)}\int_0^t\int_\Gamma(\boldsymbol{\sigma}_f^{k-1}\mathbf{n}_f-\alpha_s\mathbf{u}^{k-1})^2\,d\gamma\,ds. \qquad (3.3.17)
\end{aligned}$$

Define, for all $k\ge1$ and for a.e. $t\in(0,T]$,

$$\begin{aligned}
E^k(t)\;&:=\;\frac{\rho_f}{2}\left\|\mathbf{u}^k(t)\right\|_{\Omega_f}^2+\nu_f\int_0^t\left\|D(\mathbf{u}^k)\right\|_{\Omega_f}^2\,ds+\frac{\rho_s}{2}\left\|\partial_t\boldsymbol{\eta}^k\right\|_{\Omega_s}^2\\
&\quad+\nu_s\left\|D(\boldsymbol{\eta}^k)\right\|_{\Omega_s}^2+\frac{\lambda}{2}\left\|\nabla\cdot\boldsymbol{\eta}^k\right\|_{\Omega_s}^2+\frac{\alpha_s-\alpha_f}{2}\int_0^t\left\|\partial_t\boldsymbol{\eta}^k\right\|_\Gamma^2 ds,\\
B^k(t)\;&:=\;\frac{1}{2(\alpha_f+\alpha_s)}\int_0^t\left\|\boldsymbol{\sigma}_f^k\mathbf{n}_f-\alpha_s\mathbf{u}^k\right\|_\Gamma^2\,ds\\
&\quad+\frac{1}{2(\alpha_f+\alpha_s)}\int_0^t\left\|-\boldsymbol{\sigma}_s^k\mathbf{n}_s+\alpha_f\partial_t\boldsymbol{\eta}^k\right\|_\Gamma^2\,ds\,,
\end{aligned}$$

where $\frac{\alpha_s-\alpha_f}{2}\ge0$ with the assumption $\alpha_s\ge\alpha_f$. Adding (3.3.13) to (3.3.17) yields

$$E^k(t)+B^k(t)\le B^{k-1}(t)+C\int_0^t\|\mathbf{u}^k(s)\|_{\Omega_f}^2\,ds\,,$$

and summing over the iterates for any given $K>0$, we obtain

$$\sum_{k=1}^K E^k(t)\le B^0(t)+C\sum_{k=1}^K\int_0^t\|\mathbf{u}^k(s)\|_{\Omega_f}^2\,ds. \qquad (3.3.18)$$

In (3.3.18)

$$B^0(t)=\frac{1}{2(\alpha_f+\alpha_s)}\int_0^t g_0\,ds,$$

where $g_0 = \left\|\boldsymbol{\sigma}_f^0\mathbf{n}_f - \alpha_s\mathbf{u}^0\right\|_\Gamma^2 + \left\|-\boldsymbol{\sigma}_s^0\mathbf{n}_s + \alpha_f\partial_t\boldsymbol{\eta}^0\right\|_\Gamma^2$ is obtained by the initial guess. Now, the definition of $E^k(t)$ and (3.3.18) yield

$$\frac{\rho_f}{2}\sum_{k=1}^{K}\|\mathbf{u}^k(t)\|_{\Omega_f}^2 \le B^0(t) + C\sum_{k=1}^{K}\int_0^t \|\mathbf{u}^k(s)\|_{\Omega_f}^2\, ds,$$

and applying Gronwall's lemma, we obtain

$$\sum_{k=1}^{K}\|\mathbf{u}^k(t)\|_{\Omega_f}^2 \le \frac{2B^0(T)}{\rho_f}e^{\frac{2CT}{\rho_f}} \tag{3.3.19}$$

for any $K > 0$ and a.e. $t \in (0,T)$. The inequality (3.3.19) implies that $\mathbf{u}^k$ converges to 0 in $L^\infty(0,T;\mathbf{L^2}(\Omega_f))$ as $k \to \infty$. Also, the inequalities (3.3.18) and (3.3.19) yield

$$\begin{aligned}\sum_{k=1}^{K}\Bigg(\nu_f\int_0^t\left\|D(\mathbf{u}^k)\right\|_{\Omega_f}^2 ds + \frac{\rho_s}{2}\left\|\partial_t\boldsymbol{\eta}^k\right\|_{\Omega_s}^2 + \nu_s\left\|D(\boldsymbol{\eta}^k)\right\|_{\Omega_s}^2 + \frac{\lambda}{2}\left\|\nabla\cdot\boldsymbol{\eta}^k\right\|_{\Omega_s}^2 \\ + \frac{\alpha_s-\alpha_f}{2}\int_0^t\left\|\partial_t\boldsymbol{\eta}^k\right\|_\Gamma^2 ds\Bigg) \le \left(1 + \frac{2CT}{\rho_f}e^{\frac{2CT}{\rho_f}}\right)B^0(T),\end{aligned} \tag{3.3.20}$$

which implies that $D(\mathbf{u}^k)$, $\partial_t\boldsymbol{\eta}^k$, $D(\boldsymbol{\eta}^k)$, $\nabla\cdot\boldsymbol{\eta}^k$ converge to 0 in $L^2(0,T;\mathbf{L}^2(\Omega_f))$, $L^\infty(0,T;\mathbf{L}^2(\Omega_s))$, $L^\infty(0,T;\mathbf{L}^2(\Omega_s))$, $L^\infty(0,T;L^2(\Omega_s))$, respectively, as $k \to \infty$. In addition, $\boldsymbol{\sigma}_s^k\mathbf{n}_s$ converges to 0 in $L^\infty(0,T;\mathbf{L}^2(\Omega_s))$ by its definition, and using Poincaré-Friedrichs inequality, the convergence of $\boldsymbol{\eta}^k$ to 0 in $L^\infty(0,T;\mathbf{L}^2(\Omega_s))$ is obtained.

By the Robin condition (3.2.2) with $\mathbf{g}_s \in \mathbf{L}^2(\Gamma)$, the trace $\boldsymbol{\sigma}_s\mathbf{n}_s$ on Γ is in $\mathbf{L}^2(\Gamma)$ for a.e. $t \in (0,T)$. We prove the convergence of p^k with additional regularity assumption that $\boldsymbol{\sigma}_s\mathbf{n}_s$ is $\mathbf{H}^1(\Omega_s)$ for a.e. $t \in (0,T)$. First, we estimate a bound for the time derivative term in (3.3.6). For $\mathbf{v} \in \mathbf{V}$ the equation (3.3.6) is written as

$$\rho_f(\partial_t\mathbf{u}^k, \mathbf{v}) = -2\nu_f(D(\mathbf{u}^k), D(\mathbf{v})) - \alpha_f(\mathbf{u}^k, \mathbf{v})_\Gamma + (\alpha_f\partial_t\boldsymbol{\eta}^{k-1} - \boldsymbol{\sigma}_s^{k-1}\mathbf{n}_s, \mathbf{v})_\Gamma\,, \tag{3.3.21}$$

and the right-hand side terms in (3.3.21) are bounded using Cauchy-Schwarz inequality, the trace theorem, Korn's inequality, Poincaré-Friedrichs inequality. Then, dividing both sides by $\|\nabla\mathbf{v}\|_{\Omega_f}$ and taking supremum over $\mathbf{v} \in \mathbf{V}$, we have, for some constant $\widehat{C} > 0$,

$$\rho_f\|\partial_t\mathbf{u}^k\|_{\mathbf{V}^*} \le \widehat{C}(\,\|D(\mathbf{u}^k)\|_{\Omega_f} + \|\partial_t\boldsymbol{\eta}^{k-1}\|_\Gamma + \|\boldsymbol{\sigma}_s^{k-1}\mathbf{n}_s\|_\Gamma\,).$$

The norm equivalence of $\|\cdot\|_{\mathbf{X}^*}$ and $\|\cdot\|_{\mathbf{V}^*}$ (see Lemma 1 in [53]) then implies, for some constant $C_* > 0$,

$$\rho_f \|\partial_t \mathbf{u}^k\|_{\mathbf{X}^*} \leq C_* (\|D(\mathbf{u}^k)\|_{\Omega_f} + \|\partial_t \boldsymbol{\eta}^{k-1}\|_\Gamma + \|\boldsymbol{\sigma}_s^{k-1}\mathbf{n}_s\|_\Gamma) . \tag{3.3.22}$$

To estimate a bound for p^k, consider (3.3.6) with $\mathbf{v} \in \mathbf{X}$. We isolate the pressure term, divide by $\|\nabla \mathbf{v}\|_{\Omega_f}$, take supremum over $\mathbf{v} \in \mathbf{X}$. Then the inf-sup condition (2.1.1) and the estimate (3.3.22) yield

$$\beta \|p^k\|_{\Omega_f} \leq (1 + C_*)(\|D(\mathbf{u}^k)\|_{\Omega_f} + \|\partial_t \boldsymbol{\eta}^{k-1}\|_\Gamma + \|\boldsymbol{\sigma}_s^{k-1}\mathbf{n}_s\|_\Gamma) .$$

for some $\beta > 0$. If we square both sides, integrate over the interval $(0, t)$ for a.e. $t \in (0, T)$, then using the trace theorem,

$$\begin{aligned} \frac{\beta^2}{3(1+C_*)^2} \int_0^t \|p^k\|_{\Omega_f}^2 \, ds \quad \leq \quad & \int_0^t (\|D(\mathbf{u}^k)\|_{\Omega_f}^2 + \|\partial_t \boldsymbol{\eta}^{k-1}\|_{1,\Omega_s} \|\partial_t \boldsymbol{\eta}^{k-1}\|_{\Omega_s} \\ & + \|\boldsymbol{\sigma}_s^{k-1}\mathbf{n}_s\|_{1,\Omega_s} \|\boldsymbol{\sigma}_s^{k-1}\mathbf{n}_s\|_{\Omega_s}) \, ds . \end{aligned} \tag{3.3.23}$$

Now, $\|\partial_t \boldsymbol{\eta}^{k-1}\|_{1,\Omega_s}, \|\boldsymbol{\sigma}_s^{k-1}\mathbf{n}_s\|_{1,\Omega_s} < \infty$ as $\partial_t \boldsymbol{\eta}^{k-1}, \boldsymbol{\sigma}_s^{k-1}\mathbf{n}_s \in \mathbf{H}^1(\Omega_s)$ for a.e. $t \in (0, T)$. Hence the convergence of $D(\mathbf{u}^k)$, $\partial_t \boldsymbol{\eta}^k$, $\boldsymbol{\sigma}_s^k \mathbf{n}_s$ implies that $\displaystyle\int_0^t \|p^k\|_{\Omega_f}^2 ds$ converges to 0 as $k \to \infty$, i.e., p^k converges to 0 in $L^2(0, T; L^2(\Omega_f))$. □

Chapter 4

Nonconforming time discretization

The global-in-time DD approach allows the use of separate time discretizations in each subdomain because the local problems are still time-dependent. On the space-time interface, the transfer of information between different time grids is achieved through a suitable projection technique.

4.1 Notation

Consider τ_f be a partition of time interval $(0,T)$ into subintervals for the Stokes domain. Let $J_f^m := (t_f^{m-1}, t_f^m]$ and step size $\Delta t_f^m := t_f^m - t_f^{m-1}$ for $m = 1, ..., M_f$. The space of piecewise constant functions in time on grid τ_f, with values in $W = L^2(\Gamma)$, is denoted by $P_0(\tau_f, W)$:

$$P_0(\tau_f, W) = \{\phi : (0,T) \to W, \phi \text{ is constant on } J_f^m \quad \forall m = 1, ..., M_f\}.$$

Similarly, we define τ_s, M_s, J_s^n and Δt_s^n for the structure domain. To exchange data on the space-time interface between different time grids, we introduce the L^2 projection $\Pi_{s,f}$ from $P_0(\tau_f, W)$ onto $P_0(\tau_s, W)$ [66]:

$$\Pi_{s,f}(\phi)|_{J_s^n} = \frac{1}{|J_s^n|} \sum_{l=1}^{M_f} \int_{J_s^n \cap J_f^l} \phi.$$

The projection $\Pi_{f,s}$ from $P_0(\tau_s, W)$ onto $P_0(\tau_f, W)$ is also defined similarly.

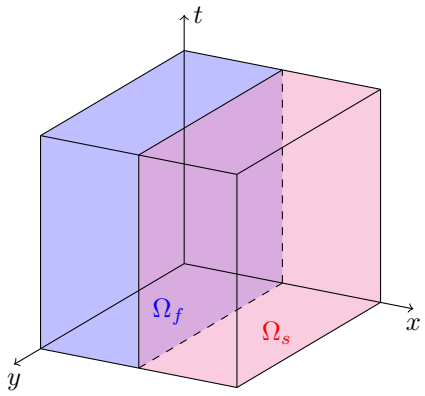

Figure 4.1: The fluid and structure domains

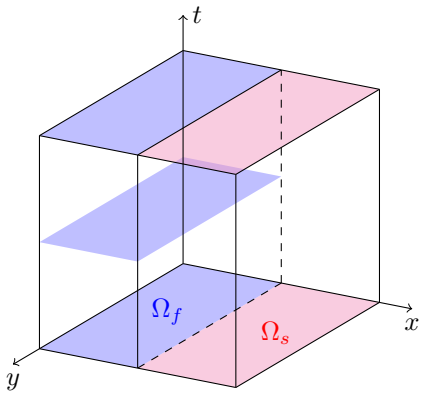

Figure 4.2: Nonconforming time grids

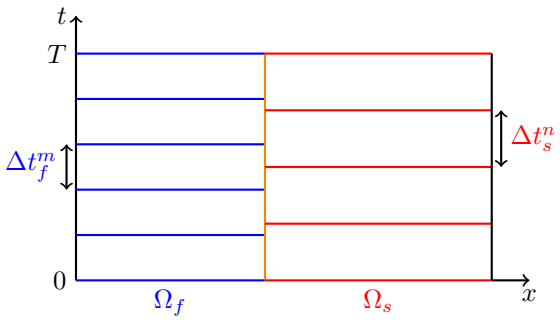

Figure 4.3: Projection of nonconforming time grids in two dimensions

4.2 Semi-discrete FSI system and discrete convergence analysis

We discretize the FSI system in time as a parabolic problem using an additional variable $\dot{\boldsymbol{\eta}} \in \boldsymbol{\Sigma}$, representing $\partial_t \boldsymbol{\eta}$. Using the backward Euler method, the semi-discrete FSI system with Robin transmission conditions (3.2.1) and (3.2.2) is given by: for $m = 1, ..., M_f$

$$\rho_f(\mathbf{u}^m - \mathbf{u}^{m-1}) + \Delta t_f^m(-2\nu_f \nabla \cdot D(\mathbf{u}^m) + \nabla p^m I) = \mathbf{f}_f^m \quad \text{in } \Omega_f\,, \tag{4.2.1}$$

$$\nabla \cdot \mathbf{u}^m = 0 \quad \text{in } \Omega_f\,, \tag{4.2.2}$$

$$\Delta t_f^m \left(\alpha_f \mathbf{u}^m + \boldsymbol{\sigma}_f^m \mathbf{n}_f\right) = \int_{J_f^m} \Pi_{f,s} \left(\alpha_f \dot{\boldsymbol{\eta}} - \boldsymbol{\sigma}_s \mathbf{n}_s\right) dt \text{ on } \Gamma, \tag{4.2.3}$$

and for $n = 1, ..., M_s$

$$\rho_s(\dot{\boldsymbol{\eta}}^n - \dot{\boldsymbol{\eta}}^{n-1}) - 2\nu_s\Delta t_s^n \nabla \cdot D(\boldsymbol{\eta}^n) - \lambda\Delta t_s^n \nabla(\nabla \cdot \boldsymbol{\eta}^n) = \mathbf{f}_s^n \quad \text{in } \Omega_s\,, \tag{4.2.4}$$

$$(\boldsymbol{\eta}^n - \boldsymbol{\eta}^{n-1}) - \Delta t_s^n \dot{\boldsymbol{\eta}}^n = \mathbf{0} \quad \text{in } \Omega_s \tag{4.2.5}$$

$$\Delta t_s^n \left(-\alpha_s \dot{\boldsymbol{\eta}}^n - \boldsymbol{\sigma}_s^n \mathbf{n}_s\right) = \int_{J_s^n} \Pi_{s,f} \left(-\alpha_s \mathbf{u} + \boldsymbol{\sigma}_f \mathbf{n}_f\right) dt \quad \text{on } \Gamma, \tag{4.2.6}$$

where $(\mathbf{u}, p) = (\mathbf{u}^m, p^m)_{m=1}^{M_f}$ satisfies the boundary condition (2.0.3) and the initial condition (2.0.4), and $(\boldsymbol{\eta}, \dot{\boldsymbol{\eta}}) = (\boldsymbol{\eta}^n, \dot{\boldsymbol{\eta}}^n)_{n=1}^{M_s}$ satisfies the boundary condition (2.0.6) and the initial conditions (2.0.7), (2.0.8).

Next, we present the semi-discrete SWR algorithm and prove the convergence of the iterations. Consider the following algorithm. In the kth iteration step, solve

$$\rho_f(\mathbf{u}^{k,m} - \mathbf{u}^{k,m-1}) + \Delta t_f^m(-2\nu_f \nabla \cdot D(\mathbf{u}^{k,m}) + \nabla p^{k,m} I) = \mathbf{f}_f^m \quad \text{in } \Omega_f\,, \tag{4.2.7}$$

$$\nabla \cdot \mathbf{u}^{k,m} = 0 \quad \text{in } \Omega_f\,, \tag{4.2.8}$$

$$\Delta t_f^m \left(\alpha_f \mathbf{u}^{k,m} + \boldsymbol{\sigma}_f^{k,m} \mathbf{n}_f\right) = \int_{J_f^m} \Pi_{f,s} \left(\alpha_f \dot{\boldsymbol{\eta}}^{k-1} - \boldsymbol{\sigma}_s^{k-1} \mathbf{n}_s\right) dt \text{ on } \Gamma, \tag{4.2.9}$$

for $(\mathbf{u}^{k,m}, p^{k,m})$ satisfying (2.0.3) and (2.0.4), where $\mathbf{u}^{k,0} = \mathbf{u}^0$, $\mathbf{u}^{k,m} := \mathbf{u}^k|_{J_f^m}, p^{k,m} := p^k|_{J_f^m}$ for $m = 1, ..., M_f$, and

$$\rho_s(\dot{\boldsymbol{\eta}}^{k,n} - \dot{\boldsymbol{\eta}}^{k,n-1}) - 2\nu_s\Delta t_s^n \nabla \cdot D(\boldsymbol{\eta}^{k,n}) - \lambda\Delta t_s^n \nabla(\nabla \cdot \boldsymbol{\eta}^{k,n}) = \mathbf{f}_s^n \quad \text{in } \Omega_s\,, \tag{4.2.10}$$

$$(\boldsymbol{\eta}^{k,n} - \boldsymbol{\eta}^{k,n-1}) - \Delta t_s^n \dot{\boldsymbol{\eta}}^{k,n} = \mathbf{0} \quad \text{in } \Omega_s, \tag{4.2.11}$$

$$\Delta t_s^n \left(-\alpha_s \dot{\boldsymbol{\eta}}^{k,n} - \boldsymbol{\sigma}_s^{k,n} \mathbf{n}_s\right) = \int_{J_s^n} \Pi_{s,f} \left(-\alpha_s \mathbf{u}^{k-1} + \boldsymbol{\sigma}_f^{k-1} \mathbf{n}_f\right) dt \quad \text{on } \Gamma \tag{4.2.12}$$

for $(\boldsymbol{\eta}^{k,n}, \dot{\boldsymbol{\eta}}^{k,n})$ satisfying (2.0.6)-(2.0.8), where $\boldsymbol{\eta}^{k,0} = \boldsymbol{\eta}^0$, $\boldsymbol{\eta}^{k,n} := \boldsymbol{\eta}^k|_{J_s^n}$ $\dot{\boldsymbol{\eta}}^{k,0} = \bar{\boldsymbol{\eta}}^0$, $\dot{\boldsymbol{\eta}}^{k,n} := \dot{\boldsymbol{\eta}}^k|_{J_s^n}$ for $n = 1, ..., M_s$. In the next theorem we show that the weak solution to (4.2.7)-(4.2.12) converges to the weak solution of (4.2.1)-(4.2.5) as $k \to \infty$.

Theorem 4.2.1. *Suppose the initial guess $(\mathbf{u}^0, p^0, \boldsymbol{\eta}^0, \dot{\boldsymbol{\eta}}^0)$ is chosen such that the Robin-Robin conditions* (4.2.9) *and* (4.2.12) *are well-defined in $\boldsymbol{L}^2(\Gamma)$. With an additional regularity assumption for $\boldsymbol{\sigma}_s \mathbf{n}_s$ and the condition that $\alpha_f = \alpha_s$, the weak formulation* (4.2.7)-(4.2.12) *defines a unique*

sequence of iterates

$$(\mathbf{u}^k, p^k, \boldsymbol{\eta}^k, \dot{\boldsymbol{\eta}}^k) \in P_0(\tau_f, \boldsymbol{X}) \times P_0(\tau_f, Q) \times P_0(\tau_s, \boldsymbol{\Sigma}) \times P_0(\tau_s, \boldsymbol{\Sigma})$$

that converges to the weak solution of (4.2.1)-(4.2.6).

Proof. Since the equations are linear, we can set $\mathbf{f}_f = \mathbf{f}_s = \mathbf{u}^0 = \boldsymbol{\eta}^0 = \dot{\boldsymbol{\eta}}^0 = \mathbf{0}$, and proceed to derive energy estimates following the proof of Theorem 3.3.1. We multiply the equations (4.2.7) and (4.2.8) by $\mathbf{u}^{k,m}$ and $p^{k,m}$, respectively, use (3.3.10), and add the resulting equations together to obtain

$$\begin{aligned}
&\rho_f(\mathbf{u}^{k,m}, \mathbf{u}^{k,m})_{\Omega_f} - \rho_f(\mathbf{u}^{k,m-1}, \mathbf{u}^{k,m})_{\Omega_f} + 2\nu_f \Delta t_f^m \left\| D(\mathbf{u}^{k,m}) \right\|_{\Omega_f}^2 \\
&\quad + \frac{\Delta t_f^m}{2(\alpha_f + \alpha_s)} \left\| \boldsymbol{\sigma}_f^{k,m} \mathbf{n}_f - \alpha_s \mathbf{u}^{k,m} \right\|_{\Gamma}^2 \\
&\quad \leq \frac{\Delta t_f^m}{2(\alpha_f + \alpha_s)} \left\| \boldsymbol{\sigma}_f^{k,m} \mathbf{n}_f + \alpha_f \mathbf{u}^{k,m} \right\|_{\Gamma}^2 + \frac{\Delta t_f^m}{2} (\alpha_s - \alpha_f) \left\| \mathbf{u}^{k,m} \right\|_{\Gamma}^2 . \qquad (4.2.13)
\end{aligned}$$

By using Cauchy-Schwarz inequality and $\frac{1}{2}(a^2 - b^2) \leq a^2 - ab$, we can obtain

$$\begin{aligned}
&\frac{\rho_f}{2} \left(\|\mathbf{u}^{k,m}\|_{\Omega_f}^2 - \|\mathbf{u}^{k,m-1}\|_{\Omega_f}^2 \right) + 2\nu_f \int_{J_f^m} \left\| D(\mathbf{u}^k) \right\|_{\Omega_f}^2 dt \\
&\quad + \frac{1}{2(\alpha_f + \alpha_s)} \int_{J_f^m} \left\| \boldsymbol{\sigma}_f^k \mathbf{n}_f - \alpha_s \mathbf{u}^k \right\|_{\Gamma}^2 dt \\
&\quad \leq \frac{1}{2(\alpha_f + \alpha_s)} \int_{J_f^m} \left\| \boldsymbol{\sigma}_f^k \mathbf{n}_f + \alpha_f \mathbf{u}^k \right\|_{\Gamma}^2 dt + \frac{(\alpha_s - \alpha_f)}{2} \int_{J_f^m} \left\| \mathbf{u}^k \right\|_{\Gamma}^2 dt. \qquad (4.2.14)
\end{aligned}$$

Next, multiply (4.2.10) by $\dot{\boldsymbol{\eta}}^{k,n}$, integrate over Ω_s and use (4.2.11) and (3.3.15) to have

$$\begin{aligned}
&\frac{\rho_s}{2} \left(\|\dot{\boldsymbol{\eta}}^{k,n}\|_{\Omega_s}^2 - \|\dot{\boldsymbol{\eta}}^{k,n-1}\|_{\Omega_s}^2 \right) + \nu_s \left(\left\| D(\boldsymbol{\eta}^{k,n}) \right\|_{\Omega_s}^2 - \left\| D(\boldsymbol{\eta}^{k,n-1}) \right\|_{\Omega_s}^2 \right) \\
&\quad + \frac{\lambda}{2} \left(\left\| \nabla \cdot \boldsymbol{\eta}^{k,n} \right\|_{\Omega_s}^2 - \left\| \nabla \cdot \boldsymbol{\eta}^{k,n-1} \right\|_{\Omega_s}^2 \right) + \frac{1}{2(\alpha_f + \alpha_s)} \int_{J_s^n} \left\| -\boldsymbol{\sigma}_s^k \mathbf{n}_s + \alpha_f \dot{\boldsymbol{\eta}}^k \right\|_{\Gamma}^2 dt \\
&\quad \leq \frac{1}{2(\alpha_f + \alpha_s)} \int_{J_s^n} \left\| -\boldsymbol{\sigma}_s^k \mathbf{n}_s - \alpha_s \dot{\boldsymbol{\eta}}^k \right\|_{\Gamma}^2 dt - \frac{(\alpha_s - \alpha_f)}{2} \int_{J_s^n} \left\| \dot{\boldsymbol{\eta}}^k \right\|_{\Gamma}^2 dt. \qquad (4.2.15)
\end{aligned}$$

To eliminate the last terms of equations (4.2.14) and (4.2.15), we assume that $\alpha_f = \alpha_s$, since we cannot use Gronwall's lemma as for the continuous case. By summing these equations over the

subintervals in $(0, t_f^m]$ and $(0, t_s^n]$, respectively, we obtain

$$\frac{\rho_f}{2}\|\mathbf{u}^{k,m}\|^2_{\Omega_f} + 2\nu_f \int_0^{t_f^m} \left\|D(\mathbf{u}^k)\right\|^2_{\Omega_f} dt + \frac{1}{2(\alpha_f+\alpha_s)} \int_0^{t_f^m} \left\|\boldsymbol{\sigma}_f^k \mathbf{n}_f - \alpha_s \mathbf{u}^k\right\|^2_{\Gamma} dt$$
$$\leq \frac{1}{2(\alpha_f+\alpha_s)} \int_0^{t_f^m} \left\|\boldsymbol{\sigma}_f^k \mathbf{n}_f + \alpha_f \mathbf{u}^k\right\|^2_{\Gamma} dt, \tag{4.2.16}$$

and

$$\frac{\rho_s}{2}\|\dot{\boldsymbol{\eta}}^{k,n}\|^2_{\Omega_s} + \nu_s\left\|D(\boldsymbol{\eta}^{k,n})\right\|^2_{\Omega_s} + \frac{\lambda}{2}\left\|\nabla\cdot\boldsymbol{\eta}^{k,n}\right\|^2_{\Omega_s}$$
$$+\frac{1}{2(\alpha_f+\alpha_s)} \int_0^{t_s^n} \left\|-\boldsymbol{\sigma}_s^k \mathbf{n}_s + \alpha_f \dot{\boldsymbol{\eta}}^k\right\|^2_{\Gamma} dt$$
$$\leq \frac{1}{2(\alpha_f+\alpha_s)} \int_0^{t_s^n} \left\|-\boldsymbol{\sigma}_s^k \mathbf{n}_s - \alpha_s \dot{\boldsymbol{\eta}}^k\right\|^2_{\Gamma} dt. \tag{4.2.17}$$

We add (4.2.16) and (4.2.17), apply the Robin conditions (4.2.9) and (4.2.12) and set $t_f^m = t_s^n = T$ to obtain the following.

$$\begin{aligned}
&\frac{\rho_f}{2}\|\mathbf{u}^{k,M_f}\|^2_{\Omega_f} + 2\nu_f \int_0^T \left\|D(\mathbf{u}^k)\right\|^2_{\Omega_f} dt \\
&\quad \frac{\rho_s}{2}\|\dot{\boldsymbol{\eta}}^{k,M_s}\|^2_{\Omega_s} + \nu_s\left\|D(\boldsymbol{\eta}^{k,M_s})\right\|^2_{\Omega_s} + \frac{\lambda}{2}\left\|\nabla\cdot\boldsymbol{\eta}^{k,M_s}\right\|^2_{\Omega_s} \\
&\quad + \frac{1}{2(\alpha_f+\alpha_s)} \int_0^T \left\|\boldsymbol{\sigma}_f^k \mathbf{n}_f - \alpha_s \mathbf{u}^k\right\|^2_{\Gamma} dt + \frac{1}{2(\alpha_f+\alpha_s)} \int_0^T \left\|-\boldsymbol{\sigma}_s^k \mathbf{n}_s + \alpha_f \dot{\boldsymbol{\eta}}^k\right\|^2_{\Gamma} dt \\
&\quad \leq \frac{1}{2(\alpha_f+\alpha_s)} \int_0^T \left\|\boldsymbol{\sigma}_f^k \mathbf{n}_f + \alpha_f \mathbf{u}^k\right\|^2_{\Gamma} dt + \frac{1}{2(\alpha_f+\alpha_s)} \int_0^T \left\|-\boldsymbol{\sigma}_s^k \mathbf{n}_s - \alpha_s \dot{\boldsymbol{\eta}}^k\right\|^2_{\Gamma} dt \\
&\quad \leq \frac{1}{2(\alpha_f+\alpha_s)} \int_0^T \left\|\Pi_{s,f}(\boldsymbol{\sigma}_f^{k-1} \mathbf{n}_f - \alpha_s \mathbf{u}^{k-1})\right\|^2_{\Gamma} dt \\
&\quad + \frac{1}{2(\alpha_f+\alpha_s)} \int_0^T \left\|\Pi_{f,s}(-\boldsymbol{\sigma}_s^{k-1} \mathbf{n}_s + \alpha_f \dot{\boldsymbol{\eta}}^{k-1})\right\|^2_{\Gamma} dt \\
&\quad \leq \frac{1}{2(\alpha_f+\alpha_s)} \int_0^T \left\|\boldsymbol{\sigma}_f^{k-1} \mathbf{n}_f - \alpha_s \mathbf{u}^{k-1}\right\|^2_{\Gamma} dt \\
&\quad + \frac{1}{2(\alpha_f+\alpha_s)} \int_0^T \left\|-\boldsymbol{\sigma}_s^{k-1} \mathbf{n}_s + \alpha_f \dot{\boldsymbol{\eta}}^{k-1}\right\|^2_{\Gamma} dt\,.
\end{aligned} \tag{4.2.18}$$

Then, for all $k > 0$

$$\frac{\rho_f}{2}\|\mathbf{u}^{k,M_f}\|^2_{\Omega_f} + 2\nu_f \int_0^T \left\|D(\mathbf{u}^k)\right\|^2_{\Omega_f} dt + \frac{\rho_s}{2}\|\dot{\boldsymbol{\eta}}^{k,M_s}\|^2_{\Omega_s} + \nu_s\left\|D(\boldsymbol{\eta}^{k,M_s})\right\|^2_{\Omega_s}$$
$$+\frac{\lambda}{2}\left\|\nabla\cdot\boldsymbol{\eta}^{k,M_s}\right\|^2_{\Omega_s} + B^k \leq B^{k-1}, \tag{4.2.19}$$

where

$$B^k = \frac{1}{2(\alpha_f+\alpha_s)}\int_0^T \left\|\boldsymbol{\sigma}_f^k\mathbf{n}_f - \alpha_s\mathbf{u}^k\right\|_\Gamma^2 dt + \frac{1}{2(\alpha_f+\alpha_s)}\int_0^T \left\|-\boldsymbol{\sigma}_s^k\mathbf{n}_s + \alpha_f\dot{\boldsymbol{\eta}}^k\right\|_\Gamma^2 dt\,.$$

By summing over the iterates k, we conclude that $\|\mathbf{u}^{k,M_f}\|_{\Omega_f}$, $\int_0^T \|D(\mathbf{u}^k)\|_{\Omega_f}^2 dt$, $\|D(\boldsymbol{\eta}^{k,M_s})\|_{\Omega_s}$, $\left\|\nabla\cdot\boldsymbol{\eta}^{k,M_s}\right\|_{\Omega_s}$ and $\|\dot{\boldsymbol{\eta}}^{k,M_s}\|_{\Omega_s}$ converge to 0 as $k\to\infty$. This implies $\int_0^{t_f^m}\|D(\mathbf{u}^k)\|_{\Omega_f}^2 dt$ converges to 0 as $k\to\infty$ for all $m=1,2,\cdots,M_f$, and also $\|D(\mathbf{u}^{k,m})\|_{\Omega_f}$ converges 0 for all $m=1,2,\cdots,M_f$, as $\mathbf{u}^k\in P_0(\tau_f,\mathbf{X})$. Now using Poincaré-Friedrichs inequality, $\|\mathbf{u}^{k,m}\|_{\Omega_f}\le C_{PF1}\|D(\mathbf{u}^{k,m})\|_{\Omega_f}$ and $\|\boldsymbol{\eta}^{k,M_s}\|_{\Omega_s}\le C_{PF2}\|D(\boldsymbol{\eta}^{k,M_s})\|_{\Omega_s}$ for some constants $C_{PF1},C_{PF2}>0$, which implies $\|\mathbf{u}^{k,m}\|_{\Omega_f}$ converges to 0 for all $m=1,2,\cdots,M_f$, and $\|\boldsymbol{\eta}^{k,M_s}\|_{\Omega_s}$ also converges to 0 as $k\to\infty$.

Next, we show the convergence of $\boldsymbol{\eta}^{k,n}$ $\dot{\boldsymbol{\eta}}^{k,n}$ and $D(\boldsymbol{\eta}^{k,n})$ in the L^2 norm for all $n=1,2,\cdots,M_s$. We multiply (4.2.10) by $\dot{\boldsymbol{\eta}}^{k,n-1}$, integrate over Ω_s, and use Cauchy-Schwarz inequality and the Trace theorem to obtain

$$\begin{aligned}\|\dot{\boldsymbol{\eta}}^{k,n-1}\|_{\Omega_s}^2 \;\le\; & C_{s1}\Big(\|\dot{\boldsymbol{\eta}}^{k,n}\|_{\Omega_s}\|\dot{\boldsymbol{\eta}}^{k,n-1}\|_{\Omega_s} + \|D(\boldsymbol{\eta}^{k,n})\|_{\Omega_s}\|D(\dot{\boldsymbol{\eta}}^{k,n-1}\|_{\Omega_s}\\ &+\|\boldsymbol{\sigma}_s^{k,n}\mathbf{n}_s\|_{1,\Omega_s}^{1/2}\|\boldsymbol{\sigma}_s^{k,n}\mathbf{n}_s\|_{\Omega_s}^{1/2}\|\dot{\boldsymbol{\eta}}^{k,n-1}\|_{1,\Omega_s}^{1/2}\|\dot{\boldsymbol{\eta}}^{k,n-1}\|_{\Omega_s}^{1/2}\Big)\,,\end{aligned} \tag{4.2.20}$$

for some constant $C_{s1}>0$. Similarly, from (4.2.11), for some constant $C_{s2}>0$,

$$\|\boldsymbol{\eta}^{k,n-1}\|_{\Omega_s}\le C_{s2}(\|\boldsymbol{\eta}^{k,n}\|_{\Omega_s}+\|\dot{\boldsymbol{\eta}}^{k,n}\|_{\Omega_s})\,. \tag{4.2.21}$$

For $n=M_s$, $\|\boldsymbol{\sigma}_s^{k,n}\mathbf{n}_s\|_{\Omega_s}$ in (4.2.20) converges to 0 as $k\to\infty$ by its definition and the convergence of $\|D(\boldsymbol{\eta}^{k,M_s})\|_{\Omega_s}$, hence the last term in (4.2.20) converges to 0 if $\boldsymbol{\sigma}_s^{k,n}\mathbf{n}_s$ has H^1 regularity. Then, (4.2.20) and (4.2.21), together with the fact that $\|\dot{\boldsymbol{\eta}}^{k,M_s}\|_{\Omega_s}$ and $\|\boldsymbol{\eta}^{k,M_s}\|_{\Omega_s}$ converge to 0, imply $\|\dot{\boldsymbol{\eta}}^{k,M_s-1}\|_{\Omega_s}$ and $\|\boldsymbol{\eta}^{k,M_s-1}\|_{\Omega_s}$ converge to 0 as $k\to\infty$. Now, multiplying (4.2.10) by $\boldsymbol{\eta}^{k,n}$, integrating over Ω_s and using Cauchy-Schwarz inequality, (4.2.12) and the Trace theorem,

$$\begin{aligned}\|D(\boldsymbol{\eta}^{k,n})\|_{\Omega_s}^2+\|\nabla\cdot\boldsymbol{\eta}^{k,n}\|_{\Omega_s}^2 \le\; & C_{s3}\Big(\|\dot{\boldsymbol{\eta}}^{k,n}\|_{\Omega_s}\|\boldsymbol{\eta}^{k,n}\|_{\Omega_s}+\|\dot{\boldsymbol{\eta}}^{k,n-1}\|_{\Omega_s}\|\boldsymbol{\eta}^{k,n}\|_{\Omega_s}\\ &+\|\Pi_{s,f}|_{J_s^n}(\mathbf{u}^{k-1}+\boldsymbol{\sigma}_f^{k-1}\mathbf{n}_f)\|_\Gamma\|\boldsymbol{\eta}^{k,n}\|_{1,\Omega_s}^{1/2}\|\boldsymbol{\eta}^{k,n}\|_{\Omega_s}^{1/2}\Big)\end{aligned} \tag{4.2.22}$$

for some $C_{s3}>0$. Since $\mathbf{g}_f\in\mathbf{L}^2(\Gamma)$, the convergence of $\|\boldsymbol{\eta}^{k,M_s-1}\|_{\Omega_s}$ to 0 implies that $\|D(\boldsymbol{\eta}^{k,M_s-1})\|_{\Omega_s}$ converges to 0. Therefore, in this way, we can show that $\|\boldsymbol{\eta}^{k,n}\|_{\Omega_s}$, $\|\dot{\boldsymbol{\eta}}^{k,n}\|_{\Omega_s}$ and $\|D(\boldsymbol{\eta}^{k,n})\|_{\Omega_s}$ con-

verge to 0 as $k \to \infty$ for all $n = 1, 2, \ldots, M_s$.

To establish the convergence of $p^{k,m}$, we follow a similar approach to the continuous case, and obtain the following result for some $\beta > 0$:

$$\beta \|p^{k,m}\|_{\Omega_f} \leq (1 + C_*)(\|D(\mathbf{u}^{k,m})\|_{\Omega_f} + \|\Pi_{f,s}\dot{\boldsymbol{\eta}}^{k-1,m}\|_{\Gamma} + \|\Pi_{f,s}\boldsymbol{\sigma}_s^{k-1,m}\mathbf{n}_s\|_{\Gamma}) .$$

Squaring both sides and integrating over the interval $(0, t_f^m]$, we get, for all m

$$\begin{aligned} \frac{\beta^2}{3(1+C_*)} \int_0^{t_f^m} \|p^k\|_{\Omega_f}^2 \, dt \quad &\leq \int_0^{t_f^m} \|D(\mathbf{u}^k)\|_{\Omega_f}^2 ds + \int_0^T \|\dot{\boldsymbol{\eta}}^{k-1}\|_{1,\Omega_s} \|\dot{\boldsymbol{\eta}}^{k-1}\|_{\Omega_s} ds \\ &+ \int_0^T \|\boldsymbol{\sigma}_s^{k-1}\mathbf{n}_s\|_{1,\Omega_s} \|\boldsymbol{\sigma}_s^{k-1}\mathbf{n}_s\|_{\Omega_s} \, ds . \end{aligned} \tag{4.2.23}$$

The last term in (4.2.23) converges to 0 by the regularity assumption for $\boldsymbol{\sigma}_s\mathbf{n}_s$ and the convergence of $\|D(\boldsymbol{\eta}^{k,n})\|_{\Omega_s}$ for all $n = 1, 2, \ldots, M_s$. Then, the convergence of $\int_0^{t_f^m} \|p^k\|_{\Omega_f}^2 dt$ to 0 as $k \to \infty$ follows from the convergence of $\|D(\mathbf{u}^{k,m})\|_{\Omega_f}^2$ and $\|\dot{\boldsymbol{\eta}}^{k,n}\|_{\Omega_s}$ for all m and n. Finally, we have that $\|p^{k,m}\|_{\Omega_f}$ converges to 0 for all $m = 1, 2, \ldots, M_f$, as $p^k \in P^0(\tau_f, Q)$. □

4.3 Numerical results

We provide two numerical examples to demonstrate the effectiveness of our proposed methods. The first example is a manufactured problem with a known solution, which we use to assess the accuracy and efficiency of the methods. The second example is a benchmark problem from the field of hemodynamics that has been previously considered in [73, 88]. For both examples, we use GMRES to achieve fast convergence when solving the interface problem (3.1.5) or (3.2.8). The SWR algorithm analyzed in Section 4 is a Jacobi-type iterative method, thus we expect fast convergence to be achieved by GMRES.

4.3.1 Test 1 : With a Known Analytical Solution

Consider an example with a known exact solution, where the fluid subdomain is $\Omega_f = (0, 1) \times (0, 1)$ and the structure subdomain is $\Omega_s = (0, 1) \times (1, 2)$. The interface between the two

subdomains is given by $\Gamma = \{(x, y) : 0 < x < 1, y = 1\}$. The chosen exact solution is

$$\mathbf{u} = \begin{pmatrix} \cos(x+t)\sin(y+t) + \sin(x+t)\cos(y+t) \\ -\sin(x+t)\cos(y+t) - \cos(x+t)\sin(y+t) \end{pmatrix}$$
$$p = 2\nu_f(\sin(x+t)\sin(y+t) - \cos(x+t)\cos(y+t)) + 2\nu_s\cos(x+t)\sin(y+t)$$
$$\boldsymbol{\eta} = \begin{pmatrix} \sin(x+t)\sin(y+t) \\ \cos(x+t)\cos(y+t) \end{pmatrix}.$$

The constants, ρ_s, ρ_f, ν_s, ν_f, and λ, are set to unity. For the Robin conditions (3.2.1) and (3.2.2) we choose $\alpha_f = \alpha_p = 1$, and the tolerance for GMRES is set to $\epsilon = 10^{-7}$.

We test the convergence of both methods in space using Taylor-Hood elements for the fluid subproblem and $\mathbf{P}_2$ elements for the structure subproblem, along with nonconforming time grids. We then repeat the test using MINI elements for the fluid and $\mathbf{P}_1$ element for the structure subproblem. The errors at the final time $T = 0.00025$ are presented in Tables 4.1-4.3 for all variable, with expected convergence rates shown. To test convergence with respect to different time steps, we use Δt_{coarse} to denote the coarse time step size and set the fine time step size to be $\Delta t_{\text{fine}} = \Delta t_{\text{coarse}}/2$. Numerical tests are performed using three different types of time grids:

1. Coarse conforming time grids: $\Delta t_f = \Delta t_s = \Delta t_{\text{coarse}}$,
2. Fine conforming time grids: $\Delta t_f = \Delta t_s = \Delta t_{\text{fine}}$,
3. Nonconforming time grids: $\Delta t_f = \Delta t_{\text{coarse}}$ and $\Delta t_s = \Delta t_{\text{fine}}$.

First, the Steklov-Poincaré interface problem (3.1.5) is solved using Taylor-Hood and $\mathbf{P}2$ elements with $h = \frac{1}{32}$ and the three types of time grids given above, with $\Delta t_{\text{coarse}} \in \{0.2, 0.1, 0.05, 0.0025\}$. Then the same test is repeated using MINI and $\mathbf{P}1$ elements with $h = \frac{1}{64}$ and $\Delta t_{\text{coarse}} \in \{0.4, 0.2, 0.1, 0.05\}$. Figures 4.4 and 4.5 demonstrate the first-order convergence of solutions, showing the errors at $T = 0.2$ and $T = 0.4$, respectively. For the nonconforming time grids, $\Delta t_f = \Delta t_{\text{coarse}}$ and $\Delta t_s = \Delta t_{\text{fine}}$. Thus, as expected, the fluid velocity and pressure errors for the nonconforming time grids are close to the errors of the conforming coarse grids, while the displacement errors are between the errors of the conforming fine and coarse grids. We also solve the interface problem (3.2.8) using Taylor-Hood and $\mathbf{P}2$ elements with the same condition as (3.1.5). Figure 4.6 shows a result similar to the result obtained by the Steklov-Poincaré method in Figure 4.4.

Next, we compare the computer running times for both methods using conforming and nonconforming time grids on a fixed mesh. Computer running times for both methods are presented in Table 4.4 and Table 4.5. The tables show that the computer running times for the nonconforming cases are close to the conforming coarse cases than the conforming fine cases for both methods, demonstrating the efficiency of the proposed methods. We also examine the convergence behavior of GMRES by various Robin parameters, α_f and α_s. Table 4.6 presents the number of iterations for various α_s values when α_f is fixed to 1. The table indicates that a higher α_s value yields faster convergence of GMRES iterations. However, in an additional test, we observe that the convergence of GMRES is not much affected by α_f values.

h		1/4	1/8	1/16	1/32
$\mathbf{u}$	L^2 error	1.99e-04	1.94e-05 [3.36]	2.52e-06 [2.95]	3.32e-07 [2.93]
	H^1 error	5.91e-03	1.21e-03 [2.28]	3.03e-04 [2.00]	7.49e-05 [2.01]
p	L^2 error	5.28e-03	1.05e-03 [2.32]	2.49e-04 [2.08]	6.52e-05 [1.93]
$\boldsymbol{\eta}$	L^2 error	2.21e-04	2.31e-05 [3.26]	2.39e-06 [3.28]	3.10e-07 [2.94]
	H^1 error	6.51e-03	1.40e-03 [2.22]	3.02e-04 [2.21]	7.62e-05 [1.99]

Table 4.1: Errors by the Steklov-Poincaré method using Taylor-Hood and $\mathbf{P}2$ elements, $\Delta t_f = 0.000025$ and $\Delta t_s = 0.000050$.

h		1/4	1/8	1/16	1/32
$\mathbf{u}$	L^2 error	8.35e-03	1.98e-03 [2.08]	4.64e-04 [2.09]	1.20e-04 [1.96]
	H^1 error	2.18e-01	8.25e-02 [1.40]	3.60e-02 [1.20]	1.79e-02[1.00]
p	L^2 error	8.24e-01	1.85e-01 [2.16]	5.01e-02 [1.88]	1.08e-02 [2.22]
$\boldsymbol{\eta}$	L^2 error	6.35e-03	1.40e-03 [2.18]	3.46e-04 [2.02]	8.76e-05 [1.98]
	H^1 error	8.24e-02	3.82e-02 [1.11]	1.90e-02 [1.00]	9.43e-03 [1.01]

Table 4.2: Errors by the Steklov-Poincaré method using MINI and $\mathbf{P}1$ elements, $\Delta t_f = 0.000025$ and $\Delta t_s = 0.000050$.

h		1/4	1/8	1/16	1/32
$\mathbf{u}$	L^2 error	1.98e-04	1.92e-05 [3.36]	2.50e-06 [2.94]	3.26e-07 [2.94]
	H^1 error	5.90e-03	1.21e-03 [2.29]	3.01e-04 [2.00]	7.48e-05 [2.01]
p	L^2 error	5.52e-03	1.10e-03 [2.33]	2.56e-04 [2.10]	6.97e-05 [1.88]
$\boldsymbol{\eta}$	L^2 error	2.22e-04	2.31e-05 [3.26]	2.39e-06 [3.28]	3.10e-07 [2.94]
	H^1 error	6.51e-03	1.40e-03 [2.22]	3.02e-04 [2.21]	7.62e-05 [1.99]

Table 4.3: Errors by the Robin method ($\alpha_f = \alpha_s = 1$) using Taylor-Hood and $\mathbf{P}2$ elements, $\Delta t_f = 0.000050$, $\Delta t_s = 0.000025$.

Δt	Steklov-Poincaré Method		Robin Method ($\alpha_f = \alpha_p = 1$)	
	Conforming	Nonconforming	Conforming	Nonconforming
0.2	335		526	
		376		532
0.1	651		942	
		802		947
0.05	1324		1765	
		1537		1785
0.025	2630		3331	
		3053		3474
0.0125	5201		6937	

Table 4.4: Comparison of the computer running times (in seconds) of conforming and nonconforming time grids using Taylor-Hood and $\mathbf{P}2$ elements with $h = 1/32$.

Δt	Steklov-Poincaré Method		Δt	Robin Method ($\alpha_f = \alpha_p = 1$)	
	Conforming	Nonconforming		Conforming	Nonconforming
0.4	2224		0.8	7958	
		2784			8060
0.2	4476		0.4	14670	
		5408			15403
0.1	9468		0.2	27961	
		11137			28217
0.05	18405		0.1	51483	
		19198			53867
0.025	38525		0.05	115693	

Table 4.5: Comparison of the computer running times (in seconds) of conforming and nonconforming time grids using MINI and $\mathbf{P}1$ elements with $h = 1/64$.

α_s	1	3	5	10	50	100
Iteration number	31	25	22	20	18	18

Table 4.6: Number of GMRES iterations for $T = 0.2$ using $(\Delta t_f, \Delta t_s) = (0.025, 0.0125)$ and $\alpha_f = 1$.

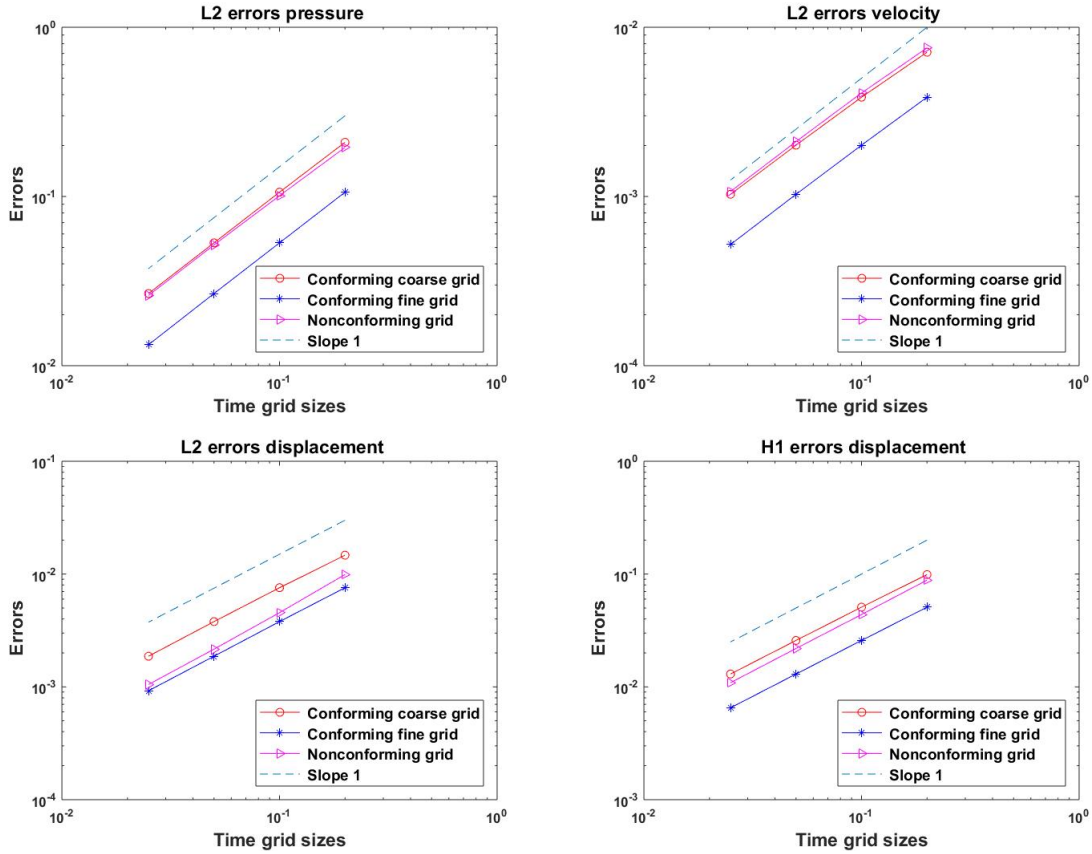

Figure 4.4: Errors at $T = 0.2$ by the Steklov-Poincaré method using Taylor-Hood and $\mathbf{P}2$ elements with $h = 1/32$.

4.3.2 Test 2 : Haemodynamic Experiment

In this example, we consider the blood flow problem reported in [73, 88]. The domain and the boundary conditions used for the computation are depicted in Figure 4.7. The force $\mathbf{b}(t)$ applied to the left fluid boundary in Figure 4.7 denotes the stress at the inlet at t seconds and is defined as:

$$\mathbf{b}(t) = \begin{cases} \left(-10^3 \left(1 - \cos \frac{2\pi t}{0.025}\right), 0\right) & t \leq 0.025 \\ (0,0)) & 0.025 < t < T. \end{cases}$$

The parameters used in this example are in accordance with the characteristics of blood flow in the human body. The density of the fluid, ρ_f, is 1 g/cm^3 and the viscosity of the fluid, ν_f, is 0.035 g/cm·s. The density of the structure, ρ_s, is 1.1 g/cm^3. The Young's Modulus of the structure, E,

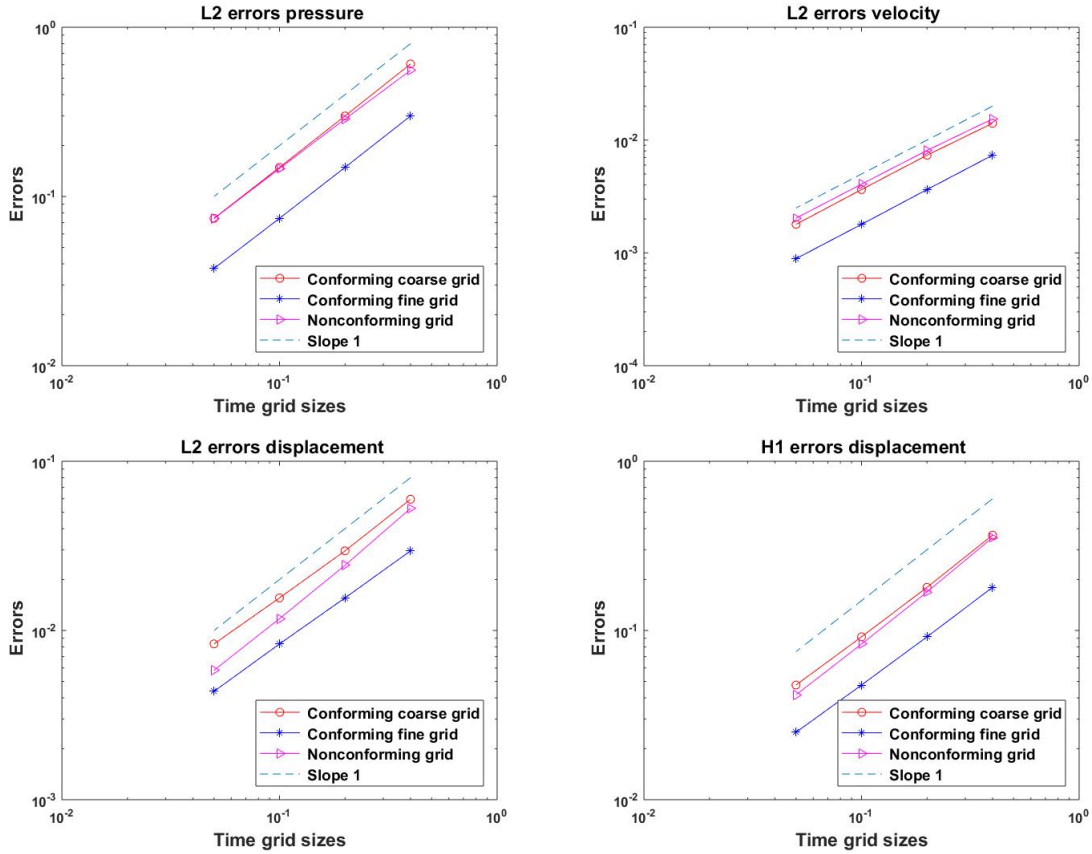

Figure 4.5: Errors at $T = 0.4$ by the Steklov-Poincaré method using MINI and $\mathbf{P}1$ elements with $h = 1/64$.

is 3×10^6 dyne/cm^2 and the Poisson ratio, ν, is 0.3. The Lame parameters λ and ν_s are defined as follows:

$$\lambda = \frac{\nu E}{(1-2\nu)(1+\nu)} \text{ dyne/cm}^2, \quad \nu_s = \frac{E}{2(1+\nu)} \text{dyne/cm}^2.$$

Both the fluid and structure have volume forces of $\mathbf{f}_s = \mathbf{f}_f = \mathbf{0}$ dyne/cm^2. Due to the closely matched densities between the fluid and the structure, the problem is significantly impacted by the added mass effect. Thus, when using a DD method at each time step, as in most DD approaches for FSI, additional relaxation steps may be necessary for solution stability, in addition to the use of a very fine time grid [88].

We simulate this example using the Steklov-Poincaré method without encountering the stability issue, as our local problems are still time-dependent. A uniform mesh is employed to spatially discretize the domains of both the fluid and structure, with h_x and h_y representing the

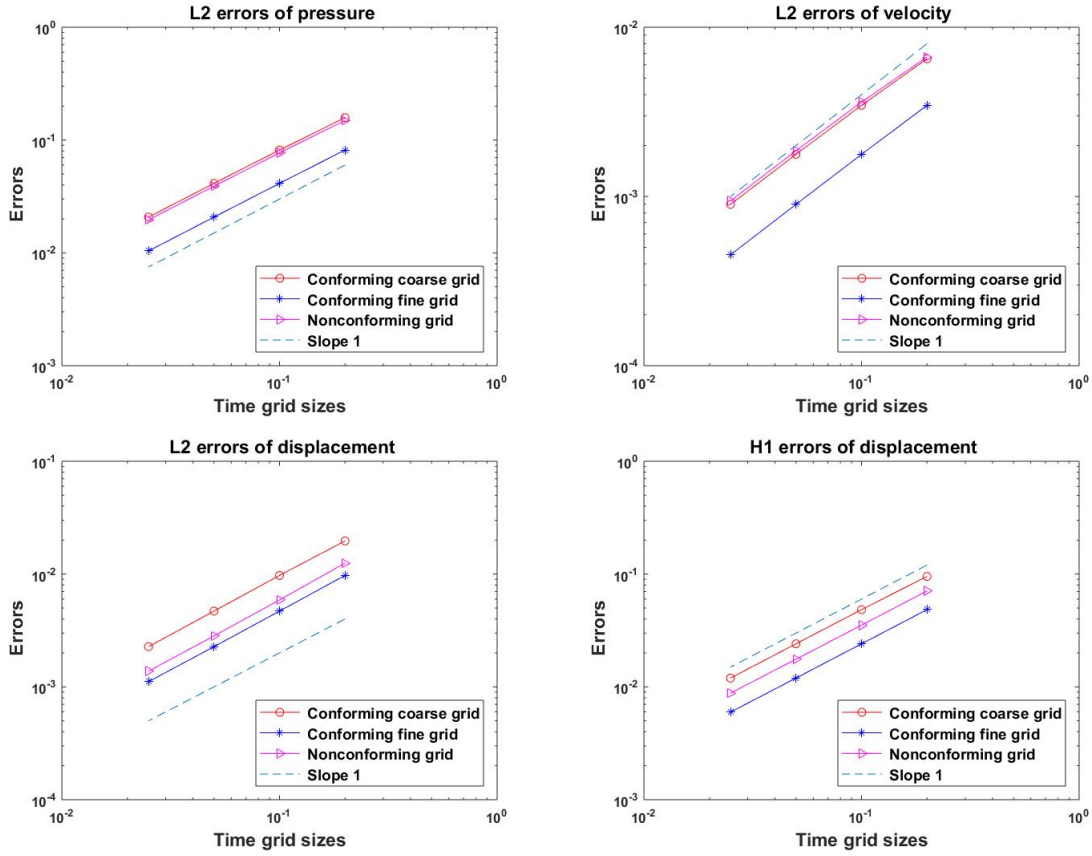

Figure 4.6: Errors at $T = 0.2$ by the Robin method ($\alpha_f = \alpha_s = 1$) using Taylor-Hood and $\mathbf{P}2$ elements with $h = 1/32$.

spatial discretization in the x and y directions. For this test, the fluid and structure are approximated using MINI elements and $\mathbf{P1}$ element, respectively. We use a time step of $\Delta t_f = 2 \times 10^{-4}$ for the fluid subdomain and $\Delta t_s = 1 \times 10^{-4}$ for the structure subdomain, with the final time set at $T = 0.1$. By setting $h_x = 0.1$ cm and changing h_y between 0.1 cm and $\frac{1}{30}$ cm, we monitor the vertical displacement at three distinct points on the interface (see Figure 4.8). We observe similar vertical displacement at each point for all values of h_y. In [73] and [88], it is observed that the solution heavily depends on spatial discretization, and the vertical displacements in Figure 4.8 are similar to their results obtained by fine spatial discretization. Furthermore, we report the interface velocity errors, $\frac{1}{2}\|\mathbf{u} - \dot{\boldsymbol{\eta}}\|_\Gamma^2$ for different mesh sizes of h_y in Table 4.7 at the final time $T = 0.1$ seconds.

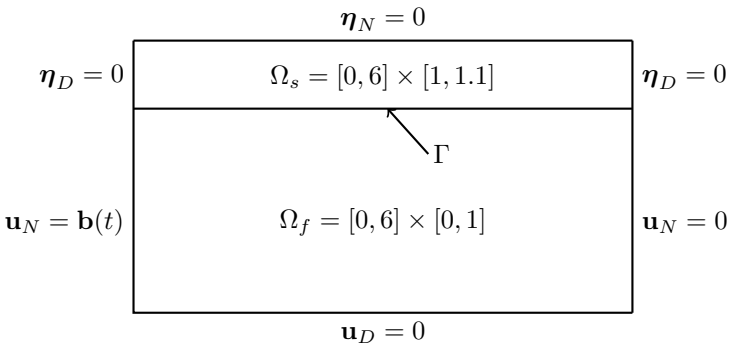

Figure 4.7: Domain and boundary conditions for Test2

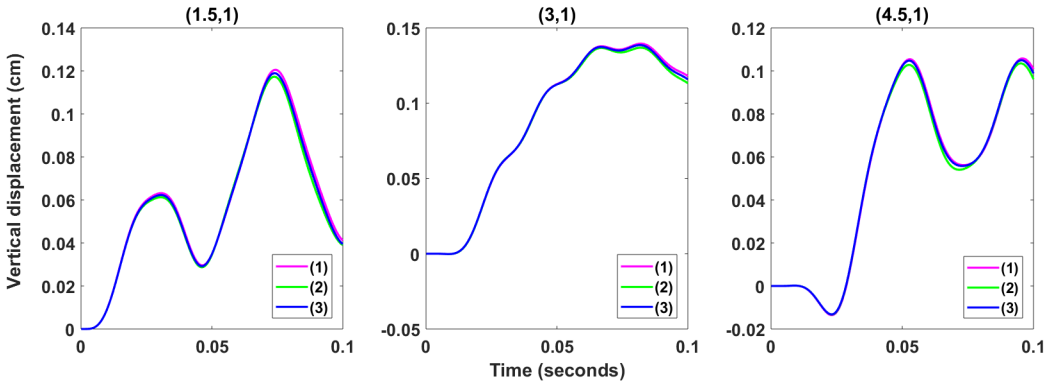

Figure 4.8: Vertical displacement at three points on the interface with: (1) $h_x = 0.1$ cm, $h_y = 0.1$ cm, (2) $h_x = 0.1$ cm, $h_y = 0.05$ cm, and (3) $h_x = 0.1$ cm, $h_y = \frac{1}{30}$ cm

Values of h_y	Interface Velocity Error
0.1	2.05e-04
0.05	8.23e-05
$\frac{1}{30}$	2.87e-05

Table 4.7: Errors in the continuity of velocity between subsystems for $h_x = 0.1$cm.

Part II

Fluid/Porous Structure

Chapter 5

Model Equations

Suppose the domain under consideration is made up of two regions $\Omega_f, \Omega_p \subset \mathbb{R}^d$, $d = 2, 3$, separated by the common interface $\Gamma = \partial\Omega_f \cap \partial\Omega_p$. The first region Ω_f is occupied by a free fluid flow and has the Lipschitz boundary $\partial\Omega_f = \Gamma_D^f \cup \Gamma$ and the second region Ω_p is occupied by a saturated porous structure with the Lipschitz boundary $\partial\Omega_p = \Gamma_N^p \cup \Gamma$ (see Figure 5.1). For the fluid flow in Ω_f we consider the Stokes equations with no-slip boundary condition on Γ_D^f:

$$\frac{\partial \mathbf{u}_f}{\partial t} - 2\nu_f \nabla \cdot D(\mathbf{u}_f) + \nabla p_f = \mathbf{f}_f \quad \text{in } \Omega_f \times (0,T)\,, \tag{5.0.1}$$

$$\nabla \cdot \mathbf{u}_f = 0 \quad \text{in } \Omega_f \times (0,T)\,, \tag{5.0.2}$$

$$\mathbf{u}_f = 0 \quad \text{on } \Gamma_D^f \times (0,T), \tag{5.0.3}$$

$$\mathbf{u}_f(\cdot, 0) = \mathbf{u}_{f0} \quad \text{in } \Omega_f, \tag{5.0.4}$$

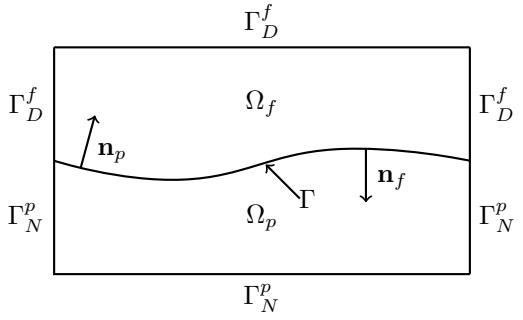

Figure 5.1: Stokes-Darcy domain

where $\mathbf{u}_f$ denotes the velocity vector, p_f the pressure, ν_f the fluid viscosity, $\mathbf{f}_f$ the body force acting on the fluid and $D(\mathbf{u}_f) := \frac{1}{2}\left(\nabla \mathbf{u}_f + (\nabla \mathbf{u}_f)^T\right)$ the rate of strain tensor. The porous medium flow is represented by the Darcy model with no-flux boundary condition on Γ_N^p:

$$\begin{aligned}
\mu_{eff}\mathbf{K}^{-1}\mathbf{u}_p + \nabla p_p &= 0 \quad \text{in } \Omega_p \times (0,T)\,, && (5.0.5)\\
\frac{\partial}{\partial t}(s_0 p_p) + \nabla \cdot \mathbf{u}_p &= f_p \quad \text{in } \Omega_p \times (0,T)\,, && (5.0.6)\\
\mathbf{u}_p \cdot \mathbf{n}_p &= 0 \quad \text{on } \Gamma_N^p \times (0,T), && (5.0.7)\\
p_p(\cdot,0) &= p_{p0} \quad \text{in } \Omega_p, && (5.0.8)
\end{aligned}$$

where p_p is the pore pressure, $\mathbf{u}_p$ the Darcy velocity and f_p the source/sink term. The constrained specific storage coefficient is denoted by s_0, μ_{eff} represents the effective fluid viscosity, and $\mathbf{K}$ the permeability tensor of the porous medium. In general, $\mathbf{K}$ is a symmetric positive definite tensor. For simplicity, we assume that $\mu_{eff}\mathbf{K}^{-1}$ is represented by $\nu_p\mathbf{I}$, i.e., $\mu_{eff}\mathbf{K}^{-1} := \nu_p\mathbf{I}$ for some scalar function ν_p.

In order to complete the Stokes-Darcy model, we impose the following interface conditions:

$$\begin{aligned}
\mathbf{u}_f \cdot \mathbf{n}_f + \mathbf{u}_p \cdot \mathbf{n}_p &= 0 \quad \text{on } \Gamma \times (0,T)\,, && (5.0.9)\\
\mathbf{n}_f \cdot (p_f\mathbf{I} - 2\nu_f D(\mathbf{u}_f)) \cdot \mathbf{n}_f &= p_p \quad \text{on } \Gamma \times (0,T)\,, && (5.0.10)\\
\mathbf{n}_f \cdot (p_f\mathbf{I} - 2\nu_f D(\mathbf{u}_f)) \cdot \mathbf{t}_j &= c_{BJS}\mathbf{u}_f \cdot \mathbf{t}_j, j = 1, ..., d-1 \quad \text{on } \Gamma \times (0,T), && (5.0.11)
\end{aligned}$$

where $\mathbf{n}_f$ and $\mathbf{n}_p$ denote outward unit normal vectors to Ω_f and Ω_p, respectively, $\mathbf{t}_j, j = 1, ..., d-1$ denote the orthogonal set of unit tangent vectors on Γ, and c_{BJS} denotes the resistance parameter in the tangential direction. The interface condition (5.0.9) enforces the continuity of the normal velocities, (5.0.10) enforces the continuity of the normal component of normal stress tensor and (5.0.11) is the Beavers-Joseph-Saffman condition [69]. These interface conditions suffice to precisely couple the Stokes system (5.0.1)-(5.0.4) to the Darcy system (5.0.5)-(5.0.8).

5.1 Function spaces and weak formulation

We use standard notation for Sobolev spaces, their associated norms and seminorms to define a weak formulation of the problem. For example, for an open domain $\Theta \subset \mathbb{R}^d$, $W^{m,p}(\Theta)$ is

the usual Sobolev space with the norm $\|\cdot\|_{m,p,\Theta}$. In case of $p = 2$, the Sobolev space $W^{m,2}(\Theta)$ is denoted by $H^m(\Theta)$ with the norm $\|\cdot\|_{m,\Theta}$. When $m = 0$, $H^m(\Theta)$ coincides with $L^2(\Theta)$. In this case, the inner product and the norm will be denoted by $(\cdot,\cdot)_\Theta$ and $\|\cdot\|_\Theta$, respectively. Moreover, if $\Theta = \Omega_f$ or Ω_p, and the context is clear, Θ will be omitted, i.e., $(\cdot,\cdot) = (\cdot,\cdot)_{\Omega_f}$ or $(\cdot,\cdot)_{\Omega_p}$ for functions defined in Ω_f and Ω_p. Finally, the associated space of vector valued functions will be denoted by a boldface font. Define the following function spaces for $(\mathbf{u}_f, p_f)$ and $(\mathbf{u}_p, p_p)$:

$$
\begin{aligned}
\mathbf{X}_f &:= \{\mathbf{v} \in \mathbf{H}^1(\Omega_f) : \ \mathbf{v} = \mathbf{0} \quad \text{on } \Gamma_D^f\},\\
Q_f &:= L^2(\Omega_f),\\
\mathbf{V}_f &:= \{\mathbf{v}_f \in \mathbf{X}_f : (q_f, \nabla\cdot\mathbf{v}_f) = 0, \forall q_f \in Q_f\},\\
\widehat{\mathbf{X}}_p &:= \{\mathbf{v} \in \mathbf{H}^{\mathrm{div}}(\Omega_p) : \mathbf{v}\cdot\mathbf{n}_p = 0 \quad \text{on } \Gamma_N^p\},\\
\mathbf{X}_p &:= \{\mathbf{v} \in \widehat{\mathbf{X}}_p : \mathbf{v}\cdot\mathbf{n} \mid_{\partial\Omega_p} \in L^2(\partial\Omega_p)\},\\
Q_p &:= L^2(\Omega_p),
\end{aligned}
$$

where $\mathbf{X}_p$ is equipped with the norm

$$\|\mathbf{v}\|^2_{\mathbf{X}_p} := \|\mathbf{v}\|^2_{\mathbf{H}^{\mathrm{div}}(\Omega_p)} + \|\mathbf{v}\cdot\mathbf{n}\|^2_{\partial\Omega_p}.$$

Note that $\mathbf{X}_p$ is a subspace of $\widehat{\mathbf{X}}_p$ with the additional regularity condition. The L^2-regularity of the normal trace of $\mathbf{v} \in \mathbf{X}_p$ is needed for the convergence proof presented in the next section. The spaces $\mathbf{X}_f$ and Q_f satisfy the inf-sup condition,

$$\inf_{q_f\in Q_f}\sup_{\mathbf{v}_f\in\mathbf{X}_f}\frac{(q_f,\nabla\cdot\mathbf{v}_f)}{\|q_f\|\|\nabla\mathbf{v}_f\|} \geq \beta > 0. \tag{5.1.1}$$

The dual spaces $\mathbf{X}_f^*$ and $\mathbf{V}_f^*$ are endowed with the following dual norms

$$\|\mathbf{w}\|_{\mathbf{X}_f^*} := \sup_{\mathbf{v}_f\in\mathbf{X}_f}\frac{(\mathbf{w},\mathbf{v}_f)}{\|\nabla\mathbf{v}_f\|}, \quad \|\mathbf{w}\|_{\mathbf{V}_f^*} := \sup_{v_f\in\mathbf{V}_f}\frac{(\mathbf{w},\mathbf{v}_f)}{\|\nabla\mathbf{v}_f\|}.$$

These norms are equivalent for functions in $\mathbf{V}_f$ as stated in the following lemma.

Lemma 5.1.1. *Let* $\mathbf{w} \in \mathbf{V}_f$. *Then, there exists* $C_* > 0$, *such that*

$$C_* \|\mathbf{w}\|_{\mathbf{X}_f^*} \leq \|\mathbf{w}\|_{\mathbf{V}_f^*} \leq \|\mathbf{w}\|_{\mathbf{X}_f^*}.$$

Proof. See Lemma 1 in [53]. □

For the variational formulation of the coupled Stokes-Darcy system, we introduce the Lagrange multiplier $\lambda \in \Lambda := H_{00}^{1/2}(\Gamma)$ [75] on the interface representing:

$$\lambda := \mathbf{n}_f \cdot (p_f \mathbf{I} - 2\nu_f D(\mathbf{u}_f)) \cdot \mathbf{n}_f = p_p \quad \text{on } \Gamma \times (0,T)\,. \tag{5.1.2}$$

Let Λ^* be the dual space of Λ. For $\gamma \subset \Gamma$, we use $\langle \cdot, \cdot \rangle_\Gamma$ to denote the duality pairing between Λ and Λ^*. The variational formulation for the Stokes-Darcy system (5.0.1)-(5.0.8) satisfying the interface conditions (5.0.9)-(5.0.11) reads as: given the initial conditions, find $(\mathbf{u}_f, p_f, \mathbf{u}_p, p_p, \lambda) \in (\mathbf{X}_f, Q_f, \widehat{\mathbf{X}}_p, Q_p, \Lambda)$, for a.e. $t \in (0,T)$, such that

$$\begin{aligned}
(\partial_t \mathbf{u}_f, \mathbf{v}_f) + 2\nu_f (D(\mathbf{u}_f), D(\mathbf{v}_f)) \; - \; & (p_f, \nabla \cdot \mathbf{v}_f) + \sum_{j=1}^{d-1} c_{BJS} (\mathbf{u}_f \cdot \mathbf{t}_j, \mathbf{v}_f \cdot \mathbf{t}_j)_\Gamma \\
&= (\mathbf{f}_f, \mathbf{v}_f) + \langle \lambda, \mathbf{v}_f \cdot \mathbf{n}_f \rangle_\Gamma \qquad \forall \mathbf{v}_f \in \mathbf{X}_f\,, \qquad (5.1.3)\\
(q_f, \nabla \cdot \mathbf{u}_f) &= 0 \qquad \forall q_f \in Q_f\,, \qquad (5.1.4)\\
\nu_p (\mathbf{u}_p, \mathbf{v}_p) - (p_p, \nabla \cdot \mathbf{v}_p) &= \langle \lambda, \mathbf{v}_p \cdot \mathbf{n}_p \rangle_\Gamma \qquad \forall \mathbf{v}_p \in \widehat{\mathbf{X}}_p\,, \qquad (5.1.5)\\
(q_p, s_0\, \partial_t p_p) + (q_p, \nabla \cdot \mathbf{u}_p) &= (f_p, q_p) \qquad \forall q_p \in Q_p\,, \qquad (5.1.6)\\
\langle \mathbf{u}_f \cdot \mathbf{n}_f + \mathbf{u}_p \cdot \mathbf{n}_p, \mu \rangle_\Gamma &= 0 \qquad \forall \mu \in \Lambda\,. \qquad (5.1.7)
\end{aligned}$$

The well-posedness of the mixed Stokes-Darcy model (5.1.3)-(5.1.7) can be found in [75] for the stationary case and is assumed to hold similarly for the non-stationary case. For the smooth solutions, the equivalence of the stationary Stokes-Darcy system and the variational formulation is discussed in [42].

Chapter 6

Global-in-time decoupling scheme

In this chapter we present a decoupling scheme for the Stokes-Darcy system based on global-in-time domain decomposition. We first rewrite the physical transmission conditions as equivalent Robin conditions and derive the associated space-time interface problem with two interface variables in Subsection 6.1. Such an interface problem is solved iteratively, using Jacobi iterations or GMRES. The former choice is equivalent to the SWR algorithm, which is presented and analyzed in Subsection 6.2.

6.1 Robin transmission conditions and the space-time interface problem

For the Robin transmission conditions on Γ, let α_f and α_p be positive parameters. Combining (5.0.9) and (5.0.10) linearly with coefficients $(-\alpha_f, 1)$ and $(\alpha_p, 1)$, we obtain the following two-sided Robin interface conditions on Γ [38]:

$$\mathbf{n}_f \cdot (p_f \mathbf{I} - 2\nu_f D(\mathbf{u}_f)) \cdot \mathbf{n}_f - \alpha_f \mathbf{u}_f \cdot \mathbf{n}_f = p_p + \alpha_f \mathbf{u}_p \cdot \mathbf{n}_p \quad \text{on } \Gamma \times (0,T)\,, \tag{6.1.1}$$

$$p_p - \alpha_p \mathbf{u}_p \cdot \mathbf{n}_p = \mathbf{n}_f \cdot (p_f \mathbf{I} - 2\nu_f D(\mathbf{u}_f)) \cdot \mathbf{n}_f + \alpha_p \mathbf{u}_f \cdot \mathbf{n}_f \quad \text{on } \Gamma \times (0,T). \tag{6.1.2}$$

If we let $g_f \in L^2(\Gamma)$ be a Robin condition for the Stokes equations with the parameter $\alpha_f > 0$ as in the left hand side of (6.1.1), the corresponding weak formulation is given as follows: find

$(\mathbf{u}_f, p_f) \in (\mathbf{X}_f, Q_f)$, for a.e. $t \in (0,T)$, such that

$$(\partial_t \mathbf{u}_f, \mathbf{v}_f) + 2\nu_f(D(\mathbf{u}_f), D(\mathbf{v}_f)) - (p_f, \nabla\cdot\mathbf{v}_f) + \sum_{j=1}^{d-1} c_{BJS}(\mathbf{u}_f\cdot\mathbf{t}_j, \mathbf{v}_f\cdot\mathbf{t}_j)_\Gamma$$
$$+\alpha_f(\mathbf{u}_f\cdot\mathbf{n}_f, \mathbf{v}_f\cdot\mathbf{n}_f)_\Gamma = (\mathbf{f}_f, \mathbf{v}_f) - (g_f, \mathbf{v}_f\cdot\mathbf{n}_f)_\Gamma \quad \forall \mathbf{v}_f \in \mathbf{X}_f\,, \tag{6.1.3}$$

$$(q_f, (\nabla\cdot\mathbf{u}_f) = 0 \quad \forall q_f \in Q_f\,, \tag{6.1.4}$$

$$(\mathbf{u}_f(\cdot,0), \mathbf{v}_f) = (\mathbf{u}_{f0}, \mathbf{v}_f) \quad \forall \mathbf{v}_f \in \mathbf{X}_f\,. \tag{6.1.5}$$

Similarly, considering $g_p \in L^2(\Gamma)$ as a Robin condition for the Darcy system with the parameter $\alpha_p > 0$ as in (6.1.2), we have the weak formulation given by: find $(\mathbf{u}_p, p_p) \in (\mathbf{X}_p, Q_p)$, for a.e. $t \in (0,T)$ satisfying

$$\nu_p(\mathbf{u}_p, \mathbf{v}_p) - (p_p, \nabla\cdot\mathbf{v}_p) + \alpha_p(\mathbf{u}_p\cdot\mathbf{n}_p, \mathbf{v}_p\cdot\mathbf{n}_p)_\Gamma = -(g_p, \mathbf{v}_p\cdot\mathbf{n}_p)_\Gamma \quad \forall \mathbf{v}_p \in \mathbf{X}_p\,, \tag{6.1.6}$$

$$(q_p, s_0\,\partial_t p_p) + (q_p, \nabla\cdot\mathbf{u}_p) = (f_p, q_p) \quad \forall q_p \in Q_p\,, \tag{6.1.7}$$

$$(p_p(\cdot,0), q_p) = (p_{p0}, q_p) \quad \forall q_p \in Q_p\,. \tag{6.1.8}$$

Remark 6.1.1. *From the Robin condition (6.1.2) with $g_p \in L^2(\Gamma)$ and by the definition of $\mathbf{X}_p$, the trace p_p is in $L^2(\Gamma)$. In fact if the test functions $\mathbf{v}_p$ in (6.1.6) are chosen to have compact support, then p_p is $H^1(\Omega_p)$ as shown in [64].*

Denote by $(\mathbf{u}_f, p_f) = \big(\mathbf{u}_f(g_f, \mathbf{f}_f, \mathbf{u}_{f0}), p_f(g_f, \mathbf{f}_f, \mathbf{u}_{f0})\big)$ the solution to the Stokes problem (6.1.3)-(6.1.5), and $(\mathbf{u}_p, p_p) = \big(\mathbf{u}_p(g_p, f_p, p_{p0}), p_p(g_p, f_p, p_{p0})\big)$ the solution to the Darcy problem (6.1.6)-(6.1.8). To derive the interface problem associated with the Robin conditions (6.1.1)-(6.1.2), we first define the interface operator:

$$\mathcal{R} : \Big(L^2(0,T;\, L^2(\Gamma))\Big)^2 \to \Big(L^2(0,T;\, L^2(\Gamma))\Big)^2,$$

such that

$$\mathcal{R}\begin{bmatrix} g_f \\ g_p \end{bmatrix} = \begin{bmatrix} g_p + (\alpha_p + \alpha_f)\left(\mathbf{u}_p(g_p, f_p, p_{p0})\cdot\mathbf{n}_p\right)|_\Gamma \\ g_f + (\alpha_f + \alpha_p)\left(\mathbf{u}_f(g_f, \mathbf{f}_f, \mathbf{u}_{f0})\cdot\mathbf{n}_f\right)|_\Gamma \end{bmatrix}. \tag{6.1.9}$$

Then the Robin transmission conditions (6.1.1)-(6.1.2) are equivalent to the following space-time

interface problem for two interface variables:

$$\mathcal{S}_{\mathcal{R}} \begin{bmatrix} g_f \\ g_p \end{bmatrix} = \chi_{\mathcal{R}} \quad \text{on } \Gamma \times (0,T), \tag{6.1.10}$$

where

$$\mathcal{S}_{\mathcal{R}} \begin{bmatrix} g_f \\ g_p \end{bmatrix} = \begin{bmatrix} g_f \\ g_p \end{bmatrix} - \begin{bmatrix} g_p + (\alpha_p + \alpha_f) \left(\mathbf{u}_p(g_p, 0, 0) \cdot \mathbf{n}_p \right) |_\Gamma \\ g_f + (\alpha_f + \alpha_p) \left(\mathbf{u}_f(g_f, \mathbf{0}, \mathbf{0}) \cdot \mathbf{n}_f \right) |_\Gamma \end{bmatrix},$$

and

$$\chi_{\mathcal{R}} = \begin{bmatrix} (\alpha_p + \alpha_f) \left(\mathbf{u}_p(0, f_p, p_{p0}) \cdot \mathbf{n}_p \right) |_\Gamma \\ (\alpha_f + \alpha_p) \left(\mathbf{u}_f(0, \mathbf{f}_f, \mathbf{u}_{f0}) \cdot \mathbf{n}_f \right) |_\Gamma \end{bmatrix}.$$

The weak form of (6.1.10) is given by: find $(g_f, g_p) \in \left(L^2(\Gamma)\right)^2$, for a.e. $t \in (0,T)$, such that

$$\int_0^T \int_\Gamma \left(\mathcal{S}_{\mathcal{R}} \begin{bmatrix} g_f \\ g_p \end{bmatrix} \cdot \begin{bmatrix} \xi_f \\ \xi_p \end{bmatrix} \right) d\gamma \, dt = \int_0^T \int_\Gamma \left(\chi_{\mathcal{R}} \cdot \begin{bmatrix} \xi_f \\ \xi_p \end{bmatrix} \right) d\gamma \, dt, \quad \forall \left(\xi_f, \xi_p\right) \in \left(L^2(\Gamma)\right)^2. \tag{6.1.11}$$

To carry out the convergence analysis of the proposed decoupling scheme, we solve the space-time interface problem (6.1.10) by Jacobi iterations, which is equivalent to the SWR algorithm and will be presented next. However, for the numerical experiments (cf. Section 7.3), we will use GMRES to solve the interface problem iteratively for faster convergence.

6.2 Schwarz waveform relaxation (SWR) algorithm and convergence analysis

Consider the following SWR algorithm based on Robin transmission conditions: at the kth iteration step we solve

$$\partial_t \mathbf{u}_f^k - \nabla \cdot (2\mu_f D(\mathbf{u}_f^k) - p_f^k \mathbf{I}) = \mathbf{f}_f \quad \text{in } \Omega_f \times (0,T), \tag{6.2.1}$$

$$\nabla \cdot \mathbf{u}_f^k = 0 \quad \text{in } \Omega_f \times (0,T), \tag{6.2.2}$$

$$\mathbf{n}_f^k \cdot (p_f^k \mathbf{I} - 2\nu_f D(\mathbf{u}_f^k)) \cdot \mathbf{n}_f - \alpha_f \mathbf{u}_f^k \cdot \mathbf{n}_f = p_p^{k-1} + \alpha_f \mathbf{u}_p^{k-1} \cdot \mathbf{n}_p \quad \text{on } \Gamma \times (0,T), \tag{6.2.3}$$

for (u_f^k, p_f^k) satisfying the initial and boundary conditions (5.0.3), (5.0.4) and the Beavers-Joseph-Saffman condition (5.0.11), and

$$\begin{aligned} \nu_p \mathbf{u}_p^k + \nabla p_p^k &= 0 \quad \text{in } \Omega_p \times (0,T)\,, && (6.2.4)\\ s_0 \partial_t p_p^k + \nabla \cdot \mathbf{u}_p^k &= \mathbf{f}_p \quad \text{in } \Omega_p \times (0,T)\,, && (6.2.5)\\ p_p^k - \alpha_p \mathbf{u}_p^k.\mathbf{n}_p &= \mathbf{n}_f \cdot (p_f^{k-1}\mathbf{I} - 2\nu_f D(\mathbf{u}_f^{k-1}))\mathbf{n}_f + \alpha_p \mathbf{u}_f^{k-1}.\mathbf{n}_f \quad \text{on } \Gamma \times (0,T)\,, && (6.2.6) \end{aligned}$$

for (u_p^k, p_p^k) satisfying (5.0.7) and (5.0.8). The weak formulation of this decoupled system is written as follows: at the kth iteration, find $(\mathbf{u}_f^k, p_f^k) \in (\mathbf{X}_f, Q_f)$ and $(\mathbf{u}_p^k, p_p^k) \in (\mathbf{X}_p, Q_p)$, for a.e. $t \in (0,T)$, such that

$$\begin{aligned} &(\partial_t \mathbf{u}_f^k, \mathbf{v}_f) + 2\nu_f (D(\mathbf{u}_f^k), D(\mathbf{v}_f)) - (p_f^k, \nabla \cdot \mathbf{v}_f) + \sum_{j=1}^{d-1} c_{BJS} (\mathbf{u}_f^k \cdot \mathbf{t}_j, \mathbf{v}_f \cdot \mathbf{t}_j)_\Gamma \\ &\quad + \alpha_f (\mathbf{u}_f^k \cdot \mathbf{n}_f, \mathbf{v}_f \cdot \mathbf{n}_f)_\Gamma = (\mathbf{f}_f, \mathbf{v}_f) - (p_p^{k-1} + \alpha_f \mathbf{u}_p^{k-1} \cdot \mathbf{n}_p, \mathbf{v}_f \cdot \mathbf{n}_f)_\Gamma \quad \forall \mathbf{v}_f \in \mathbf{X}_f\,, && (6.2.7)\\ &(q_f, \nabla \cdot \mathbf{u}_f^k) = 0 \quad \forall q_f \in Q_f\,, && (6.2.8) \end{aligned}$$

and

$$\begin{aligned} &\nu_p (\mathbf{u}_p^k, \mathbf{v}_p) - (p_p^k, \nabla \cdot \mathbf{v}_p^k) + \alpha_p (\mathbf{u}_p^k \cdot \mathbf{n}_p, \mathbf{v}_p \cdot \mathbf{n}_p)_\Gamma \\ &\qquad = -(\mathbf{n}_f \cdot (p_f^{k-1}\mathbf{I} - 2\nu_f D(\mathbf{u}_f^{k-1}))\mathbf{n}_f + \alpha_p \mathbf{u}_f^{k-1} \cdot \mathbf{n}_f, \mathbf{v}_p \cdot \mathbf{n}_p)_\Gamma \quad \forall \mathbf{v}_p \in \mathbf{X}_p\,, && (6.2.9)\\ &(q_p, s_0\, \partial_t p_p^k) + (q_p, \nabla \cdot \mathbf{u}_p^k) = (f_p, q_p) \quad \forall q_p \in Q_p\,. && (6.2.10) \end{aligned}$$

In the next theorem we prove the convergence of the proposed algorithm. The following identities will be used in the proof:

$$\begin{aligned} &(\mathbf{n}_f^k \cdot (p_f^k I - 2\nu_f D(\mathbf{u}_f^k)) \cdot \mathbf{n}_f - \alpha_f \mathbf{u}_f^k \cdot \mathbf{n}_f)^2 - (\mathbf{n}_f^k \cdot (p_f^k \mathbf{I} - 2\nu_f D(\mathbf{u}_f^k)) \cdot \mathbf{n}_f + \alpha_p \mathbf{u}_f^k \cdot \mathbf{n}_f)^2 \\ &\qquad = -2(\alpha_f + \alpha_p)(\mathbf{u}_f^k \cdot \mathbf{n}_f)(\mathbf{n}_f^k \cdot (p_f^k I - 2\nu_f D(\mathbf{u}_f^k)) \cdot \mathbf{n}_f) \\ &\qquad + (\alpha_f^2 - \alpha_p^2)(\mathbf{u}_f^k \cdot \mathbf{n}_f)^2\,, \end{aligned} \tag{6.2.11}$$

$$(p_p^k - \alpha_p \mathbf{u}_p^k \cdot \mathbf{n}_p)^2 - (p_p^k + \alpha_f \mathbf{u}_p^k \cdot \mathbf{n}_p)^2 = -2(\alpha_f + \alpha_p) p_p^k (\mathbf{u}_p^k \cdot \mathbf{n}_p) + (\alpha_p^2 - \alpha_f^2)(\mathbf{u}_p^k \cdot \mathbf{n}_p)^2\,. \tag{6.2.12}$$

Theorem 6.2.1. *Let $\mathbf{f}_f \in \boldsymbol{X}_f^{-1}, f_p \in Q_p$ and let $\alpha_f, \alpha_p \in \mathbb{R}$ be such that $\alpha_p \geq \alpha_f > 0$. If initial*

values $(\mathbf{u}_f^0, p_f^0, \mathbf{u}_p^0, p_p^0)$ *are chosen such that the Robin-Robin conditions (6.2.3), (6.2.6) are well-defined in* $L^2(\Gamma)$ *then the weak formulation (6.2.7)-(6.2.10) defines a unique sequence of iterates*

$$(\mathbf{u}_f^k, p_f^k, \mathbf{u}_p^k, p_p^k) \in L^\infty(0,T;\boldsymbol{X}_f) \times L^2(0,T;Q_f) \times L^2(0,T;\boldsymbol{X}_p) \times L^\infty(0,T;Q_p)$$

that converges to the weak solution $(\mathbf{u}_f, p_f, \mathbf{u}_p, p_p)$ *of problem (5.1.3)-(5.1.7).*

Proof. As the equations are linear, for the proof of convergence we can take $\mathbf{f}_f = \mathbf{u}_{f0} = \mathbf{0}$ and $f_p = p_{p0} = 0$, and show that the sequence $(\mathbf{u}_f^k, p_f^k, \mathbf{u}_p^k, p_p^k)$ of iterates converges to zero in suitable norms. The uniqueness of the sequence of iterates follows from the well-posedness of non-stationary Stokes-Darcy system.

Choosing $\mathbf{v}_f = \mathbf{u}_f^k$ and $q_f = p_f^k$ in (6.2.7)-(6.2.8) and adding two resulting equations yield

$$\begin{aligned}(\partial_t \mathbf{u}_f^k, \mathbf{u}_f^k) + 2\nu_f \|D(\mathbf{u}_f^k)\|_{\Omega_f}^2 + \sum_{j=1}^{d-1} c_{BJS} \|\mathbf{u}_f^k \cdot \mathbf{t}_j\|_\Gamma^2 + \alpha_f \|\mathbf{u}_f^k \cdot \mathbf{n}_f\|_\Gamma^2 \\ = -(p_p^{k-1} + \alpha_f \mathbf{u}_p^{k-1} \cdot \mathbf{n}_p, \mathbf{u}_f^k \cdot \mathbf{n}_f)_\Gamma.\end{aligned}$$

By using the Robin condition (6.2.3) and (6.2.11), we obtain

$$\begin{aligned}&(\partial_t \mathbf{u}_f^k, \mathbf{u}_f^k) + 2\nu_f \|D(\mathbf{u}_f^k)\|_{\Omega_f}^2 + \sum_{j=1}^{d-1} c_{BJS} \|\mathbf{u}_f^k \cdot \mathbf{t}_j\|_\Gamma^2 \\ &\qquad + \frac{1}{2(\alpha_f + \alpha_p)} \|\mathbf{n}_f \cdot (p_f^k \mathbf{I} - 2\nu_f D(\mathbf{u}_f^k)) \cdot \mathbf{n}_f + \alpha_p \mathbf{u}_f^k \cdot \mathbf{n}_f\|_\Gamma^2 \\ &= \frac{1}{2(\alpha_f + \alpha_p)} \|p_p^{k-1} + \alpha_f \mathbf{u}_p^{k-1} \cdot \mathbf{n}_p\|_\Gamma^2 + \frac{\alpha_p - \alpha_f}{2} \|\mathbf{u}_f^k \cdot \mathbf{n}_f\|_\Gamma^2.\end{aligned}$$

We integrate the above equation over $(0,t)$ for a.e. $t \in (0,T]$, and use the trace theorem, Korn's inequality and Young's inequality to obtain

$$\begin{aligned}&\frac{1}{2}\|\mathbf{u}_f^k(t)\|_{\Omega_f}^2 + 2\nu_f \int_0^t \|D(\mathbf{u}_f^k)\|_{\Omega_f}^2 \, ds + \sum_{j=1}^{d-1} c_{BJS} \int_0^t \|\mathbf{u}_f^k \cdot \mathbf{t}_j\|_\Gamma^2 \, ds \\ &\qquad + \frac{1}{2(\alpha_f + \alpha_p)} \int_0^t \|\mathbf{n}_f \cdot (p_f^k \mathbf{I} - 2\nu_f D(\mathbf{u}_f^k)) \cdot \mathbf{n}_f + \alpha_p \mathbf{u}_f^k \cdot \mathbf{n}_f\|_\Gamma^2 \, ds \\ &\leq \frac{1}{2(\alpha_f + \alpha_p)} \int_0^t \|p_p^{k-1} + \alpha_f \mathbf{u}_p^{k-1} \cdot \mathbf{n}_p\|_\Gamma^2 \, ds + \overline{C} \int_0^t \|\mathbf{u}_f^k(s)\|_{\Omega_f} \|D(\mathbf{u}_f^k(s))\|_{\Omega_f} \, ds \\ &\leq \frac{1}{2(\alpha_f + \alpha_p)} \int_0^t \|p_p^{k-1} + \alpha_f \mathbf{u}_p^{k-1} \cdot \mathbf{n}_p\|_\Gamma^2 \, ds + \overline{C} \int_0^t \left(\frac{1}{4\epsilon} \|\mathbf{u}_f^k(s)\|_{\Omega_f}^2 + \epsilon \|D(\mathbf{u}_f^k(s))\|_{\Omega_f}^2 \right) ds,\end{aligned}$$

for some constant $\overline{C} > 0$ and $\epsilon > 0$. Setting $\epsilon = \nu_f/\overline{C}$, we have

$$\begin{aligned}\frac{1}{2}\|\mathbf{u}_f^k(t)\|_{\Omega_f}^2 + \nu_f \int_0^t \|D(\mathbf{u}_f^k)\|_{\Omega_f}^2 \, ds + \sum_{j=1}^{d-1} c_{BJS} \int_0^t \|\mathbf{u}_f^k \cdot \mathbf{t}_j\|_\Gamma^2 \, ds \\ + \frac{1}{2(\alpha_f + \alpha_p)} \int_0^t \|\mathbf{n}_f \cdot (p_f^k \mathbf{I} - 2\nu_f D(\mathbf{u}_f^k)) \cdot \mathbf{n}_f + \alpha_p \mathbf{u}_f^k \cdot \mathbf{n}_f\|_\Gamma^2 \, ds \\ \leq \frac{1}{2(\alpha_f + \alpha_p)} \int_0^t \|p_p^{k-1} + \alpha_f \mathbf{u}_p^{k-1} \cdot \mathbf{n}_p\|_\Gamma^2 \, ds + C \int_0^t \|\mathbf{u}_f^k(s)\|_{\Omega_f}^2 \, ds \,, \end{aligned} \tag{6.2.13}$$

where $C = \frac{\overline{C}^2}{4\nu_f}$. Similarly, setting $\mathbf{v}_p = \mathbf{u}_p^k, q_p = p_p^k$ in (6.2.9)-(6.2.10), adding the resulting equations and using (6.2.12), we get

$$\begin{aligned}\nu_p \|\mathbf{u}_p^k\|_{\Omega_p}^2 + (s_0 \, \partial_t p_p^k, p_p^k) + \frac{1}{2(\alpha_f + \alpha_p)} \|p_p^k + \alpha_f \mathbf{u}_p^k \cdot \mathbf{n}_p\|_\Gamma^2 \\ \leq \frac{1}{2(\alpha_f + \alpha_p)} \|p_p^k - \alpha_p \mathbf{u}_p^k \cdot \mathbf{n}_p\|_\Gamma^2 - \frac{1}{2}(\alpha_p - \alpha_f) \|\mathbf{u}_p^k \cdot \mathbf{n}_p\|_\Gamma^2 \,. \end{aligned}$$

Suppose $\alpha_p \geq \alpha_f$ and let $\gamma := \frac{1}{2(\alpha_p - \alpha_f)} \geq 0$. Integrating over $(0, t)$ for a.e. $t \in (0, T]$ and applying the Robin boundary condition (6.2.6) imply

$$\begin{aligned}\nu_p \int_0^t \|\mathbf{u}_p^k(t)\|_{\Omega_p}^2 \, ds + \frac{s_0}{2} \|p_p^k(t)\|_{\Omega_p}^2 + \frac{1}{2(\alpha_f + \alpha_p)} \int_0^t \|p_p^k + \alpha_f \mathbf{u}_p^k \cdot \mathbf{n}_p\|_\Gamma^2 \, ds + \gamma \int_0^t \|\mathbf{u}_p^k \cdot \mathbf{n}_p\|_\Gamma^2 \, ds \\ \leq \frac{1}{2(\alpha_f + \alpha_p)} \int_0^t \|\mathbf{n}_f \cdot (p_f^{k-1} \mathbf{I} - 2\nu_f D(\mathbf{u}_f^{k-1})) \mathbf{n}_f + \alpha_p \mathbf{u}_f^{k-1} . \mathbf{n}_f\|_\Gamma^2 \, ds \,. \end{aligned} \tag{6.2.14}$$

We add (6.2.13) and (6.2.14), and define

$$\begin{aligned} E^k(t) &:= \frac{1}{2}\|\mathbf{u}_f^k(t)\|_{\Omega_f}^2 + \nu_f \int_0^t \|D(\mathbf{u}_f^k)\|_{\Omega_f}^2 \, ds + \sum_{j=1}^{d-1} c_{BJS} \int_0^t \|\mathbf{u}_f^k \cdot \mathbf{t}_j\|_\Gamma^2 \, ds \\ &\quad + \nu_p \int_0^t \|\mathbf{u}_p^k(t)\|_{\Omega_p}^2 \, ds + \frac{s_0}{2} \|p_p^k(t)\|_{\Omega_p}^2 + \gamma \int_0^t \|\mathbf{u}_p^k \cdot \mathbf{n}_p\|_\Gamma^2 \, ds \,, \\ B^k(t) &:= \frac{1}{2(\alpha_f + \alpha_p)} \int_0^t \|\mathbf{n}_f \cdot (p_f^k \mathbf{I} - 2\nu_f D(\mathbf{u}_f^k)) \mathbf{n}_f + \alpha_p \mathbf{u}_f^k . \mathbf{n}_f\|_\Gamma^2 \, ds \\ &\quad + \frac{1}{2(\alpha_f + \alpha_p)} \int_0^t \|p_p^k + \alpha_f \mathbf{u}_p^k \cdot \mathbf{n}_p\|_\Gamma^2 \, ds \,. \end{aligned}$$

Then, for all $k > 0$

$$E^k(t) + B^k(t) \leq B^{k-1}(t) + C \int_0^t \|\mathbf{u}_f^k(s)\|_{\Omega_f}^2 \, ds \,,$$

and summing over the iterates for any given $K > 0$ yields,

$$\sum_{k=1}^{K} E^k(t) \leq B^0(t) + C \sum_{k=1}^{K} \int_0^t \|\mathbf{u}_f^k(s)\|_{\Omega_f}^2 \, ds, \tag{6.2.15}$$

where

$$B^0(t) = \frac{1}{2(\alpha_f + \alpha_p)} \int_0^t \int_\Gamma g_0 \, ds,$$

for $g_0 = (\mathbf{n}_f \cdot (p_f^0 I - 2\nu_f D(\mathbf{u}_f^0))\mathbf{n}_f + \alpha_p \mathbf{u}_f^0.\mathbf{n}_f)^2 + (p_p^0 + \alpha_f \mathbf{u}_p^0 \cdot \mathbf{n}_p)^2$ obtained by the initial guess. Now, from the definition of $E^k(t)$ and (6.2.15),

$$\frac{1}{2} \sum_{k=1}^{K} \|\mathbf{u}_f^k(t)\|_{\Omega_f}^2 \leq B^0(t) + C \sum_{k=1}^{K} \int_0^t \|\mathbf{u}_f^k(s)\|_{\Omega_f}^2 \, ds.$$

Applying Gronwall's lemma, we obtain

$$\sum_{k=1}^{K} \|\mathbf{u}_f^k(t)\|_{\Omega_f}^2 \leq 2e^{2CT} B^0(T), \tag{6.2.16}$$

for any $K > 0$ and a.e. $t \in (0, T)$. The inequality (6.2.16) implies that $\mathbf{u}_f^k$ tends to 0 in $L^\infty(0, T; \mathbf{L^2}(\Omega_f))$ as $k \to \infty$, and the inequalities (6.2.15) and (6.2.16) yield

$$\sum_{k=1}^{K} \left(\nu_f \int_0^t \|D(\mathbf{u}_f^k)\|_{\Omega_f}^2 \, ds + \sum_{j=1}^{d-1} c_{BJS} \int_0^t \|\mathbf{u}_f^k \cdot \mathbf{t}_j\|_\Gamma^2 \, ds + \nu_p \int_0^t \|\mathbf{u}_p^k(t)\|_{\Omega_p}^2 \, ds + \frac{s_0}{2} \|p_p^k(t)\|_{\Omega_p}^2 \right.$$
$$\left. + \gamma \int_0^t \|\mathbf{u}_p^k \cdot \mathbf{n}_p\|_\Gamma^2 \, ds \right) \leq (1 + 2CTe^{2CT}) B^0(T) \quad \forall K > 0 \,. \tag{6.2.17}$$

The inequality (6.2.17) implies that $D(\mathbf{u}_f^k)$, $\mathbf{u}_f^k \cdot \mathbf{t}_j$, $\mathbf{u}_p^k$, p_p^k and $\mathbf{u}_p^k \cdot \mathbf{n}_p$ tend to 0 in $L^2(0, T; \mathbf{L}^2(\Omega_f))$, $L^2(0, T; L^2(\Gamma))$, $L^2(0, T; \mathbf{L}^2(\Omega_p))$, $L^\infty(0, T; L^2(\Omega_p))$ and $L^2(0, T; L^2(\Gamma))$, respectively, as $k \to \infty$.

For the convergence of p_f^k, we follow the technique used in [45]. We isolate the time derivative term in (6.2.7). Then for all $\mathbf{v}_f \in \mathbf{V}_f$:

$$\begin{aligned} (\partial_t \mathbf{u}_f^k, \mathbf{v}_f) \quad = \quad & -2\nu_f (D(\mathbf{u}_f^k), D(\mathbf{v}_f)) - \sum_{j=1}^{d-1} c_{BJS} (\mathbf{u}_f^k \cdot \mathbf{t}_j, \mathbf{v}_f \cdot \mathbf{t}_j)_\Gamma \\ & - \alpha_f (\mathbf{u}_f^k \cdot \mathbf{n}_f, \mathbf{v}_f \cdot \mathbf{n}_f)_\Gamma - (p_p^{k-1} + \alpha_f \mathbf{u}_p^{k-1} \cdot \mathbf{n}_p, \mathbf{v}_f \cdot \mathbf{n}_f)_\Gamma \,. \end{aligned} \tag{6.2.18}$$

For the bounds of right-hand side terms in (6.2.18) we use Cauchy-Schwarz inequality, the trace

theorem, Korn's inequality and Poincaré-Friedrichs inequality, divide both sides by $\left\|\nabla \mathbf{v}_f\right\|_{\Omega_f}$ and take supremum over $\mathbf{v}_f \in \mathbf{V}_f$. Then, for some constants $C_1, C_2, C_3, C_4 > 0$,

$$\begin{aligned}
\|\partial_t \mathbf{u}_f^k\|_{\mathbf{V}_f^*} &\leq 2\nu_f C_1 \|D(\mathbf{u}_f^k)\|_{\Omega_f} + C_2 \|D(\mathbf{u}_f^k)\|_{\Omega_f}^{1/2} \|\mathbf{u}_f^k\|_{\Omega_f}^{1/2} \\
&\quad + \sum_{j=1}^{d-1} c_{BJS} C_3 \|\mathbf{u}_f^k \cdot \mathbf{t}_j\|_\Gamma + C_4 \|p_p^{k-1} + \alpha_f \mathbf{u}_p^{k-1} \cdot \mathbf{n}_p\|_\Gamma \\
&\leq \frac{C_2}{2} \|\mathbf{u}_f^k\|_{\Omega_f} + \left(2\nu_f C_1 + \frac{C_2}{2}\right) \|D(\mathbf{u}_f^k)\|_{\Omega_f} + \sum_{j=1}^{d-1} c_{BJS} C_3 \|\mathbf{u}_f^k \cdot \mathbf{t}_j\|_\Gamma \\
&\quad + C_4 \|p_p^{k-1}\|_\Gamma + \alpha_f C_4 \|\mathbf{u}_p^{k-1} \cdot \mathbf{n}_p\|_\Gamma \,.
\end{aligned}$$

Setting $\widehat{C} = \max\{\frac{C_2}{2}, (2\nu_f C_1 + \frac{C_2}{2}), c_{BJS} C_3, C_4, \alpha_f C_4\}$, we have

$$\|\partial_t \mathbf{u}_f^k\|_{\mathbf{V}_f^*} \leq \widehat{C}(\|\mathbf{u}_f^k\|_{\Omega_f} + \|D(\mathbf{u}_f^k)\|_{\Omega_f} + \sum_{j=1}^{d-1} \|\mathbf{u}_f^k \cdot \mathbf{t}_j\|_\Gamma + \|p_p^{k-1}\|_\Gamma + \|\mathbf{u}_p^{k-1} \cdot \mathbf{n}_p\|_\Gamma) \,.$$

Lemma 5.1.1 then implies

$$\|\partial_t \mathbf{u}_f^k\|_{\mathbf{X}_f^*} \leq C_*^{-1} \widehat{C}(\|\mathbf{u}_f^k\|_{\Omega_f} + \|D(\mathbf{u}_f^k)\|_{\Omega_f} + \sum_{j=1}^{d-1} \|\mathbf{u}_f^k \cdot \mathbf{t}_j\|_\Gamma + \|p_p^{k-1}\|_\Gamma + \|\mathbf{u}_p^{k-1} \cdot \mathbf{n}_p\|_\Gamma) \,. \quad (6.2.19)$$

Now consider (6.2.7) with $\mathbf{v}_f \in \mathbf{X}_f$. We isolate pressure term, divide by $\|\nabla \mathbf{v}_f\|$, take supremum over $\mathbf{v}_f \in \mathbf{X}_f$ and use the inf-sup condition (5.1.1) and the estimate (6.2.19). Then, for some $\beta > 0$,

$$\beta \|p_f^k\|_{\Omega_f} \leq (1 + C_*^{-1} \widehat{C})(\|\mathbf{u}_f^k\|_{\Omega_f} + \|D(\mathbf{u}_f^k)\|_{\Omega_f} + \sum_{j=1}^{d-1} \|\mathbf{u}_f^k \cdot \mathbf{t}_j\|_\Gamma + \|p_p^{k-1}\|_\Gamma + \|\mathbf{u}_p^{k-1} \cdot \mathbf{n}_p\|_\Gamma) \,.$$

Square both sides and integrate over the interval $(0, t)$ for a.e. $t \in (0, T]$ to obtain

$$\frac{\beta^2}{C_d} \int_0^t \|p_f^k\|_{\Omega_f}^2 \, ds \leq \int_0^t (\|\mathbf{u}_f^k\|_{\Omega_f}^2 + \|D(\mathbf{u}_f^k)\|_{\Omega_f}^2 + \sum_{j=1}^{d-1} \|\mathbf{u}_f^k \cdot \mathbf{t}_j\|_\Gamma^2 + \|p_p^{k-1}\|_\Gamma^2 + \|\mathbf{u}_p^{k-1} \cdot \mathbf{n}_p\|_\Gamma^2) \, ds \,. \quad (6.2.20)$$

where $C_d = (d+3)(1 + C_*^{-1} \widehat{C})^2 > 0$. As $p_p^{k-1} \in H^1(\Omega_p)$ (see Remark 6.1.1), using the trace theorem

we have $\|p_p^{k-1}\|_\Gamma \le \|p_p^{k-1}\|^{1/2}_{\mathbf{H}^1(\Omega_p)} \|p_p^{k-1}\|^{1/2}_{\Omega_p}$. Thus (6.2.20) becomes

$$\begin{aligned}\frac{\beta^2}{C_d}\int_0^t \|p_f^k\|^2_{\Omega_f}\, ds \;\;\le\;\; & \int_0^t \big(\|\mathbf{u}_f^k\|^2_{\Omega_f} + \|D(\mathbf{u}_f^k)\|^2_{\Omega_f} + \sum_{j=1}^{d-1} \|\mathbf{u}_f^k \cdot \mathbf{t}_j\|^2_\Gamma \\ & + \|p_p^{k-1}\|_{\mathbf{H}^1(\Omega_p)} \|p_p^{k-1}\|_{\Omega_p} + \|\mathbf{u}_p^{k-1} \cdot \mathbf{n}_p\|^2_\Gamma \big)\, ds\,, \end{aligned} \tag{6.2.21}$$

where $\|p_p^{k-1}\|_{\mathbf{H}^1(\Omega_p)} < \infty$, since $p_p^{k-1} \in H^1(\Omega_p)$. Because $\mathbf{u}_f^k$, $D(\mathbf{u}_f^k)$, $\mathbf{u}_f^k \cdot \mathbf{t}_j$, p_p^k and $\mathbf{u}_p^k \cdot \mathbf{n}_p$ tend to 0 in $L^\infty(0,T;\mathbf{L}^2(\Omega_f))$, $L^2(0,T;\mathbf{L}^2(\Omega_f))$, $L^2(0,T;L^2(\Gamma))$, $L^\infty(0,T;L^2(\Omega_p))$ and $L^2(0,T;L^2(\Gamma))$, respectively, as $k \to \infty$, (6.2.21) implies $\int_0^t \|p_f^k\|^2 ds$ converges to 0 as $k \to \infty$. Hence p_f^k tends to 0 in $L^2(0,T;L^2(\Omega_f))$ as $k \to \infty$. □

Remark 6.2.2. *The choice of the Robin parameters, α_f and α_p, depends on the physical parameters of the problem and its discretization (i.e., the mesh size and time step size). For the case where a unique physics is considered on the whole domain, Robin parameters can be optimized by minimizing the convergence factor of the SWR algorithm in the Fourier transformed domain as proposed in [48]. Such an approach is called optimized Schwarz waveform relaxation (OSWR). For the stationary Stokes-Darcy system, optimization of the Robin parameters was studied in the framework of optimized Schwarz methods in [38, 49], again by means of Fourier analysis. However, for the time-dependent Stokes-Darcy coupling, it is not clear how to choose the Robin parameters in an optimal way; direct application of OSWR to the multiphysics system may not give desired numerical results in terms of accuracy of numerical solutions. We shall discuss various choices of the Robin parameters and their numerical performance in Section 7.3.*

Chapter 7

The semi-discrete, nonconforming in time, SWR algorithm

As the interface problem (6.1.11) is global-in-time, we can use different time step sizes in the Stokes and Darcy regions. The advantage of using nonconforming time grids is that time discretization can be selectively refined for a subproblem where the error in the solution is likely to be larger. In the following, we use L^2 projection functions to exchange data on the space-time interface between different time grids and prove the convergence of the time discretized SWR algorithm with nonconforming time grids.

7.1 Notation

Let τ_f be a partition of time interval $(0,T)$ into subintervals for the Stokes domain. We denote the time interval $(t_f^{m-1}, t_f^m]$ by J_f^m and the step size by $\Delta t_f^m := t_f^m - t_f^{m-1}$ for $m = 1, ..., M_f$. Denote the space of piecewise constant functions in time on grid τ_f with values in W by $P_0(\tau_f, W)$, where $W = L^2(\Gamma)$:

$$P_0(\tau_f, W) = \{\phi : (0,T) \to W, \phi \text{ is constant on } J_f^m \quad \forall m = 1, ..., M_f\}.$$

We define τ_p, M_p, J_p^n and Δt_p^n similarly for the Darcy domain. In order to exchange data on the space-time interface between different time grids, we define the L^2 projection $\Pi_{p,f}$ from $P_0(\tau_f, W)$

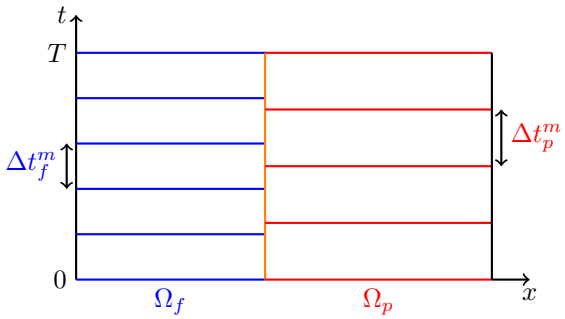

Figure 7.1: Nonconforming time grids.

onto $P_0(\tau_p, W)$ [64]:

$$\Pi_{p,f}(\phi)|_{J_p^n} = \frac{1}{|J_p^n|} \sum_{l=1}^{M_f} \int_{J_p^n \cap J_l^f} \phi.$$

The projection $\Pi_{f,p}$ from $P_0(\tau_p, W)$ onto $P_0(\tau_f, W)$ is also defined similarly.

7.2 The semi-discrete Stokes-Darcy system and convergence analysis of SWR algorithm

Using the backward Euler method, the semi-discrete Stokes-Darcy system with Robin transmission conditions on Γ is given by: for $m = 1, ..., M_f$

$$\mathbf{u}_f^m - \mathbf{u}_f^{m-1} + \Delta t_f^m(-2\mu_f \nabla \cdot D(\mathbf{u}_f^m) + \nabla p_f^m I) = \int_{J_f^m} \mathbf{f}_f \, dt \quad \text{in } \Omega_f \,, \tag{7.2.1}$$

$$\nabla \cdot \mathbf{u}_f^m = 0 \quad \text{in } \Omega_f \,, \tag{7.2.2}$$

$$\Delta t_f^m \left(\mathbf{n}_f \cdot (p_f^m \mathbf{I} - 2\nu_f D(\mathbf{u}_f^m)) \cdot \mathbf{n}_f - \alpha_f \mathbf{u}_f^m \cdot \mathbf{n}_f \right) = \int_{J_f^m} \Pi_{f,p} \left(p_p + \alpha_f \mathbf{u}_p \cdot \mathbf{n}_p \right) dt \text{ on } \Gamma, \tag{7.2.3}$$

and for $n = 1, ..., M_p$

$$\nu_p \mathbf{u}_p^n + \nabla p_p^n = 0 \quad \text{in } \Omega_p \,, \tag{7.2.4}$$

$$s_0(p_p^n - p_p^{n-1}) + \Delta t_p^n \nabla \cdot \mathbf{u}_p^n = \int_{J_p^n} f_p dt \quad \text{in } \Omega_p \,, \tag{7.2.5}$$

$$\Delta t_p^n \left(p_p^n - \alpha_p \mathbf{u}_p^n . \mathbf{n}_p \right) = \int_{J_p^n} \Pi_{p,f} \left(\mathbf{n}_f \cdot (p_f \mathbf{I} - 2\nu_f D(\mathbf{u}_f)) \mathbf{n}_f + \alpha_p \mathbf{u}_f \cdot \mathbf{n}_f \right) dt \quad \text{on } \Gamma, \tag{7.2.6}$$

where $(\mathbf{u}_f^k, p_f^k)$, satisfies (5.0.3), (5.0.11), $\mathbf{u}_f^0 = \mathbf{u}_{f0}$, $p_p^0 = p_{p0}$ and $\mathbf{u}_p^k$ satisfies (5.0.7). The semi-discrete SWR algorithm is then written as follows: in the kth iteration step, we solve

$$\mathbf{u}_f^{k,m} - \mathbf{u}_f^{k,m-1} - \Delta t_f^m \nabla \cdot (2\mu_f D(\mathbf{u}_f^{k.m}) - p_f^{k,m} I) = \int_{J_f^m} \mathbf{f}_f \, dt \quad \text{in } \Omega_f \,, \tag{7.2.7}$$

$$\nabla \cdot \mathbf{u}_f^{k,m} = 0 \quad \text{in } \Omega_f \,, \tag{7.2.8}$$

$$\Delta t_f^m \left(\mathbf{n}_f^k \cdot (p_f^{k,m} \mathbf{I} - 2\nu_f D(\mathbf{u}_f^{k,m})) \cdot \mathbf{n}_f - \alpha_f \mathbf{u}_f^{k,m} \cdot \mathbf{n}_f \right) = \int_{J_f^m} \Pi_{f,p} \left(p_p^{k-1} + \alpha_f \mathbf{u}_p^{k-1} \cdot \mathbf{n}_p \right) dt \quad \text{on } \Gamma \tag{7.2.9}$$

for $(\mathbf{u}_f^{k,m}, p_f^{k,m})$ satisfying (5.0.3), (5.0.11), where $\mathbf{u}_f^{k,0} = \mathbf{u}_{f0}$, $\mathbf{u}_f^{k,m} := \mathbf{u}_f^k|_{J_f^m}, p_f^{k,m} := p_f^k|_{J_f^m}$ for $m = 1, ..., M_f$, and

$$\nu_p \mathbf{u}_p^{k,n} + \nabla p_p^{k,n} = 0 \quad \text{in } \Omega_p \,, \tag{7.2.10}$$

$$s_0(p_p^{k,n} - p_p^{k,n-1}) + \Delta t_p^n \nabla \cdot \mathbf{u}_p^{k,n} = \int_{J_p^n} \mathbf{f}_p dt \quad \text{in } \Omega_p \,, \tag{7.2.11}$$

$$\Delta t_p^n \left(p_p^{k,n} - \alpha_p \mathbf{u}_p^{k,n} . \mathbf{n}_p \right) = \int_{J_p^n} \Pi_{p,f} \left(\mathbf{n}_f \cdot (p_f^{k-1} \mathbf{I} - 2\nu_f D(\mathbf{u}_f^{k-1})) \mathbf{n}_f + \alpha_p \mathbf{u}_f^{k-1} \cdot \mathbf{n}_f \right) dt \quad \text{on } \Gamma \tag{7.2.12}$$

for $(\mathbf{u}_p^{k,m}, p_p^{k,m})$ satisfying (5.0.7), where $p_p^{k,0} = p_{p0}$, $\mathbf{u}_p^{k,n} := \mathbf{u}_p^k|_{J_p^n}, p_p^{k,n} := p_p^k|_{J_p^n}$ for $n = 1, ..., M_p$. We show in the following theorem that as $k \to \infty$, the weak solution to (7.2.1)-(7.2.6) converges to the weak solution of (7.2.7)-(7.2.12).

Theorem 7.2.1. *Assume that $\alpha_f = \alpha_p > 0$. If initial guess values $(\mathbf{u}_f^0, p_f^0, \mathbf{u}_p^0, p_p^0)$ are chosen such that the Robin-Robin conditions (7.2.9), (7.2.12) are well-defined in $L^2(\Gamma)$, the weak formulation* (7.2.7)-(7.2.12) *defines a unique sequence of iterates*

$$(\mathbf{u}_f^k, p_f^k, \mathbf{u}_p^k, p_p^k) \in P_0(\tau_f; \boldsymbol{X}_f) \times P_0(\tau_f; Q_f) \times P_0(\tau_p; \boldsymbol{X}_p) \times P_0(\tau_p; Q_p)$$

that converges to the weak solution of (7.2.1)-(7.2.6).

Proof. As the equations are linear, we let $\mathbf{f}_f = \mathbf{u}_{f0} = \mathbf{0}$, $f_p = p_{p0} = 0$ and derive the energy estimates as in the proof of Theorem 6.2.1. First, we multiply (7.2.7), (7.2.8) by $\mathbf{u}_f^{k,m}$ and $p_f^{k,m}$, respectively, integrate them over Ω_f and use (5.0.11). Then add two resulting equations and use

(6.2.11) to obtain

$$
\begin{aligned}
&(\mathbf{u}_f^{k,m},\mathbf{u}_f^{k,m})_{\Omega_f}-(\mathbf{u}_f^{k,m-1},\mathbf{u}_f^{k,m})_{\Omega_f}+2\Delta t_f^m\nu_f\|D(\mathbf{u}_f^{k,m})\|_{\Omega_f}^2+\sum_{j=1}^{d-1}c_{BJS}\Delta t_f^m\|\mathbf{u}_f^{k,m}\cdot\mathbf{t}_j\|_{\Omega_f}^2\\
&\qquad+\frac{\Delta t_f^m}{2(\alpha_f+\alpha_p)}\|\mathbf{n}_f\cdot(p_f^{k,m}\mathbf{I}-2\nu_f D(\mathbf{u}_f^{k,m}))\cdot\mathbf{n}_f+\alpha_p\mathbf{u}_f^{k,m}\cdot\mathbf{n}_f\|_\Gamma^2\\
&\le\frac{\Delta t_f^m}{2(\alpha_f+\alpha_p)}\|\mathbf{n}_f\cdot(p_f^{k,m}\mathbf{I}-2\nu_f D(\mathbf{u}_f^{k,m}))\cdot\mathbf{n}_f-\alpha_f\mathbf{u}_f^{k,m}\cdot\mathbf{n}_f\|_\Gamma^2+\frac{\Delta t_f^m(\alpha_p-\alpha_f)}{2}\|\mathbf{u}_f^{k,m}\cdot\mathbf{n}_f\|_\Gamma^2.
\end{aligned}
$$

Using Cauchy-Schwarz inequality and $\frac{1}{2}(a^2-b^2)\le a^2-ab$, we obtain

$$
\begin{aligned}
&\frac{1}{2}\left(\|\mathbf{u}_f^{k,m}\|_{\Omega_f}^2-\|\mathbf{u}_f^{k,m-1}\|_{\Omega_f}^2\right)+\int_{J_f^m}2\nu_f\|D(\mathbf{u}_f^k)\|_{\Omega_f}^2\,dt+\sum_{j=1}^{d-1}c_{BJS}\int_{J_f^m}\|\mathbf{u}_f^k\cdot\mathbf{t}_j\|_{\Omega_f}^2\,dt\\
&\qquad+\frac{1}{2(\alpha_f+\alpha_p)}\int_{J_f^m}\|\mathbf{n}_f\cdot(p_f^k\mathbf{I}-2\nu_f D(\mathbf{u}_f^k))\cdot\mathbf{n}_f+\alpha_p\mathbf{u}_f^k\cdot\mathbf{n}_f\|_\Gamma^2\,dt\\
&\le\frac{1}{2(\alpha_f+\alpha_p)}\int_{J_f^m}\|\mathbf{n}_f\cdot(p_f^k\mathbf{I}-2\nu_f D(\mathbf{u}_f^k))\cdot\mathbf{n}_f-\alpha_f\mathbf{u}_f^k\cdot\mathbf{n}_f\|_\Gamma^2\,dt\\
&\qquad+\frac{\alpha_p-\alpha_f}{2}\int_{J_f^m}\|\mathbf{u}_f^k\cdot\mathbf{n}_f\|_\Gamma^2\,dt. \qquad (7.2.13)
\end{aligned}
$$

Similarly, multiply (7.2.10), (7.2.11) by $\mathbf{u}_p^{k,n}$ and $p_p^{k,n}$, respectively, integrate over Ω_p, add the two results and use (6.2.12) to have

$$
\begin{aligned}
&\nu_p\int_{J_p^n}\|\mathbf{u}_p^k\|_{\Omega_p}^2\,dt+\frac{s_0}{2}\left(\|p_p^{k,n}\|_{\Omega_p}^2-\|p_p^{k,n-1}\|_{\Omega_p}^2\right)+\frac{1}{2(\alpha_f+\alpha_p)}\int_{J_p^n}\|p_p^k+\alpha_f\mathbf{u}_p^k\cdot\mathbf{n}_p\|_\Gamma^2\,dt\\
&\qquad\le\frac{1}{2(\alpha_f+\alpha_p)}\int_{J_p^n}\|p_p^k-\alpha_p\mathbf{u}_p^k\cdot\mathbf{n}_p\|_\Gamma^2\,dt-\frac{\alpha_p-\alpha_f}{2}\int_{J_p^n}\|\mathbf{u}_p^k\cdot\mathbf{n}_p\|_\Gamma^2\,dt\,. \qquad (7.2.14)
\end{aligned}
$$

We cannot use Gronwall's lemma as in the continuous case because of the global-in-time projections $\Pi_{f,p}$ and $\Pi_{p,f}$. Hence, we make the assumption that $\alpha_f=\alpha_p$ to cancel the last terms of (7.2.13) and (7.2.14). Summing (7.2.13) and (7.2.14) over the subintervals in $(0,t_f^m]$ and $(0,t_p^n]$, respectively, yields

$$
\begin{aligned}
&\frac{1}{2}\|\mathbf{u}_f^{k,m}\|_{\Omega_f}^2+\int_0^{t_f^m}2\nu_f\|D(\mathbf{u}_f^k)\|_{\Omega_f}^2\,dt+\sum_{j=1}^{d-1}c_{BJS}\int_0^{t_f^m}\|\mathbf{u}_f^k\cdot\mathbf{t}_j\|_{\Omega_f}^2\,dt\\
&\qquad+\frac{1}{2(\alpha_f+\alpha_p)}\int_0^{t_f^m}\|\mathbf{n}_f\cdot(p_f^k\mathbf{I}-2\nu_f D(\mathbf{u}_f^k))\cdot\mathbf{n}_f+\alpha_p\mathbf{u}_f^k\cdot\mathbf{n}_f\|_\Gamma^2\,dt\\
&\le\frac{1}{2(\alpha_f+\alpha_p)}\int_0^{t_f^m}\|\mathbf{n}_f\cdot(p_f^k\mathbf{I}-2\nu_f D(\mathbf{u}_f^k))\cdot\mathbf{n}_f-\alpha_f\mathbf{u}_f^k\cdot\mathbf{n}_f\|_\Gamma^2\,dt, \qquad (7.2.15)
\end{aligned}
$$

and

$$\nu_p \int_0^{t_p^n} \|\mathbf{u}_p^k\|_{\Omega_p}^2 \, dt + \frac{s_0}{2}\|p_p^{k,n}\|_{\Omega_p}^2 + \frac{1}{2(\alpha_f+\alpha_p)} \int_0^{t_p^n} \|p_p^k + \alpha_f \mathbf{u}_p^k \cdot \mathbf{n}_p\|_\Gamma^2 \, dt$$
$$\leq \frac{1}{2(\alpha_f+\alpha_p)} \int_0^{t_p^n} \|p_p^k - \alpha_p \mathbf{u}_p^k \cdot \mathbf{n}_p\|_\Gamma^2 \, dt. \tag{7.2.16}$$

Adding (7.2.15) and (7.2.16), and using the Robin conditions (7.2.9) and (7.2.12), we obtain

$$\begin{aligned}
&\frac{1}{2}\|\mathbf{u}_f^{k,m}\|_{\Omega_f}^2 + \int_0^{t_f^m} 2\nu_f \|D(\mathbf{u}_f^k)\|_{\Omega_f}^2 \, dt + \sum_{j=1}^{d-1} c_{BJS} \int_0^{t_f^m} \|\mathbf{u}_f^k \cdot \mathbf{t}_j\|_{\Omega_f}^2 \, dt + \nu_p \int_0^{t_p^n} \|\mathbf{u}_p^k\|_{\Omega_p}^2 \, dt \\
&\quad + \frac{s_0}{2}\|p_p^{k,n}\|_{\Omega_p}^2 + \frac{1}{2(\alpha_f+\alpha_p)} \int_0^{t_p^n} \|p_p^k + \alpha_f \mathbf{u}_p^k \cdot \mathbf{n}_p\|_\Gamma^2 \, dt \\
&\quad + \frac{1}{2(\alpha_f+\alpha_p)} \int_0^{t_f^m} \|\mathbf{n}_f \cdot (p_f^k \mathbf{I} - 2\nu_f D(\mathbf{u}_f^k)) \cdot \mathbf{n}_f + \alpha_p \mathbf{u}_f^k \cdot \mathbf{n}_f\|_\Gamma^2 \, dt \\
&\leq \frac{1}{2(\alpha_f+\alpha_p)} \int_0^{t_f^m} \|\Pi_{f,p}(p_p^{k-1} + \alpha_f \mathbf{u}_p^{k-1} \cdot \mathbf{n}_p)\|_\Gamma^2 \, dt \\
&\quad + \frac{1}{2(\alpha_f+\alpha_p)} \int_0^{t_p^n} \|\Pi_{p,f}(\mathbf{n}_f \cdot (p_f^{k-1}\mathbf{I} - 2\nu_f D(\mathbf{u}_f^{k-1})) \cdot \mathbf{n}_f + \alpha_p \mathbf{u}_f^{k-1} \cdot \mathbf{n}_f)\|_\Gamma^2 \ \ dt \\
&\leq \frac{1}{2(\alpha_f+\alpha_p)} \int_0^{t_f^m} \|p_p^{k-1} + \alpha_f \mathbf{u}_p^{k-1} \cdot \mathbf{n}_p\|_\Gamma^2 \, dt \\
&\quad + \frac{1}{2(\alpha_f+\alpha_p)} \int_0^{t_p^n} \|\mathbf{n}_f \cdot (p_f^{k-1}\mathbf{I} - 2\nu_f D(\mathbf{u}_f^{k-1})) \cdot \mathbf{n}_f + \alpha_p \mathbf{u}_f^{k-1} \cdot \mathbf{n}_f\|_\Gamma^2 \, dt\,.
\end{aligned} \tag{7.2.17}$$

We set $m = M_f$ and $n = M_p$ then $t_f^{M_f} = t_p^{M_p} = T$. Now (7.2.17) becomes

$$\begin{aligned}
&\frac{1}{2}\|\mathbf{u}_f^{k,M_f}\|_{\Omega_f}^2 + \int_0^{T} 2\nu_f \|D(\mathbf{u}_f^k)\|_{\Omega_f}^2 \, dt + \sum_{j=1}^{d-1} c_{BJS} \int_0^{T} \|\mathbf{u}_f^k \cdot \mathbf{t}_j\|_{\Omega_f}^2 \, dt + \nu_p \int_0^{T} \|\mathbf{u}_p^k\|_{\Omega_p}^2 \, dtb \\
&\quad + \frac{s_0}{2}\|p_p^{k,M_p}\|_{\Omega_p}^2 + \frac{1}{2(\alpha_f+\alpha_p)} \int_0^{T} \|p_p^k + \alpha_f \mathbf{u}_p^k \cdot \mathbf{n}_p\|_\Gamma^2 \, dt \\
&\quad + \frac{1}{2(\alpha_f+\alpha_p)} \int_0^{T} \|\mathbf{n}_f \cdot (p_f^k \mathbf{I} - 2\nu_f D(\mathbf{u}_f^k)) \cdot \mathbf{n}_f + \alpha_p \mathbf{u}_f^k \cdot \mathbf{n}_f\|_\Gamma^2 \, dt \\
&\leq \frac{1}{2(\alpha_f+\alpha_p)} \int_0^{T} \|p_p^{k-1} + \alpha_f \mathbf{u}_p^{k-1} \cdot \mathbf{n}_p\|_\Gamma^2 \, dt \\
&\quad + \frac{1}{2(\alpha_f+\alpha_p)} \int_0^{T} \|\mathbf{n}_f \cdot (p_f^{k-1}\mathbf{I} - 2\nu_f D(\mathbf{u}_f^{k-1})) \cdot \mathbf{n}_f + \alpha_p \mathbf{u}_f^{k-1} \cdot \mathbf{n}_f\|_\Gamma^2 \, dt\,.
\end{aligned}$$

Then, for all $k > 0$

$$\frac{1}{2}\|\mathbf{u}_f^{k,M_f}\|_{\Omega_f}^2 + \int_0^T 2\nu_f \|D(\mathbf{u}_f^k)\|_{\Omega_f}^2 \, dt + \sum_{j=1}^{d-1} c_{BJS} \int_0^T \|\mathbf{u}_f^k \cdot \mathbf{t}_j\|_{\Omega_f}^2 \, dt$$
$$+\nu_p \int_0^T \|\mathbf{u}_p^k\|_{\Omega_p}^2 \, dt + \frac{s_0}{2}\|p_p^{k,M_p}\|_{\Omega_p}^2 + B^k \leq B^{k-1},$$

where

$$B^k = \frac{1}{2(\alpha_f + \alpha_p)} \int_0^T \|\mathbf{n}_f \cdot (p_f^k \mathbf{I} - 2\nu_f D(\mathbf{u}_f^k)) \cdot \mathbf{n}_f + \alpha_p \mathbf{u}_f^k \cdot \mathbf{n}_f\|_\Gamma^2 + \|p_p^k + \alpha_f \mathbf{u}_p^k \cdot \mathbf{n}_p\|_\Gamma^2 \, dt \,.$$

We sum over the iterates k to obtain that $\|\mathbf{u}_f^{k,M_f}\|_{\Omega_f}^2$, $\int_0^T \|D(\mathbf{u}_f^k)\|_{\Omega_f}^2 dt$, $\sum_{j=1}^{d-1}\int_0^T \|\mathbf{u}_f^k \cdot \mathbf{t}_j\|_{\Omega_f}^2 dt$, $\int_0^T \|\mathbf{u}_p^k\|_{\Omega_p}^2 dt$ and $\|p_p^{k,M_p}\|_{\Omega_p}^2$ converge to 0 as $k \to \infty$. This implies $\int_0^{t_f^m} \|D(\mathbf{u}_f^k)\|_{\Omega_f}^2 dt$, $\sum_{j=1}^{d-1}\int_0^{t_f^m} \|\mathbf{u}_f^k \cdot \mathbf{t}_j\|_{\Omega_f}^2 dt$ converge to 0 as $k \to \infty$ for $m = 1, ..., M_f$ and $\int_0^{t_p^n} \|\mathbf{u}_p^k\|_{\Omega_p}^2 dt$ converges to 0 as $k \to \infty$ for $n = 1, ..., M_p$. From Poincaré-Friedrichs inequality and Korn's inequality, we have $\|\mathbf{u}_f^{k,m}\|_{\Omega_f}^2 \leq \overline{C}_{PF}\|D(\mathbf{u}_f^{k,m})\|_{\Omega_f}^2$ for some constant $\overline{C}_{PF} > 0$. This implies $\int_0^{t_f^m} \|\mathbf{u}_f^k\|_{\Omega_f}^2 dt$ converges to 0 as $k \to \infty$ for $m = 1, ..., M_f$.

To show the convergence of $p_p^{k,n}$, we multiply (7.2.10) by $\nabla p_p^{k,m}$, integrate over Ω_p and use Cauchy-Schwarz inequality to obtain

$$\|\nabla p_p^{k,n}\|_{\Omega_p}^2 = -\nu_p(\mathbf{u}_p^{k,n}, \nabla p_p^{k,n}) \leq \nu_p \|\mathbf{u}_p^{k,n}\|_{\Omega_p} \|\nabla p_p^{k,n}\|_{\Omega_p} \,.$$

Since $p_p^{k,n} \in H^1(\Omega_p)$ (see remark 6.1.1), using Poincaré-Friedrichs inequality,

$$C_{PF}^{-1}\|p_p^{k,n}\|_{\Omega_p} \leq \|\nabla p_p^{k,n}\|_{\Omega_p} \leq \nu_p \|\mathbf{u}_p^{k,n}\|_{\Omega_p}, \tag{7.2.18}$$

for some constant $C_{PF} > 0$. Squaring all sides and integrating them over $(0, t_p^n]$, we have that $\int_0^{t_p^n} \|p_p^k\|_{\Omega_p}^2$ converges to 0 as $k \to \infty$ for $n = 1, ..., M_p$. Similarly, we multiply (7.2.11) by $\nabla \cdot \mathbf{u}_p^{k,n}$ and integrate over Ω_p to obtain

$$\Delta t_p^n \|\nabla \cdot \mathbf{u}_p^{k,n}\|_{\Omega_p}^2 \;=\; -(s_0(p_p^{k,n} - p_p^{k,n-1}), \nabla \cdot \mathbf{u}_p^{k,n})_{\Omega_p} \leq s_0 \|p_p^{k,n} - p_p^{k,n-1}\|_{\Omega_p} \|\nabla \cdot \mathbf{u}_p^{k,n}\|_{\Omega_p} \,,$$

which yields

$$\Delta t_p^n \|\nabla \cdot \mathbf{u}_p^{k,n}\|_{\Omega_p} \leq s_0 \|p_p^{k,n} - p_p^{k,n-1}\|_{\Omega_p} \leq s_0 \left(\|p_p^{k,n}\|_{\Omega_p} + \|p_p^{k,n-1}\|_{\Omega_p} \right).$$

Now, squaring all sides, integrating them over $(0, t_p^n]$ and the convergence of $\int_0^{t_p^n} \|p_p^k\|_{\Omega_p}^2$ yield that $\int_0^{t_p^n} \|\nabla \cdot \mathbf{u}_p^k\|_{\Omega_p}^2 dt$ converges to 0 as $k \to \infty$ for $n = 1, ..., M_p$. Also, this result together with the convergence of $\int_0^{t_p^n} \|\mathbf{u}_p^k\|_{\Omega_p}^2 dt$ implies that $\int_0^{t_p^n} \|\mathbf{u}_p^k\|_{\mathbf{H}^{\mathrm{div}}(\Omega_p)}^2 dt$ converges to 0 as $k \to \infty$ for $n = 1, ..., M_p$.

For the convergence of $p_f^{k,m}$ we multiply (7.2.7) by $\mathbf{v}_f \in \mathbf{V}_f$, integrate over Ω_f and proceed similarly to the continuous case to have

$$\begin{aligned} \frac{1}{\Delta t_f^m} \|\mathbf{u}_f^{k,m} - \mathbf{u}_f^{k,m-1}\|_{\mathbf{X}_f^{h*}} \quad \leq \quad & C_*^{-1} C(\|\mathbf{u}_f^{k,m}\|_{\Omega_f} + \|D(\mathbf{u}_f^{k,m})\|_{\Omega_f} + \sum_{j=1}^{d-1} \|\mathbf{u}_f^{k,m} \cdot \mathbf{t}_j\|_\Gamma \\ & + \|\Pi_{f,p}(p_p^{k-1,m} + \alpha_p \mathbf{u}_p^{k-1,m} \cdot \mathbf{n}_p)\|_\Gamma). \end{aligned} \tag{7.2.19}$$

Next, we multiply (7.2.7) by $\mathbf{v}_f \in \mathbf{X}_f$ and integrate over Ω_f. And then isolate the pressure term, divide by $\|\nabla \mathbf{v}_f\|$, take supremum over $\mathbf{v}_f \in \mathbf{X}_f$. Then, using the inf-sup condition (5.1.1) and estimate (7.2.19),

$$\begin{aligned} \beta \|p_f^{k,m}\|_{\Omega_f} \quad \leq \quad & (1 + C_*^{-1} C)(\|\mathbf{u}_f^{k,m}\|_{\Omega_f} + \|D(\mathbf{u}_f^{k,m})\|_{\Omega_f} \\ & + \sum_{j=1}^{d-1} \|\mathbf{u}_f^{k,m} \cdot \mathbf{t}_j\|_\Gamma + \|p_p^{k-1,m}\|_\Gamma + \alpha_p \|\mathbf{u}_p^{k-1,m} \cdot \mathbf{n}_p\|_\Gamma), \end{aligned}$$

for some $\beta > 0$. Square both sides and integrate over $(0, t_f^m]$. Then, for some $t_p^n \geq t_f^m$, we have

$$\begin{aligned} \beta^2 \int_0^{t_f^m} \|p_f^k\|_{\Omega_f}^2 \, dt \quad \leq \quad & (d+3)(1 + C_*^{-1} C)^2 \left(\int_0^{t_f^m} \|\mathbf{u}_f^k\|_{\Omega_f}^2 + \|D(\mathbf{u}_f^k)\|_{\Omega_f}^2 + \sum_{j=1}^{d-1} \|\mathbf{u}_f^k \cdot \mathbf{t}_j\|_\Gamma^2 \, dt \right. \\ & \left. + \int_0^{t_p^n} \|p_p^{k-1}\|_\Gamma^2 + \alpha_p \|\mathbf{u}_p^{k-1} \cdot \mathbf{n}_p\|_\Gamma^2 \, dt \right). \end{aligned} \tag{7.2.20}$$

As $p_p^{k-1} \in H^1(\Omega_p)$, using the trace theorem, we have $\|p_p^{k-1}\|_\Gamma \leq \|p_p^{k-1}\|_{\mathbf{H}^1(\Omega_p)}^{1/2} \|p_p^{k-1}\|_{\Omega_p}^{1/2}$. Also, using

$\|\mathbf{u}_p^{k-1}\cdot\mathbf{n}_p\|_\Gamma \le C\|\mathbf{u}_p^{k-1}\|_{\mathbf{H}^{\mathrm{div}}(\Omega_p)}$, (7.2.20) becomes

$$\begin{aligned}\beta^2\int_0^{t_f^m}\|p_f^k\|^2\,dt \;\le\; & C\left(\int_0^{t_f^m}\|\mathbf{u}_f^k\|_{\Omega_f}^2+\|D(\mathbf{u}_f^k)\|_{\Omega_f}^2+\sum_{j=1}^{d-1}\|\mathbf{u}_f^k\cdot\mathbf{t}_j\|_\Gamma^2\,dt\right.\\ &\left.+\int_0^{t_p^n}\|p_p^{k-1}\|_{\mathbf{H}^1(\Omega_p)}\|p_p^{k-1}\|_{\Omega_p}+\|\mathbf{u}_p^{k-1}\|_{\mathbf{H}^{\mathrm{div}}(\Omega_p)}^2\,dt\right). \qquad (7.2.21)\end{aligned}$$

As $p_p^{k-1}\in H^1(\Omega_p)$, $\|p_p^{k-1}\|_{\mathbf{H}^1(\Omega_p)}<\infty$. Therefore, the convergence of $\int_0^{t_f^m}\|p_f^k\|^2dt$ to 0 is obtained, since each term in the right hand side of (7.2.21) converges to 0 as $k\to\infty$ for $m=1,....,M_f$.

□

7.3 Numerical results

In this section, we consider two numerical tests to investigate the convergence and efficiency of the proposed global-in-time DD algorithm. The first numerical example is a manufactured problem where the exact solution is known. The second is a physical example where a flow is driven by a pressure drop. As mentioned in Subsection 6.1, GMRES is used in the numerical experiments to solve the space-time interface problem (6.1.11) iteratively. We shall verify the accuracy and convergence of the numerical solutions with decreasing grid sizes and time step sizes.

7.3.1 Test 1

We consider a test case with a known exact solution. The subdomains chosen are $\Omega_p=(0,1)\times(0,1)$ for the porous medium and $\Omega_f=(0,1)\times(1,2)$ for the fluid domain, with the interface $\Gamma=\{(x,y):0<x<1,y=1\}$. The exact solution is given by

$$\begin{aligned}\mathbf{u}_f &= [(y-1)^2x^3(1+t^2)\ ,\ -\cos(y)e(1+t^2)],\\ p_f &= (\cos(x)e^y+y^2-2y+1)(1+t^2),\\ \mathbf{u}_p &= [-x(\sin(y)e+2(y-1))(1+t^2)\ ,\ (-\cos(y)e+(y-1)^2)(1+t^2)],\\ p_p &= (-\sin(y)e+\cos(x)e^y+y^2-2y+1)(1+t^2),\end{aligned}$$

for which the Beavers-Joseph-Saffman condition is satisfied with $\alpha=1$. The model parameters are chosen as $\nu_f=1,\nu_p=1,s_0=1$. The initial and boundary conditions are imposed using the exact

solution. Two different finite element spaces were used for numerical simulations. First, we used Taylor-Hood elements for both $(\mathbf{u}_f, p_f)$ and $(\mathbf{u}_p, p_p$. As $\mathbf{u}_p \in H^{\text{div}}(\Omega_p)$, Taylor-Hood elements are not conforming for $(\mathbf{u}_p, p_p)$. Hence, the stabilization term $\gamma(\nabla \cdot \mathbf{u}_p, \nabla \cdot \mathbf{v}_p)$ was added to the Darcy equation (6.2.9) with $\gamma = 10$. Secondly, we used MINI elements for the Stokes and Raviart-Thomas of order one and P1 elements (RT1-P1) for the Darcy problem. The Robin parameters are chosen as $\alpha_f = 0.1$ and $\alpha_p = 50$. Test results using different values of Robin parameters will be discussed later. The tolerance for GMRES is set to be $\epsilon = 10^{-6}$.

First, we investigate the convergence of numerical solutions through spatial mesh refinement with nonconforming time grids. Table 7.1 and Table 7.2 show errors at $T = 0.01$ with $\Delta t_f = 0.002$ and $\Delta t_p = 0.001$ by Taylor-Hood elements for both the Stokes and Darcy problems and by MINI elements for the Stokes and RT1-P1 elements for Darcy problem, respectively. Note that for this non-physical example, the errors in the porous medium are larger, so we have chosen a small time step there while using a larger time step in the fluid domain. We observe from Tables 7.1 and 7.2 that the orders of accuracy in space are preserved with nonconforming time grids.

h		1/4	1/8	1/16	1/32
$\mathbf{u}_f$	L^2 error	8.34e-04	9.39e-05 [3.15]	1.15e-05 [3.03]	1.62e-06 [2.83]
	H^1 error	2.68e-02	5.81e-03 [2.21]	1.32e-03 [2.13]	3.38e-04 [1.97]
p_f	L^2 error	2.80e-02	5.53e-03 [2.34]	1.29e-03 [2.09]	3.91e-04 [1.73]
$\mathbf{u}_p$	L^2 error	1.11e-03	2.53e-04 [2.14]	3.84e-05 [2.72]	4.19e-06 [3.20]
	H^{div} error	2.11e-03	4.43e-04 [2.25]	9.55e-05 [2.21]	1.91e-05 [2.32]
p_p	L^2 error	2.31e-02	5.03e-03 [2.20]	1.26e-03 [1.99]	3.13e-04 [2.01]

Table 7.1: Errors at $T = 0.01$ by Taylor-Hood elements for the Stokes and Darcy problems using $(\Delta t_f, \Delta t_p) = (0.002, 0.001)$ and $(\alpha_f, \alpha_p) = (0.1, 50)$.

h		1/4	1/8	1/16	1/32
$\mathbf{u}_f$	L^2 error	9.60e-03	2.43e-03 [1.98]	5.49e-04 [2.15]	1.44e-04 [1.93]
	H^1 error	2.71e-01	1.29e-01 [1.07]	6.10e-02 [1.08]	3.15e-02 [0.95]
p_f	L^2 error	4.54e-01	1.06e-01 [2.10]	2.22e-02 [2.26]	5.63e-03 [1.98]
$\mathbf{u}_p$	L^2 error	1.99e-02	4.16e-03 [2.26]	1.01e-03 [2.04]	2.47e-04 [2.03]
	H^{div} error	2.26e-02	4.37e-03 [2.37]	1.06e-03 [2.03]	2.56e-04 [2.05]
p_p	L^2 error	2.26e-02	4.91e-03 [2.20]	1.23e-03 [1.99]	3.06e-04 [2.01]

Table 7.2: Errors at $T = 0.01$ by MINI elements for the Stokes and RT1-P1 elements for Darcy problem using $(\Delta t_f, \Delta t_p) = (0.002, 0.001)$ and $(\alpha_f, \alpha_p) = (0.1, 50)$.

We also performed convergence tests with respect to different time steps while keeping the

mesh size fixed, $h = 1/32$. We denote the coarse time step size by Δt_{coarse}. For Taylor-Hood elements, we use $\Delta t_{\text{coarse}} \in \{0.2, 0.1, 0.05, 0.0025\}$. In the case of MINI elements for the Stokes and RT1-P1 elements for the Darcy, we use $\Delta t_{\text{coarse}} \in \{0.8, 0.4, 0.2, 0.1\}$. The fine time step size is given by $\Delta t_{\text{fine}} = \Delta t_{\text{coarse}}/2$. Consider three types of time grids as follows:

1. Coarse conforming time grids: $\Delta t_f = \Delta t_p = \Delta t_{\text{coarse}}$,
2. Fine conforming time grids: $\Delta t_f = \Delta t_p = \Delta t_{\text{fine}}$,
3. Nonconforming time grids: $\Delta t_f = \Delta t_{\text{coarse}}$ and $\Delta t_p = \Delta t_{\text{fine}}$.

In Figure 7.2 we show the errors at $T = 0.2$ by Taylor-Hood elements using $\alpha_f = 0.1$ and $\alpha_p = 50$. Similarly Figure 7.3 presents errors by MINI elements and RT1-P1 elements at $T = 0.8$ using $\alpha_f = 0.1$ and $\alpha_p = 50$ on the fixed mesh $h = 1/64$. We observe that the first order convergence is preserved with the conforming and nonconforming time grids. The errors with nonconforming time grids in the porous medium are close to those with fine conforming time grids, which is expected, as a smaller time step is used in the porous medium. We also note that the H^{div} errors of Darcy velocity are very sensitive to the Robin parameters. In Figure 7.4 we compare H^{div} errors of Darcy velocity at $T = 0.2$ by Taylor-Hood elements using $\alpha_p = 50$ for different values of α_f. Similarly, in Figure 7.5, we compare H^{div} errors of Darcy velocity at $T = 0.2$ by Taylor-Hood elements using $\alpha_f = 0.1$ for different values of α_p. After performing experiments using various pairs of (α_f, α_p), we noticed that the first order convergence with respect to time is achieved if $\alpha_p \approx 500\alpha_f$ and $\alpha_f \leq 1$, which is the motivation for the choice of parameters $(\alpha_f, \alpha_p) = (0.1, 50)$ in most of our numerical tests. For very smaller values of α_f, we notice that the H^{div} errors of Darcy velocity for nonconforming case shift from conforming coarse to conforming fine on increasing α_p (see Figure 7.6). In Table 7.3 we compare the computer running time (in seconds) of conforming and nonconforming time grids for Taylor-Hood elements on the fixed mesh $h = 1/32$. Similarly, in Table 7.4, we compare the computer running time (in seconds) for MINI elements and RT1-P1 elements on the fixed mesh $h = 1/64$. We observe that using nonconforming time grids could significantly reduce the computational time while still maintaining the desired accuracy.

7.3.2 Test 2

In this example, we consider a flow driven by a pressure drop in the same domain as in Test1. Let $p_{\text{in}} = 1$ on the top boundary of Ω_f and $p_{\text{out}} = 0$ on the bottom boundary of Ω_p. We impose the

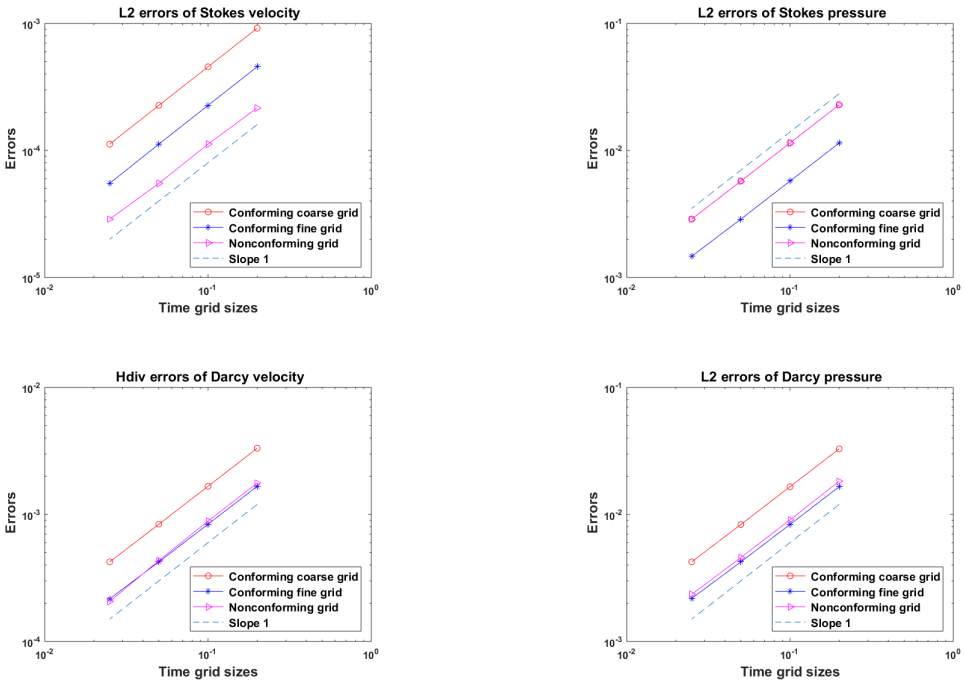

Figure 7.2: Errors for the Stokes and Darcy problems at T = 0.2 by Taylor-Hood elements using $(\alpha_f, \alpha_p) = (0.1, 50)$.

Δt	Conforming	Nonconforming
0.2	72	
		77
0.1	144	
		153
0.05	285	
		314
0.025	576	
		622
0.0125	1114	

Table 7.3: Comparison of the computer running times (in seconds) of conforming and nonconforming time grids with Taylor-Hood elements on fixed mesh $h = 1/32$ using $(\alpha_f, \alpha_p) = (0.1, 50)$.

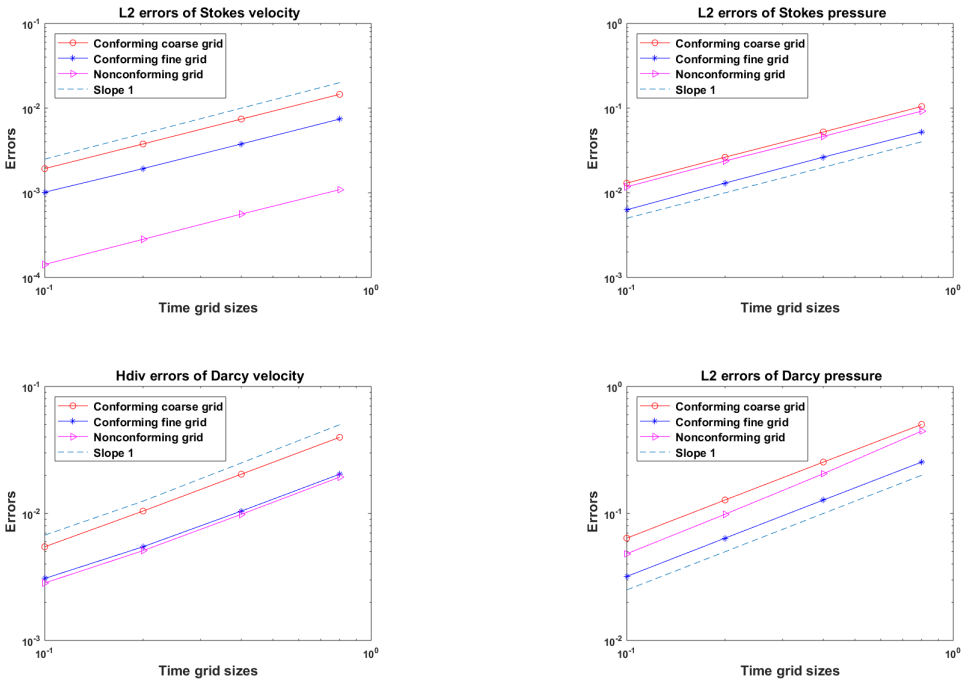

Figure 7.3: Errors by MINI elements for the Stokes and RT1-P1 elements for the Darcy problems at $T = 0.8$ using $(\alpha_f, \alpha_p) = (0.1, 50)$.

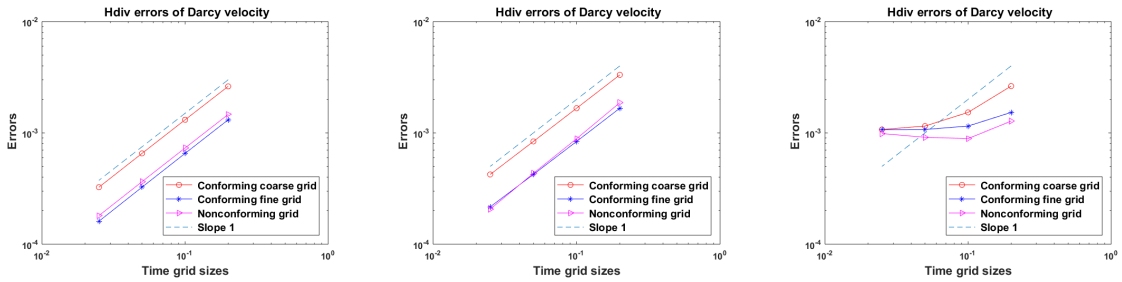

(a) $\alpha_f = 0.001$ (b) $\alpha_f = 0.1$ (c) $\alpha_f = 1$

Figure 7.4: H^{div} errors of Darcy velocity at T = 0.2 by Taylor-Hood elements using $\alpha_p = 50$ for different values of α_f.

no-slip boundary condition on the left and right boundaries of the Stokes's domain, and the initial Stokes velocity and the initial Darcy pressure are set to zero. The model parameters are selected as: $\nu_f = 1$, $\nu_p = 50$, $s_0 = 1$, $\alpha = 1$. The Robin parameters are chosen as $\alpha_f = 0.1$ and $\alpha_p = 50$, and the final time is set as $T = 1$. For this test, the Stokes and Darcy equations are approximated using MINI elements and RT1-P1 elements, respectively. To verify the convergence with respect to time with nonconforming time grids, we first compute the reference solution on the mesh size $h = 1/64$

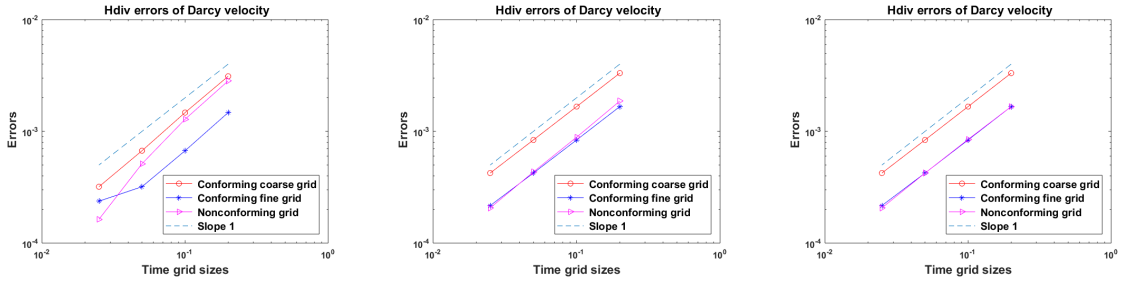

(a) $\alpha_p = 10$ (b) $\alpha_p = 50$ (c) $\alpha_p = 100$

Figure 7.5: H^{div} errors of Darcy velocity at T = 0.2 by Taylor-Hood elements using $\alpha_f = 0.1$ for different values of α_p.

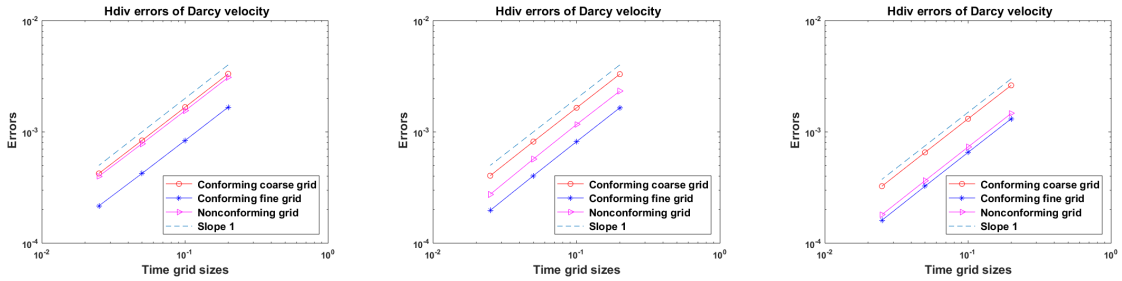

(a) $\alpha_p = 10$ (b) $\alpha_p = 25$ (c) $\alpha_p = 50$

Figure 7.6: H^{div} errors of Darcy velocity at T = 0.2 by Taylor-Hood elements using $\alpha_f = 0.001$ for different values of α_p.

and $\Delta t_{\text{ref}} = 0.01$ and calculate errors using the reference solution. The nonconforming time grids are chosen as $\Delta t_f = \Delta t_p/2$. Table 7.5 shows errors and convergence rates at $T = 1$ with the fixed mesh size $h = 1/64$, where first order convergence by nonconforming time grids is observed. In Table 7.6 and Table 7.7, we compare the accuracy in time of the conforming and nonconforming time grids. In particular, the errors (by nonconforming time grids) in the fluid domain are close to those by fine conforming time grids, while errors in the porous medium are close to those by coarse conforming time grids.

The velocity magnitude at $T = 1$ using $\Delta t_f = 1/16$ and $\Delta t_p = 1/8$ is shown in Figure 7.7. As defined in Section 5, $\nu_p \mathbf{I} = \nu_{\text{eff}} \mathbf{K}^{-1}$, where $\mathbf{K}$ is the permeability tensor of the porous medium. For some porous medium like clayey soil or clay the value of coefficients of permeability is around $10^{-5} - 10^{-4}$ meter per day; and about $10^{-8} - 10^{-2}$ meter per day for different kinds of sands [12, 72]. In Figure 7.8, we show the velocity magnitude at the final time for the porous medium with coefficients of permeability 10^{-5} assuming ν_{eff} to be unity.

Δt	Conforming	Nonconforming
0.8	1445	
		1446
0.4	2833	
		2871
0.2	5939	
		6457
0.1	10923	
		11244
0.05	22198	

Table 7.4: Comparison of the computer running times (in seconds) of conforming and nonconforming time grids with MINI elements for the Stokes and RT1-P1 element for the Darcy problems on fixed mesh $h = 1/64$ using $(\alpha_f, \alpha_p) = (0.1, 50)$.

Time steps		$\mathbf{u}_f$	p_f	$\mathbf{u}_p$	p_p
Δt_f	Δt_p	H^1 error	L^2 error	H^{div} error	L^2 error
1/4	1/2	2.61e-02	3.58e-02	6.31e-02	2.36e-02
1/8	1/4	1.49e-02 [0.81]	1.52e-02 [1.23]	3.42e-02 [0.88]	1.22e-02 [0.95]
1/16	1/8	7.59e-03 [0.97]	6.48e-03 [1.24]	1.66e-02 [1.04]	6.00e-03 [1.03]
1/32	1/16	3.38e-03 [1.16]	2.67e-03 [1.27]	7.46e-03 [1.15]	2.71e-03 [1.14]

Table 7.5: : Errors at $T = 1$ using $h = 1/64$ and $(\alpha_f, \alpha_p) = (0.1, 0.5)$.

Time grids	Δt_f	Δt_p	$\mathbf{u}_f$		p_f
			L^2 error	H^1 error	L^2 error
Conforming coarse	1/8	1/8	3.63e-03	1.23e-02	7.98e-03
Nonconforming	1/16	1/8	2.23e-03	7.59e-03	6.48e-03
Conforming fine	1/16	1/16	1.89e-03	6.45e-03	3.18e-03

Table 7.6: : Errors for the Stokes problem at $T = 1$ using $h = 1/64$ and $(\alpha_f, \alpha_p) = (0.1, 0.5)$.

Time grids	Δt_f	Δt_p	$\mathbf{u}_p$		p_p
			L^2 error	H^{div} error	L^2 error
Conforming coarse	1/8	1/8	1.07e-03	1.84e-02	6.73e-03
Nonconforming	1/16	1/8	9.87e-04	1.66e-02	6.00e-03
Conforming fine	1/16	1/16	5.24e-04	8.82e-03	3.09e-03

Table 7.7: : Errors for the Darcy problem at $T = 1$ using $h = 1/64$ and $(\alpha_f, \alpha_p) = (0.1, 0.5)$.

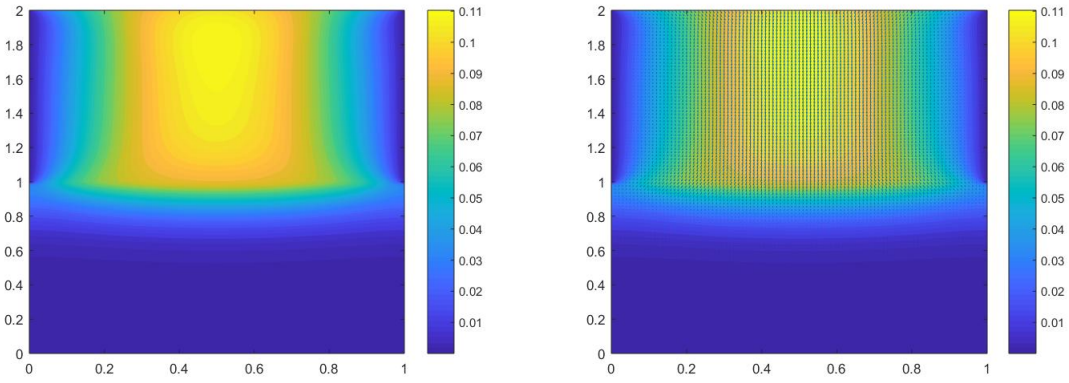

Figure 7.7: [Test case 2] Velocity magnitude and velocity vector at T = 1 for $\nu_p = 50$.

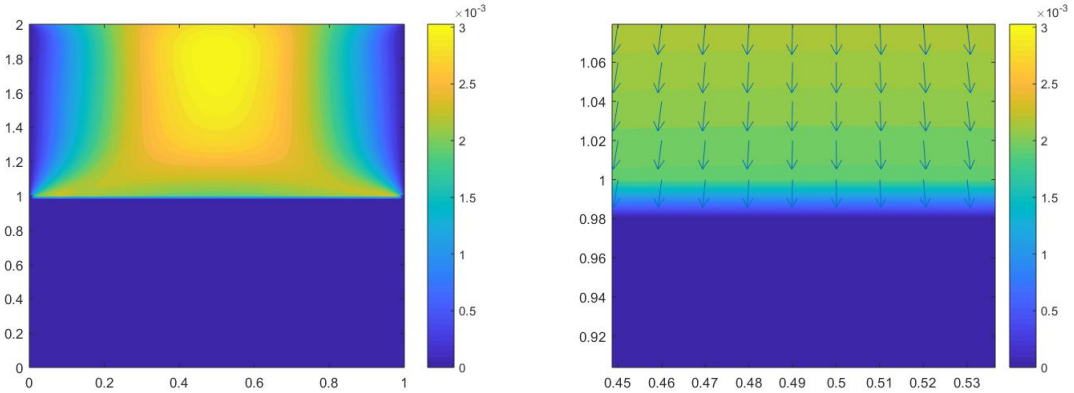

Figure 7.8: [Test case 2] Velocity magnitude and velocity vector near interface at T = 1 for $\nu_p = 10^5$.

Part III

Fluid/Poroelastic Structure

Chapter 8

Model equations

We consider a Lipschitz domain, $\Omega \in \mathbb{R}^d, d = 2, 3$, subdivided into two regions Ω^f and Ω^p, separated by a common moving interface Γ (See Figure 8.1). For Let $\mathbf{n}_\star$ denote outward unit normal vectors and $\Gamma^\star_N$ and $\Gamma^\star_D$ represent to the Neumann and Dirichelet boundaries, respectively to $\Omega^\star, \star \in \{f, p\}$. Note that in the interface, $\mathbf{n}_f = -\mathbf{n}_p$. The first region Ω^f is occupied by the free fluid and has boundary $\partial\Gamma^f$ such that $\partial\Gamma^f := \Gamma^f_N \cup \Gamma^f_D \cup \Gamma$ and the second region Ω^p is occupied by saturated poroelastic structure with the boundary $\partial\Gamma^p$ such that $\partial\Gamma^p := \Gamma^p_N \cup \Gamma^p_D \cup \Gamma$.

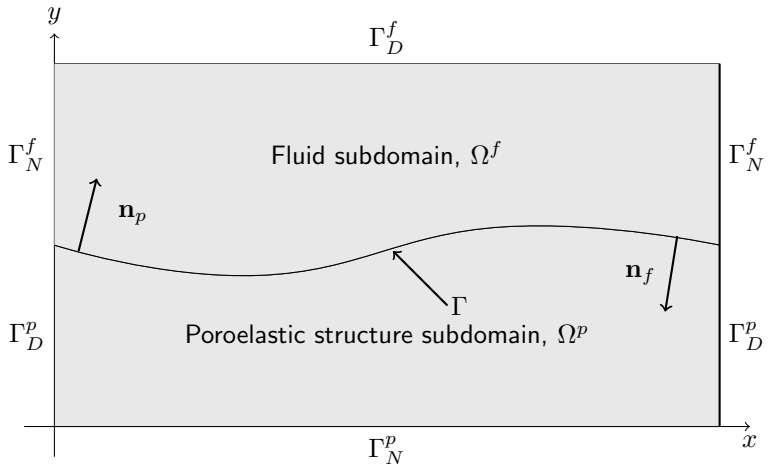

Figure 8.1: Fluid-poroelastic domain in $\mathbb{R}^2$

We assume that the flow in Ω^f is governed by the time-dependent non-linear Stokes equations. On defining $(\mathbf{u}_f, p_f)$ as a velocity-pressure pair in Ω^f, the fluid system is written as, for final

time $T > 0$:

$$\rho_f \frac{\partial \mathbf{u}_f}{\partial t} - \nabla \cdot \nu_f(|D(\mathbf{u}_f)|)\, D(\mathbf{u}_f) + \nabla p_f = \mathbf{f}_f \quad \text{in } \Omega^f \times (0,T)\,, \tag{8.0.1}$$

$$\nabla \cdot \mathbf{u}_f = 0 \quad \text{in } \Omega^f \times (0,T)\,, \tag{8.0.2}$$

$$\mathbf{u}_f(\mathbf{x},0) = \mathbf{u}_{f0}(\mathbf{x}) \quad \text{in } \Omega^f \tag{8.0.3}$$

where ρ_f is the density of the fluid, $\nu_f(|D(\mathbf{u}_f)|)$ is the fluid viscosity function, $\mathbf{f}_f$ represents the body force acting on the fluid, and $D(\mathbf{u}_f) := \frac{1}{2}\left(\nabla \mathbf{u}_f + (\nabla \mathbf{u}_f)^T\right)$ is the strain rate tensor. For the viscosity function, we consider Cross model given by:

$$\nu_f(|D(\mathbf{u}_f)|) = \nu_{f\infty} + \frac{\nu_{f0} - \nu_{f\infty}}{1 + K_f |D(\mathbf{u}_f)|^{2-r_f}}, \tag{8.0.4}$$

where $r_f > 1$ and $K_f > 0$ are constants. The constants $\nu_f\infty$ and ν_{f0} are limiting viscosity values at an infinite shear rate and at zero shear rate, respectively, such that $0 < \nu_{f\infty} \leq \nu_{f0}$. Further, we assume viscosity function $\nu_f(\cdot)$ to be monotonic and bounded and a nonlinear function $\mathbf{G(x)} := \nu_f(|\mathbf{x}|)\mathbf{x}$ to be uniformly continuous in $\mathbb{R}^d$. This assumption is used to show the well-posedness of the fluid-poroelastic system in [2].

Defining $(\mathbf{u}_p, p_p, \boldsymbol{\eta})$ as a velocity-pressure-displacement triplet in Ω^p, the poroelastic system is represented by the Biot model as:

$$\rho_s \frac{\partial^2 \boldsymbol{\eta}}{\partial t^2} - 2\nu_s \nabla \cdot D(\boldsymbol{\eta}) - \lambda \nabla(\nabla \cdot \boldsymbol{\eta}) + \alpha \nabla p_p = \mathbf{f}_s \quad \text{in } \Omega^p \times (0,T)\,, \tag{8.0.5}$$

$$\kappa^{-1}\mathbf{u}_p + \nabla p_p = 0 \quad \text{in } \Omega^p \times (0,T)\,, \tag{8.0.6}$$

$$\frac{\partial}{\partial t}(s_0 p_p + \alpha \nabla \cdot \boldsymbol{\eta}) + \nabla \cdot \mathbf{u}_p = f_p \quad \text{in } \Omega^p \times (0,T)\,, \tag{8.0.7}$$

$$\mathbf{u}_p(\mathbf{x},0) = \mathbf{u}_{p0}(\mathbf{x}) \quad \text{in } \Omega^p, \tag{8.0.8}$$

$$\boldsymbol{\eta}(\mathbf{x},0) = \boldsymbol{\eta}_0(\mathbf{x}) \quad \text{in } \Omega^p, \tag{8.0.9}$$

where f_p is the source/sink term, $\mathbf{f}_s$ is the body force, ν_s and λ denote the Lame parameters satisfying $0 < \lambda_{min} < \lambda(\mathbf{x}) < \lambda_{max}$ and $0 < \nu_{min} < \nu_s(\mathbf{x}) < \nu_{max}$. The density of saturated medium is denoted by ρ_s, and the hydraulic conductivity is denoted by κ. In general, κ is a symmetric positive definite

permeability tensor, satisfying, for some constants, $0 < \kappa_{min} < \kappa_{max}$,

$$\forall \boldsymbol{\zeta} \in \mathbb{R}^d, \quad \kappa_{min} \boldsymbol{\zeta}^T \boldsymbol{\zeta} \leq \boldsymbol{\zeta}^T \kappa(\mathbf{x}) \boldsymbol{\zeta} \leq \kappa_{max} \boldsymbol{\zeta}^T \boldsymbol{\zeta}, \quad \forall \mathbf{x} \in \Omega^p.$$

However in this work we assume an isotropic porous material so that κ is a scalar quantity. The constrained specific storage coefficient is denoted by s_0 and the Biot-Willis constant by α, which is usually close to unity. In the subsequent discussion, all the physical parameters are assumed to be constant in space and time. Note that the Biot system consists of the momentum equation for the balance of total forces (8.0.5) and the mass conservation equation (8.0.7), along with the standard assumption of Darcy's law (8.0.6) for the flux.

For the interface condition on the fluid-poroelastic interface, let $\boldsymbol{\sigma}_f(\mathbf{u}_f, p_f)$ denote the Cauchy stress tensor given by

$$\boldsymbol{\sigma}_f(\mathbf{u}_f, p_f) := \nu_f(|D(\mathbf{u}_f)|)\, D(\mathbf{u}_f) - p_f \mathbf{I},$$

and $\boldsymbol{\sigma}_p(\boldsymbol{\eta}, p_p)$ be the total stress tensor for the poroelastic structure given by

$$\boldsymbol{\sigma}_p(\boldsymbol{\eta}, p_p) := 2\nu_s D(\boldsymbol{\eta}) + \lambda(\nabla \cdot \boldsymbol{\eta})\mathbf{I} - \alpha\, p_p \mathbf{I}.$$

Then the fluid-poroelastic structure interaction system (8.0.1)-(8.0.9) is imposed with the following interface conditions:

$$\mathbf{u}_f \cdot \mathbf{n}_f = -\left(\frac{\partial \boldsymbol{\eta}}{\partial t} + \mathbf{u}_p\right) \cdot \mathbf{n}_p \quad \text{on } \Gamma \times (0,T), \tag{8.0.10}$$

$$\boldsymbol{\sigma}_f \mathbf{n}_f = -\boldsymbol{\sigma}_p \mathbf{n}_p \quad \text{on } \Gamma \times (0,T), \tag{8.0.11}$$

$$\boldsymbol{\sigma}_f \mathbf{n}_f \cdot \mathbf{n}_f = -p_p \quad \text{on } \Gamma \times (0,T), \tag{8.0.12}$$

$$\boldsymbol{\sigma}_f \mathbf{n}_f \cdot \mathbf{t}_j = -c_{BJS}\left(\mathbf{u}_f - \frac{\partial \boldsymbol{\eta}}{\partial t}\right) \cdot \mathbf{t}_j, j = 1, ..., d-1 \quad \text{on } \Gamma \times (0,T), \tag{8.0.13}$$

where $\mathbf{t}_j, j = 1, ..., d-1$ denote the orthogonal set of unit vectors on Γ, and c_{BJS} denotes the resistance parameter in the tangential direction. Here, (8.0.10) describes the continuity of the normal velocities. The conservation of momentum, expressed by (8.0.11), requires balance in the total stress of the fluid and porous medium. For the balance of normal stress across the interface,

we have (8.0.12). Finally, the tangential stress of the fluid is assumed to be proportional to the slip rate according to the Beavers-Joseph-Saffman condition (8.0.13). These interface conditions suffice to precisely couple the Stokes system (8.0.1)-(8.0.2) to the Biot system (8.0.5)-(8.0.7). The above system of equations needs to be complemented by a set of boundary conditions. We consider the following boundary conditions:

$$\boldsymbol{\sigma}_f \mathbf{n}_f = \tau_N \text{ on } \Gamma_N^f \times (0,T)\,, \qquad \mathbf{u}_f = \mathbf{0} \text{ on } \Gamma_D^f \times (0,T)\,,$$

$$\mathbf{u}_p \cdot \mathbf{n}_p = 0,\ \boldsymbol{\eta} = \mathbf{0} \text{ on } \Gamma_D^p \times (0,T)\,, \qquad p_p = 0,\ \boldsymbol{\sigma}_p \mathbf{n}_p = \mathbf{0} \text{ on } \Gamma_N^p \times (0,T)\,.$$

8.1 Function spaces and weak formulation

Now, we derive a weak formulation of the problem using a Lagrange multiplier. We use the standard notation for Sobolev spaces and their associated norms and seminorms. For m a non-negative integer and $\Theta \in \mathbb{R}^d$, Sobolev space, denoted by $H^m(\Theta)$, are Hilbert spaces with the norm $\|\cdot\|_{m,\Theta}$. We denote L^2 inner product and norm over Θ by $(\cdot,\cdot)_\Theta$ and $\|\cdot\|_\Theta$, respectively. Moreover, for functions defined in Ω^f and Ω^p, we simply use $(\cdot,\cdot) = (\cdot,\cdot)_{\Omega^f}$ or $(\cdot,\cdot)_{\Omega^p}$. For $\gamma \subset \mathbb{R}^{d-1}$, we use $\langle\cdot,\cdot\rangle_\gamma$ to denote the duality pairing between $H^{-1/2}(\gamma)$ and $H^{1/2}(\gamma)$. Finally, the associated space of vector-valued functions will be denoted by a boldface font. We now define the following function spaces:

$$\begin{aligned}
\mathbf{U}_f &:= \{\mathbf{v} \in \mathbf{H}^1(\Omega^f) :\ \mathbf{v} = \mathbf{0} \quad \text{on } \Gamma_D^f\}, \qquad Q_f := L^2(\Omega^f),\\
\mathbf{U}_p &:= \{\mathbf{v} \in \mathbf{L}^2(\Omega^p) : \nabla\cdot\mathbf{v} \in L^2(\Omega^p),\ \mathbf{v}\cdot\mathbf{n}_p = 0 \quad \text{on } \Gamma_D^p\}, \qquad Q_p := L^2(\Omega^p),\\
\boldsymbol{\Sigma}_p &:= \{\boldsymbol{\xi} \in \mathbf{H}^1(\Omega^p) :\ \boldsymbol{\xi} = \mathbf{0} \quad \text{on } \Gamma_D^p\}.
\end{aligned}$$

For the variational formulation, we introduce a Lagrange multiplier denoted by

$$\mathbf{g} := \boldsymbol{\sigma}_f \mathbf{n}_f = -\boldsymbol{\sigma}_p \mathbf{n}_p \quad \text{on } \Gamma \times (0,T),$$

such that $\mathbf{g} \in \mathbf{G} := \mathbf{H}^{1/2}(\Gamma)$. Further, we can rewrite it as

$$\mathbf{g} = (\mathbf{n}_f \cdot (\boldsymbol{\sigma}_f \mathbf{n}_f)|_\Gamma)\mathbf{n}_f + \sum_{j=1}^{d-1} (\mathbf{t}_j \cdot (\boldsymbol{\sigma}_f \mathbf{n}_f)|_\Gamma)\mathbf{t}_j,$$

which, together with (8.0.12), implies that

$$-p_p = \mathbf{n}_f \cdot \boldsymbol{\sigma}_f \mathbf{n}_f = \mathbf{g} \cdot \mathbf{n}_f = -\mathbf{g} \cdot \mathbf{n}_p \quad \text{on } \Gamma \times (0,T). \tag{8.1.1}$$

We now multiply the governing equations (8.0.1)-(8.0.2) and (8.0.5)-(8.0.7) by appropriate test functions, use integration by parts and (8.1.1) to obtain following continuous variational formulation: *given initial conditions, find* $(\mathbf{u}_f, p_f, \mathbf{u}_p, p_p, \boldsymbol{\eta}, \mathbf{g}) \in (\mathbf{U}_f, Q_f, \mathbf{U}_p, Q_p, \boldsymbol{\Sigma}, \mathbf{G})$*, for a.e.* $t \in (0,T)$*, such that*

$$\begin{aligned} \rho_f \left(\frac{\partial \mathbf{u}_f}{\partial t}, \mathbf{v}_f \right) + (\nu_f(|D(\mathbf{u}_f)|) D(\mathbf{u}_f), D(\mathbf{v}_f)) - (p_f, \nabla \cdot \mathbf{v}_f) \\ = (\mathbf{f}_f, \mathbf{v}_f) + \left\langle \tau_N, \mathbf{v}_f \right\rangle_{\Gamma_N^f} + \left\langle \mathbf{g}, \mathbf{v}_f \right\rangle_{\Gamma} \quad \forall \mathbf{v}_f \in \mathbf{U}_f \,, \end{aligned} \tag{8.1.2}$$

$$(q_f, \nabla \cdot \mathbf{u}_f) = 0, \quad \forall q_f \in Q_f \,. \tag{8.1.3}$$

and

$$\begin{aligned} \rho_s \left(\frac{\partial^2 \boldsymbol{\eta}}{\partial t^2}, \boldsymbol{\xi} \right) + 2\nu_s (D(\boldsymbol{\eta}), D(\boldsymbol{\xi})) + \lambda (\nabla \cdot \boldsymbol{\eta}, \nabla \cdot \boldsymbol{\xi}) - \alpha (p_p, \nabla \cdot \boldsymbol{\xi}) \\ = (\mathbf{f}_s, \boldsymbol{\xi}) - \langle \mathbf{g}, \boldsymbol{\xi} \rangle_{\Gamma}, \quad \forall \boldsymbol{\xi} \in \boldsymbol{\Sigma}_p \,, \end{aligned} \tag{8.1.4}$$

$$\kappa^{-1} (\mathbf{u}_p, \mathbf{v}_p) - (p_p, \nabla \cdot \mathbf{v}_p) = -\langle \mathbf{g} \cdot \mathbf{n}_p, \mathbf{v}_p \cdot \mathbf{n}_p \rangle_{\Gamma}, \quad \forall \mathbf{v}_p \in \mathbf{U}_p \,, \tag{8.1.5}$$

$$\left(q_p, \frac{\partial}{\partial t} (s_0 p_p + \alpha \nabla \cdot \boldsymbol{\eta}) + \nabla \cdot \mathbf{u}_p \right) = (q_p, f_p), \quad \forall q_p \in Q_p \,. \tag{8.1.6}$$

Chapter 9

Space-time interface problem and nested iteration algorithm

In this section, we use the physical transmission conditions to derive the associated space-time interface problem. First we introduce the interface operators I_{f1}, I_{f2}, I_{p1} and I_{p2} defined from $\mathbf{L}^2(0,T;\mathbf{G})$ to $\mathbf{L}^2(0,T;\mathbf{G}^*)$ as follows:

$$I_{f1}(\mathbf{g}) = \mathbf{g}\cdot\mathbf{t} + c_{BJS}\mathbf{u}_f(\mathbf{g})\cdot\mathbf{t}|_\Gamma, \quad I_{p1}(\mathbf{g}) = -c_{BJS}\frac{\partial\boldsymbol{\eta}(\mathbf{g})}{\partial t}\cdot\mathbf{t}|_\Gamma$$

$$I_{f2}(\mathbf{g}) = \mathbf{u}_f(\mathbf{g})\cdot\mathbf{n}_f|_\Gamma, \quad I_{p2}(\mathbf{g}) = \left(\frac{\partial\boldsymbol{\eta}(\mathbf{g})}{\partial t} + \mathbf{u}_p(\mathbf{g})\right)\cdot\mathbf{n}_p|_\Gamma$$

where $(\mathbf{u}_f(\mathbf{g}), p_f(\mathbf{g}))$ and $(\mathbf{u}_p(\mathbf{g}), p_p(\mathbf{g}), \boldsymbol{\eta}(\mathbf{g}))$ are the solutions to the Stokes problem (8.1.2)-(8.1.3) and the Biot problem (8.1.4)-(8.1.6) respectively. The interface conditions (8.0.11) and (8.0.12) are imposed through $\mathbf{g}$. However interface conditions (8.0.10) and (8.0.13) are not enforced in the formulation (8.1.2)-(8.1.6). This leads to the interface problem:
For a.e $t \in (0,T)$, *find* $\mathbf{g}(t) \in \mathbf{L}^2(0,T,\mathbf{G})$ *such that:*

$$\int_0^T \left(\langle I_{f1}(\mathbf{g}), \mathbf{v}\cdot\mathbf{t}\rangle + \langle I_{p1}(\mathbf{g}), \mathbf{v}\cdot\mathbf{t}\rangle\right) ds = 0, \forall\, \mathbf{v} \in \mathbf{L}^2(0,T,\mathbf{G}). \tag{9.0.1}$$

and

$$\int_0^T \left(\langle I_{f2}(\mathbf{g}), \mathbf{v}\cdot\mathbf{n}\rangle + \langle I_{p2}(\mathbf{g}), \mathbf{v}\cdot\mathbf{n}\rangle\right) ds = 0, \forall\, \mathbf{v} \in \mathbf{L}^2(0,T,\mathbf{G}). \tag{9.0.2}$$

For the nested iteration algorithm that can be used to solve this non-linear time-dependent interface problem, we use the solutions of the linearized Stokes-Biot system, which reads as follows: *given initial* $\mathbf{g}$*, find* $(\mathbf{w}_f, \phi_f, \mathbf{w}_p, \phi_p, \boldsymbol{\varphi}, \mathbf{h}) \in (\mathbf{U}_f, Q_f, \mathbf{U}_p, Q_p, \boldsymbol{\Sigma}_p, \mathbf{G})$*, for a.e.* $t \in (0,T)$*, such that*

$$\begin{aligned}\rho_f \left(\frac{\partial \mathbf{w}_f}{\partial t}, \mathbf{v}_f\right) &+ (\nu_f(|D(\mathbf{u}_f)|)D(\mathbf{w}_f), D(\mathbf{v}_f)) \\ &+ \left(\frac{(r_f-2)(\nu_{f0}-\nu_{f\infty})K_f}{(1+K_f|D(\mathbf{u}_f)|^{2-r_f})^2|D(\mathbf{u}_f)|^{r_f}} D(\mathbf{u}_f)(D(\mathbf{u}_f):D(\mathbf{w}_f)), D(\mathbf{v}_f)\right) \\ &-(\phi_f, \nabla\cdot\mathbf{v}_f) \\ &= -\left\langle \mathbf{h}, \mathbf{v}_f\right\rangle_\Gamma \quad \forall \mathbf{v}_f \in \mathbf{U}_f\,, \end{aligned} \tag{9.0.3}$$

$$(q_f, \nabla\cdot\mathbf{w}_f) = 0, \quad \forall q_f \in Q_f\,. \tag{9.0.4}$$

and

$$\begin{aligned}\rho_s \left(\frac{\partial^2 \boldsymbol{\varphi}}{\partial t^2}, \boldsymbol{\xi}\right) &+ 2\nu_s(D(\boldsymbol{\varphi}), D(\boldsymbol{\xi})) + \lambda(\nabla\cdot\boldsymbol{\varphi}, \nabla\cdot\boldsymbol{\xi}) - \alpha(\phi_p, \nabla\cdot\boldsymbol{\xi}) \\ &= \langle \mathbf{h}, \boldsymbol{\xi}\rangle_\Gamma, \quad \forall \boldsymbol{\xi} \in \boldsymbol{\Sigma}_p\,, \end{aligned} \tag{9.0.5}$$

$$\kappa^{-1}(\mathbf{w}_p, \mathbf{v}_p) - (\phi_p, \nabla\cdot\mathbf{v}_p) = -\langle \mathbf{h}\cdot\mathbf{n}_p, \mathbf{v}_p\cdot\mathbf{n}_p\rangle_\Gamma, \quad \forall \mathbf{v}_p \in \mathbf{U}_p\,, \tag{9.0.6}$$

$$\left(q_p, \frac{\partial}{\partial t}(s_0\phi_p + \alpha\nabla\cdot\boldsymbol{\varphi}) + \nabla\cdot\mathbf{w}_p\right) = 0, \quad \forall q_p \in Q_p\,. \tag{9.0.7}$$

Finally, for the nested iteration algorithm, we define the following linear operators from $\mathbf{L}^2(0,T;\mathbf{G})$ to $\mathbf{L}^2(0,T;\mathbf{G}^*)$:

$$L_{f1,\mathbf{g}}(\mathbf{h}) = \mathbf{h}\cdot\mathbf{t} + c_{BJS}\mathbf{w}_f(\mathbf{h})\cdot\mathbf{t}|_\Gamma\,,\; L_{p1,\mathbf{g}}(\mathbf{h}) = -c_{BJS}\frac{\partial\boldsymbol{\varphi}(\mathbf{h})}{\partial t}\cdot\mathbf{t}|_\Gamma$$

$$L_{f2,\mathbf{g}}(\mathbf{h}) = \mathbf{w}_f(\mathbf{h})\cdot\mathbf{n}_f|_\Gamma\,,\; L_{p2,\mathbf{g}}(\mathbf{h}) = \left(\frac{\partial\boldsymbol{\varphi}(\mathbf{h})}{\partial t} + \mathbf{w}_p(\mathbf{h})\right)\cdot\mathbf{n}_p|_\Gamma.$$

And operators Φ and $\Phi'(\mathbf{g})$ are defined as follows:

$$\Phi(\mathbf{g}) := \begin{bmatrix} I_{f1}(\mathbf{g}) + I_{p1}(\mathbf{g}) \\ I_{f2}(\mathbf{g}) + I_{p2}(\mathbf{g})\end{bmatrix}, \quad \Phi'(\mathbf{g})(\mathbf{h}) = \begin{bmatrix} L_{f1,\mathbf{g}}(\mathbf{h}) + L_{p1,\mathbf{g}}(\mathbf{h}) \\ L_{f2,\mathbf{g}}(\mathbf{h}) + L_{p2,\mathbf{g}}(\mathbf{h})\end{bmatrix} \tag{9.0.8}$$

and solve:

$$\int_0^T \langle \Phi'(\mathbf{g})(\mathbf{h}), \mathbf{v} \rangle_\Gamma \, ds = \int_0^T \langle -\Phi(\mathbf{g}), \mathbf{v} \rangle_\Gamma \, ds, \quad \forall \, \mathbf{v} \in \mathbf{L}^2(0, T; \Lambda). \tag{9.0.9}$$

Algorithm 1: Working algorithm

Input: $\mathbf{g}_0$ initial guess, ϵ tolerance and N_{iter} maximum number of iteration.

Output: $\mathbf{g}_k$

$k = 0$, error $= 0$

while $k < N_{\text{iter}}$ and error $> \epsilon$, **do**

1. Compute RHS of (9.0.9) by solving Stokes and Biot problem with $\mathbf{g} = \mathbf{g}_k$:

$$\Phi\left(\mathbf{g}_k\right) := \begin{bmatrix} I_{f1}(\mathbf{g}_k) + I_{p1}(\mathbf{g}_k) \\ I_{f2}(\mathbf{g}_k) + I_{p2}(\mathbf{g}_k) \end{bmatrix}.$$

2. Solve the following interface problem with a Krylov-type method:

$$\int_0^T \langle \Phi'(\mathbf{g}_k)(\mathbf{h}), \mathbf{v} \rangle_\Gamma \, ds = \int_0^T \langle -\Phi(\mathbf{g}_k), \mathbf{v} \rangle_\Gamma \, ds, \quad \forall \mathbf{v} \in \mathbf{L}^2(0, T; \Lambda),$$

where

$$\Phi'\left(\mathbf{g}_k\right)\left(\mathbf{h}_k\right) = \begin{bmatrix} L_{f1,\mathbf{g}_k}(\mathbf{h}_k) + L_{p1,\mathbf{g}_k}(\mathbf{h}) \\ L_{f2,\mathbf{g}_k}(\mathbf{h}_k) + L_{p2,\mathbf{g}_k}(\mathbf{h}) \end{bmatrix},$$

3. Update $\mathbf{g}_{k+1} = \mathbf{g}_k + \mathbf{h}_k, k = k + 1$, error $= \|h_k\|$

Chapter 10

Nonconforming discretization in time

As the interface problem (9.0.1)-(9.0.2) is global-in-time, we can use different time step sizes in the Stokes and Biot regions. The advantage of using nonconforming time grids is that time discretization can be selectively refined for a subproblem where the error in the solution is likely to be larger.

10.1 Notation

Let P_f be a partition of time interval $(0,T)$ into subintervals $T_f^m := (t_f^{m-1}, t_f^m]$ with step size $\Delta t_f^m := t_f^m - t_f^{m-1}$ for the Stokes domain where $m = 1, ..., M_f$. We denote the space of piecewise constant functions in time on grid P_f with values in K by $P_0(P_f, K)$:

$$P_0(P_f, K) = \{\phi : (0,T) \to K, \phi \,\text{is constant on}\, T_f^m \quad \forall m = 1, ..., M_f\}.$$

We define P_p, M_p, T_p^n and Δt_p^n similarly for the Biot domain. The interface problem (9.0.1)-(9.0.2) can be solved using various time discretization. The time-step in the interface does not need to match the time-steps used in fluid or the structure subdomain. Hence we define $P_\Gamma, M_\Gamma, T_\Gamma^k$ and Δt_Γ^k for the interface similarly. In order to exchange data on the space-time interface between different time grids, we define, for $\star \in \{f, p\}$, the following L^2 projection $\Pi_{\star,\Gamma}$ from $P_0(P_\Gamma, W)$ onto $P_0(P_\star, W)$

to :

$$\Pi_{\star,\Gamma}(\phi)|_{I_\star^s} = \frac{1}{|I_\star^s|}\sum_{l=1}^{M_\Gamma}\int_{I_\star^n\cap I_\Gamma^l}\phi, \text{ where } s=\{1,2,\cdots,M_\star\}.$$

The projection $\Pi_{\Gamma,\star}$ from $P_0(P_\star,W)$ onto $P_0(P_\Gamma,W)$ is also defined similarly.

10.2 The semi-discrete Stokes-Biot system

Using the backward Euler method, the semi-discrete Stokes-Biot system on Γ is given by: for $m=1,.....,M_f$

$$\rho_f\left(\frac{\mathbf{u}_f^m-\mathbf{u}_f^{m-1}}{\Delta t_f^m},\mathbf{v}_f\right)+(\nu_f(|D(\mathbf{u}_f^m)|)D(\mathbf{u}_f^m),D(\mathbf{v}_f))-(p_f^m,\nabla\cdot\mathbf{v}_f)$$
$$=(\mathbf{f}_f^m,\mathbf{v}_f)+\left\langle\tau_N^m,\mathbf{v}_f\right\rangle_{\Gamma_N^f}+\left\langle\mathbf{g}^m,\mathbf{v}_f\right\rangle_\Gamma\quad\forall\mathbf{v}_f\in\mathbf{U}_f\,, \tag{10.2.1}$$

$$(q_f,\nabla\cdot\mathbf{u}_f^m)=0,\quad\forall q_f\in Q_f\,. \tag{10.2.2}$$

and for $n=1,.....,M_p$

$$\rho_s\left(\frac{\boldsymbol{\eta}^n-2\boldsymbol{\eta}^{n-1}+\boldsymbol{\eta}^{n-2}}{(\Delta t_p^n)^2},\boldsymbol{\xi}\right)+2\nu_s(D(\boldsymbol{\eta}^n),D(\boldsymbol{\xi}))+\lambda(\nabla\cdot\boldsymbol{\eta}^n,\nabla\cdot\boldsymbol{\xi})-\alpha(p_p^n,\nabla\cdot\boldsymbol{\xi})$$
$$=(\mathbf{f}_s^n,\boldsymbol{\xi})-\langle\mathbf{g}^n,\boldsymbol{\xi}\rangle_\Gamma,\quad\forall\boldsymbol{\xi}\in\boldsymbol{\Sigma}_p\,, \tag{10.2.3}$$

$$\kappa^{-1}(\mathbf{u}_p^n,\mathbf{v}_p)-(p_p^n,\nabla\cdot\mathbf{v}_p)=-\langle\mathbf{g}^n\cdot\mathbf{n}_p,\mathbf{v}_p\cdot\mathbf{n}_p\rangle_\Gamma,\quad\forall\mathbf{v}_p\in\mathbf{U}_p\,, \tag{10.2.4}$$

$$\left(q_p,s_0\frac{p_p^n-p_p^{n-1}}{\Delta t_p^n}+\alpha\frac{\nabla\cdot\boldsymbol{\eta}^n-\nabla\cdot\boldsymbol{\eta}^{n-1}}{\Delta t_p^n}+\nabla\cdot\mathbf{u}_p^n\right)=(q_p,f_p^n),\quad\forall q_p\in Q_p\,. \tag{10.2.5}$$

We now weakly enforce the transmission conditions over the time intervals with nonconforming time grids. We choose $\mathbf{g}\in P_0(P_\Gamma,\mathbf{G})$ and impose

$$(\boldsymbol{\sigma}_f\mathbf{n}_f)|_\Gamma=\Pi_{f,\Gamma}(\mathbf{g}).$$

The weak conservation of momentum across the interface is fulfilled by setting,

$$(-\boldsymbol{\sigma}_p\mathbf{n}_p)|_\Gamma=\Pi_{p,\Gamma}(\mathbf{g})\in P_0(P_p,\mathbf{G}),$$

and weakly the balance of normal components of the stress in the fluid phase across the interface is fulfilled by setting,

$$p_p|_\Gamma = \Pi_{p,\Gamma}(\mathbf{g}\cdot\mathbf{n}_p) \in P_0(P_p, \mathbf{G}).$$

The semi-discrete (non-conforming in time) counterpart of interface conditions (8.0.10) and (8.0.13) is weakly enforced by integrating it over each time interval T_Γ^i of grid P_Γ:
$\forall i = 1, ..., M_\Gamma$,

$$\int_{T_\Gamma^i} \left(\langle \Pi_{\Gamma,f}(I_{f1}(\Pi_{f,\Gamma}(\mathbf{g}))), \mathbf{v}\cdot\mathbf{t}\rangle_\Gamma + \langle \Pi_{\Gamma,p}(I_{p1}(\Pi_{p,\Gamma}(\mathbf{g}))), \mathbf{v}\cdot\mathbf{t}\rangle_\Gamma \right) ds = 0, \forall\, \mathbf{v} \in \mathbf{G}. \tag{10.2.6}$$

and

$$\int_{T_\Gamma^i} \left(\langle \Pi_{\Gamma,f}(I_{f2}(\Pi_{f,\Gamma}(\mathbf{g}))), \mathbf{v}\cdot\mathbf{n}\rangle_\Gamma + \langle \Pi_{\Gamma,p}(I_{p2}(\Pi_{p,\Gamma}(\mathbf{g}))), \mathbf{v}\cdot\mathbf{n}\rangle_\Gamma \right) ds = 0, \forall\, \mathbf{v} \in \mathbf{G}. \tag{10.2.7}$$

Similarly, for the linearized interface problem, at k^{th} iteration, we have:

$$\int_{J_\Gamma^i} \langle \Psi'_{NC}(\mathbf{g}^k)(\mathbf{h}^k), \mathbf{v}\rangle_\Gamma \, ds = \int_{J_\Gamma^i} \langle -\Psi_{NC}(\mathbf{g}^k), \mathbf{v}\rangle_\Gamma \, ds, \quad \forall\, \mathbf{v} \in \mathbf{G}. \tag{10.2.8}$$

where

$$\Psi_{NC}\left(\mathbf{g}^k\right) = \begin{bmatrix} \Pi_{\Gamma,f}(I_{f1}(\Pi_{f,\Gamma}(\mathbf{g}^k))) + \Pi_{\Gamma,p}(I_{p1}(\Pi_{p,\Gamma}(\mathbf{g}^k))) \\ \Pi_{\Gamma,f}(I_{f2}(\Pi_{f,\Gamma}(\mathbf{g}^k))) + \Pi_{\Gamma,p}(I_{p2}(\Pi_{p,\Gamma}(\mathbf{g}^k))) \end{bmatrix},$$

and

$$\Psi'_{NC}\left(\mathbf{g}^k\right)\left(\mathbf{h}^k\right) = \begin{bmatrix} \Pi_{\Gamma,f}(L_{f1,\mathbf{g}^k}(\Pi_{f,\Gamma}(\mathbf{h}^k))) + \Pi_{\Gamma,p}(L_{p1,\mathbf{g}^k}(\Pi_{p,\Gamma}(\mathbf{h}^k))) \\ \Pi_{\Gamma,f}(L_{f2,\mathbf{g}^k}(\Pi_{f,\Gamma}(\mathbf{h}^k))) + \Pi_{\Gamma,p}(L_{p2,\mathbf{g}^k}(\Pi_{p,\Gamma}(\mathbf{h}^k))) \end{bmatrix}.$$

In the next section, we investigate the numerical performance of the non-conforming time grids in terms of accuracy and efficiency.

10.3 Numerical results

In this section, we present numerical results that illustrate the behavior of the method. We perform numerical tests for three kinds of problems. First, we use a manufactured solution and observe the convergence with respect to space and time. Secondly, we study a hemodynamic appli-

cation. And at last, we implement our method to a geoscience application and perform sensitivity analysis. The computations are performed on FreeFem++ [59].

10.3.1 Test 1 : Convergence tests against manufactured solutions

We consider a test case with a known exact solution. The computational domain are chosen as $\Omega^p = (0,1)\times(0,1)$ for the poroelastic medium and $\Omega^f = (0,1)\times(1,2)$ for the fluid medium, with the interface $\Gamma = \{(x,y) : 0 < x < 1, y = 1\}$. We use the following manufactured solutions [74, 31]:

$$\begin{aligned}
\mathbf{u}_f^{ex} &= \begin{pmatrix} (y-1)^2 x^3 e^{-t} \\ -\cos(y) e^{1-t} \end{pmatrix}, \\
p_f^{ex} &= (\cos(x) e^y + y^2 - 2y + 1) e^{-t}, \\
\mathbf{u}_p^{ex} &= \begin{pmatrix} -x(\sin(y)e + 2(y-1)) e^{-t} \\ (-\cos(y)e + (y-1)^2) e^{-t} \end{pmatrix}, \\
\boldsymbol{\eta}^{ex} &= \begin{pmatrix} (\sqrt{2}\cos(\sqrt{2}x)\cos(y) e^{-t} \\ \sin(\sqrt{2}x)\sin(y) e^{-t} \end{pmatrix}, \\
p_p^{ex} &= (-\sin(y)e + \cos(x)e^y + y^2 - 2y + 1) e^{-t}.
\end{aligned}$$

Note that the above-mentioned manufactured solutions satisfy the interface conditions (8.0.11), (8.0.12), and the following modified versions of (8.0.10) and (8.0.13):

$$\mathbf{u}_f \cdot \mathbf{n}_f = -\mathbf{u}_p \cdot \mathbf{n}_p \,, \tag{10.3.1a}$$

$$\mathbf{n}_f \cdot \boldsymbol{\sigma}_f \mathbf{t} = -c_{BJS} (\mathbf{u}_f \cdot \mathbf{t}) \,, \tag{10.3.1b}$$

with $c_{BJS} = 1$. These conditions (10.3.1a) and (10.3.1b) are obtained from (8.0.10) and (8.0.13) under the assumption that $\frac{\partial \boldsymbol{\eta}}{\partial t}$ is negligible. Since the manufactured solutions satisfy (10.3.1a) and (10.3.1b), instead of (8.0.10) and (8.0.13), the interface operators need to be modified as follows:

$$I_{p1}(\mathbf{g}) = -c_{BJS} \left(\frac{\partial \boldsymbol{\eta}(\mathbf{g})}{\partial t} - \frac{\partial \boldsymbol{\eta}^{ex}}{\partial t} \right) \cdot \mathbf{t}|_\Gamma$$

$$I_{p2}(\mathbf{g}) = \left(\frac{\partial \boldsymbol{\eta}(\mathbf{g})}{\partial t} + \mathbf{u}_p(\mathbf{g}) - \frac{\partial \boldsymbol{\eta}^{ex}}{\partial t} \right) \cdot \mathbf{n}_p|_\Gamma$$

The model parameters are chosen as follows: $\nu_s = 0.5$, $\rho_f = \rho_s = 1$, $\alpha = \beta = \lambda = s_0 = \kappa = 1, K_f = 1, \nu_{f_\infty} = 0.5, \nu_{f_0} = 1.5, \delta = 0$. For the finite element approximations, we use Taylor-Hood elements $\mathbf{P}_2$ - $\mathbf{P}_1$ on structured meshes for both $(\mathbf{u}_f, p_f)$ and $(\mathbf{u}_p, p_p)$, and $\mathbf{P}_2$ elements for $\boldsymbol{\eta}$. These elements are not stable for the Biot model as $\mathbf{u}_p \in H^{div}(\Omega^p)$, hence we add a stabilization term $\gamma(\nabla \cdot \mathbf{u}_p, \nabla \cdot \mathbf{v}_p)$ to the Darcy equation (8.1.5) with $\gamma = 10$. The initial and boundary conditions are imposed using the manufactured solution. To investigate the convergence of the numerical solution with respect to space, we set final computation time $T = 0.0002$ and $(\Delta t_f, \Delta t_p) = (0.00002, 0.00001)$, and use $h \in \{1/4, 1/8, 1/16, 1/32\}$. We set the tolerance for GMRES at 10^{-6}. At the interface, we chose $\Delta t_\Gamma = \Delta t_p$. The errors and the convergence rates for both linear, $r_f = 2$, and non-linear, $r_f = 1.5$, problems are recorded in table 10.1. The convergence rates of all the functions are close to the theoretical rates of convergence. We also performed convergence tests with respect to different time steps while keeping the mesh size fixed, $h = 1/32$. Let Δt_{coarse} and Δt_{fine} represent the coarse and the fine time step size such that $\Delta t_{\text{fine}} = \Delta t_{\text{coarse}}/2$. Then, we consider the following three cases for the convergence test with respect to time: We use $\Delta t_{\text{coarse}} \in \{0.2, 0.1, 0.05, 0.0025\}$. The

Case	Δt_f	Δt_p
Conforming coarse time grids	Δt_{coarse}	Δt_{coarse}
Nonconforming time grids	Δt_{coarse}	Δt_{fine}
Conforming fine time grids	Δt_{fine}	Δt_{fine}

errors plotted in fig. 10.1 show that the first-order convergence in time is preserved for all three cases. The diagrams are similar to the linear Stokes-Biot problem. Further, the computer running time (in seconds) as plotted in fig. 10.2 shows the computational efficiency of using nonconforming time grids.

h		1/4	1/8	1/16	1/32
Linear Viscosity					
$\mathbf{u}_f$	L^2 error	6.00e-04	7.77e-05[2.95]	9.53e-06[3.02]	1.44e-06[2.73]
	H^1 error	2.20e-02	5.18e-03[2.09]	1.24e-03[2.06]	3.36e-04[1.88]
p_f	L^2 error	3.09e-02	5.54e-03[2.48]	1.28e-03[2.12]	3.17e-04[2.01]
$\mathbf{u}_p$	L^2 error	1.00e-03	2.20e-04[2.19]	3.00e-05[2.87]	5.49e-06[2.45]
	H^{div} error	1.87e-03	3.81e-04[2.30]	8.01e-05[2.25]	1.96e-05[2.03]
p_p	L^2 error	2.31e-02	5.03e-03[2.20]	1.26e-03[2.00]	3.11e-04[2.02]
$\boldsymbol{\eta}$	L^2 error	4.17e-04	4.13e-05[3.34]	4.52e-06[3.19]	6.02e-07[2.91]
	H^1 error	1.22e-02	2.44e-03[2.32]	5.69e-04[2.10]	1.45e-04[1.97]
Nonlinear Viscosity					
$\mathbf{u}_f$	L^2 error	6.01e-04	7.77e-05[2.95]	9.75e-06[3.00]	1.59e-06[2.62]
	H^1 error	2.21e-02	5.19e-03[2.09]	1.26e-03[2.04]	3.51e-04[1.85]
p_f	L^2 error	2.98e-02	5.50e-03[2.44]	1.48e-03[1.89]	8.13e-04[0.86]
$\mathbf{u}_p$	L^2 error	1.00e-03	2.18e-04[2.20]	2.97e-05[2.88]	6.41e-06[2.21]
	H^{div} error	1.84e-03	3.74e-04[2.29]	7.86e-05[2.25]	1.93e-05[2.02]
p_p	L^2 error	2.23e-02	4.87e-03[2.20]	1.22e-03[2.00]	3.00e-04[2.02]
$\boldsymbol{\eta}$	L^2 error	4.17e-04	4.13e-05[3.34]	4.52e-06[3.19]	6.02e-07[2.91]
	H^1 error	1.22e-02	2.44e-03[2.32]	5.69e-04[2.10]	1.45e-04[1.97]

Table 10.1: Errors at $T = 0.0002$ by Taylorhood elements for the Stokes and $(\mathbf{P}_2, P_1, \mathbf{P}_2)$ for Biot problems using $(\Delta t_f, \Delta t_p) = (0.00002, 0.00001)$.

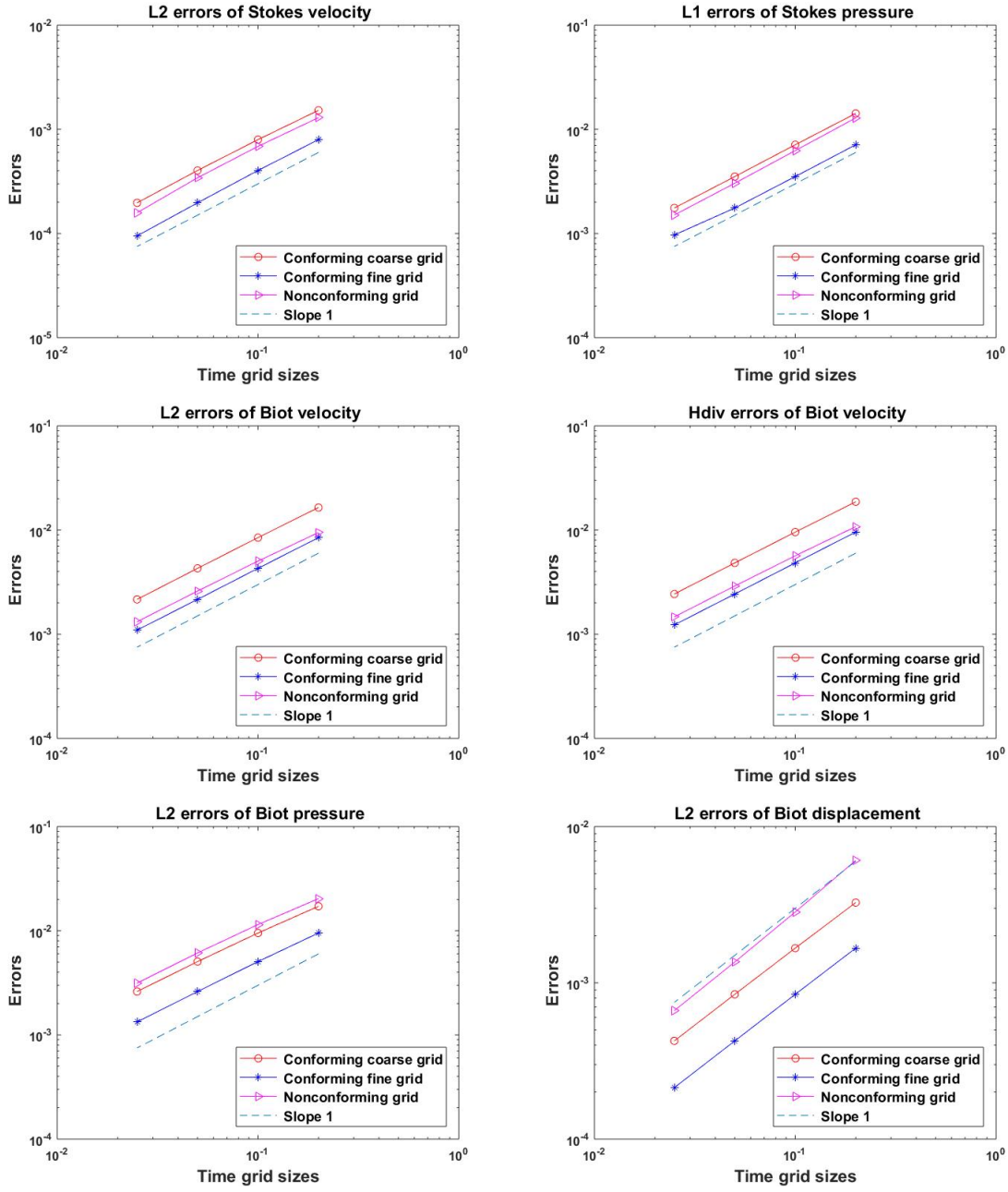

Figure 10.1: Errors at $T = 0.2$ with Taylor-Hood elements for the Stokes and $(\mathbf{P}_2, P_1, \mathbf{P}_2)$ for the nonlinear Biot problem ($r_f = 1.5$).

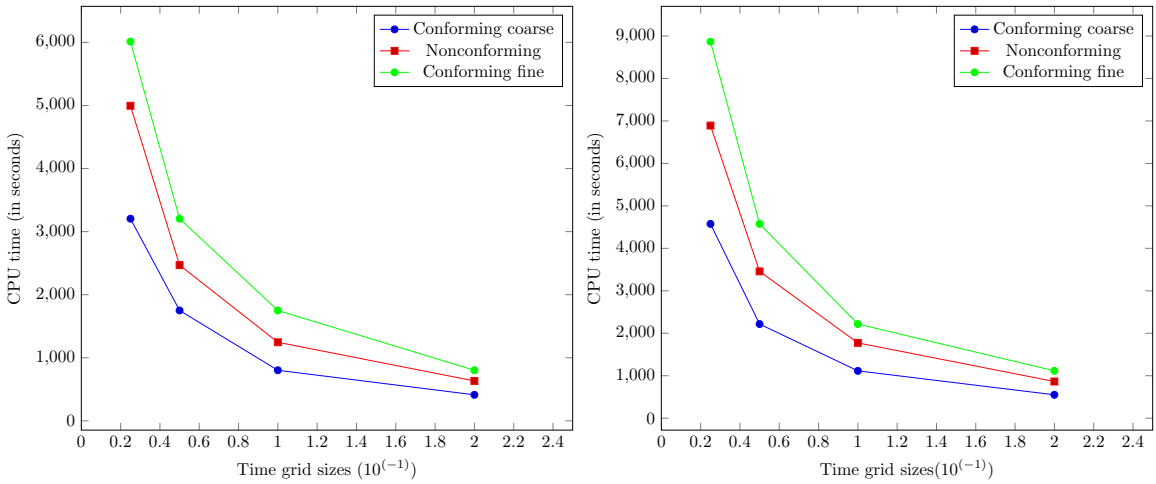

Figure 10.2: Comparison of the computer running times (in seconds) of conforming and nonconforming time grids with Taylorhood elements for the Stokes and $(\mathbf{P}_2, P_1, \mathbf{P}_2)$ for linear (left) and nonlinear (right) Biot problems on fixed mesh $h = 1/32$.

10.3.2 Test 2 : Application in Haemodynamic experiment

The example focuses on a well-established benchmark problem in FSI, as cited in [19, 9] and related literature. In this example, we examine the propagation of a pressure wave whose magnitude is similar to the pressure difference between the systolic and diastolic phases of a heartbeat. Figure 10.3 depicts the domain and boundary conditions used for the computation. The force $\mathbf{b}(t)$ applied to the left fluid boundary in Figure 10.3 denotes the stress at the inlet at t seconds and is defined as:

$$\mathbf{b}(t) = \begin{cases} \left(\frac{P_{max}}{2} \left(1 - \cos \frac{2\pi t}{T_{max}} \right), 0 \right) & t \leq T_{max} \\ (0,0) & T_{max} < t < T_{final}, \end{cases}$$

where $P_{max} = 2 \times 10^3 \text{dyne/cm}^2$ and $T_{max} = 0.003$ seconds. In order to better emulate an artery's behavior, the governing equation (8.0.5) for the elastic skeleton is adjusted slightly as follows for this test case:

$$\rho_s \frac{\partial^2 \boldsymbol{\eta}}{\partial t^2} - 2\nu_s \nabla \cdot D(\boldsymbol{\eta}) - \lambda \nabla(\nabla \cdot \boldsymbol{\eta}) + \xi \boldsymbol{\eta} + \alpha \nabla p_p \quad = \quad \mathbf{f}_s \quad \text{in } \Omega^p \times (0,T)\,, \tag{10.3.2}$$

As per the axially symmetric formulation, the term $\xi\boldsymbol{\eta}$ is necessary to compensate for the recoil induced by the circumferential strain [18]. The parameters used in this example are in accordance

with the characteristics of blood flow in the human body. The density of the fluid, ρ_f, is 1 g/cm^3 and the viscosity of the fluid, ν_f, is 0.035 g/cm·s. The density of the structure, ρ_s, is 1.1 g/cm^3. The Young's Modulus of the structure, E, is 3×10^6 dyne/cm^2 and the Poisson ratio, ν, is 0.4. The Lame parameters λ and ν_s are defined as follows:

$$\lambda = \frac{\nu E}{(1-2\nu)(1+\nu)} \text{ dyne/cm}^2, \quad \nu_s = \frac{E}{2(1+\nu)} \text{dyne/cm}^2.$$

The hydraulic conductivity, κ, is 5×10^{-9} cm^{3}s/g and the mass storage coefficient, s_0, is 0 cm^2/dyne. The Biot-Willis constant, α, is set to unity, and the spring constant, ξ, is 5×10^7dyne/cm^4. Please take note that though $\alpha = 1$ and $s_0 = 0$ signify that both the fluid and solid components are incompressible, a Poisson ratio that is less than 0.5 suggests that the poroelastic medium is still compressible [96]. Both the fluid and structure have volume forces of $\mathbf{f}_s = \mathbf{f}_f = \mathbf{0}$ dyne/cm^2. We simulate this example for the final time $T_{final} = 6$ ms and $h = 0.05$ cm using a time step of $\Delta t_f = 5 \times 10^{-4}$ seconds for the fluid subdomain and $\Delta t_s = 2.5 \times 10^{-4}$ seconds for the structure subdomain. At the interface, we set $\Delta t_\Gamma = \Delta t_f$. For this test, we use MINI elements for the Stokes and $(RT1, P_1, \mathbf{P}_b)$ for the Biot subproblem. In figure 10.4, we record the fluid pressure, p_f, and the pressure of the poroelastic structure, p_p, at every 2 ms. The simulation illustrated in the figure depicts the visual representation of the initial pressure pulse propagation from left to right in a fluid and the poroelastic domain. Further figure 10.5 shows the vertical displacement of the interface as the pressure pulse propagates. This is crucial for understanding how the pressure pulse affects the physical structure of the system under investigation. The results obtained from this simulation are qualitatively similar to those obtained in a prior study [19] using conforming time-step $\Delta t = 10^{-6}$ seconds.

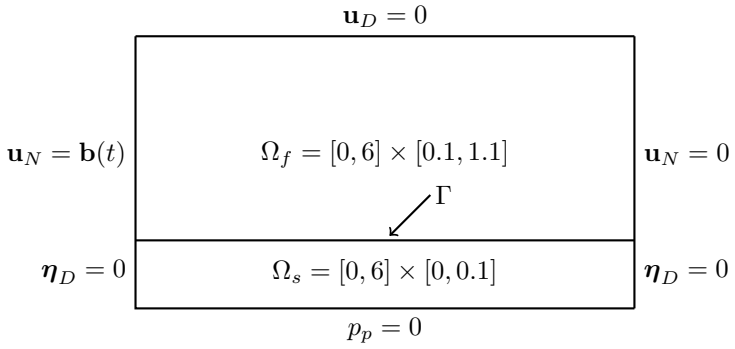

Figure 10.3: Domain and boundary conditions for Test2

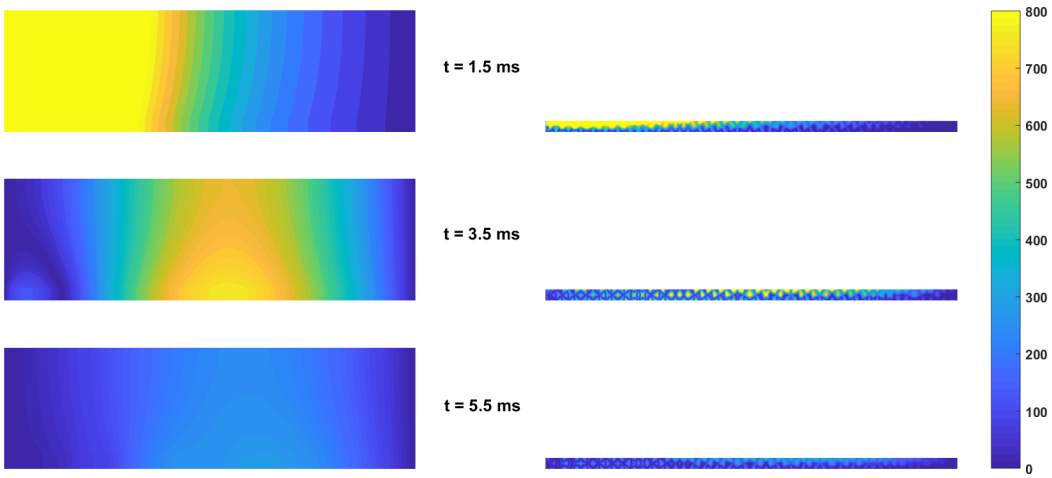

Figure 10.4: Pressure profiles at every 2 ms to visualize the propagation of an initial pressure pulse in a fluid (left) and poroelastic structure (right).

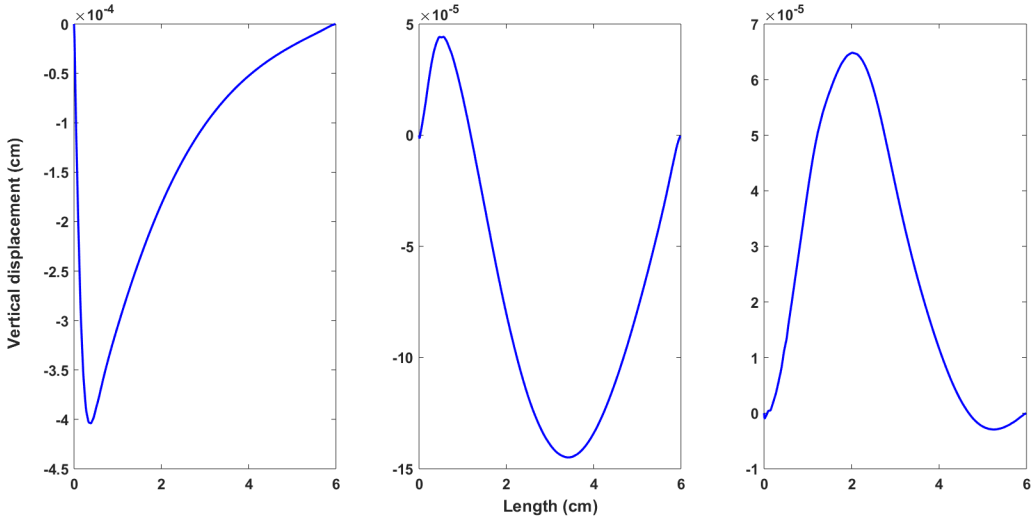

Figure 10.5: Vertical displacement of the fluid-structure interface at times 1.5 ms, 3.5 ms, and 4.5 ms from left to right.

10.3.3 Test 3 : Geoscience application

In this particular case, we conduct a simulation that involves the coupling of surface and subsurface flows [28]. This modeling type finds valuable geoscience applications, as it allows us to

describe important interactions, like those occurring between a river and an aquifer. We consider the fluid domain $\Omega_f = (0,2)\times(0,1)$ and poroelastic domain $\Omega_f = (0,2)\times(-1,0)$, with the interface $\Gamma = \{(x,y) : 0 < x < 2, y = 0\}$. For geoscience application, the governing equation (8.0.5) for the poroelastic structure is adjusted as follows for this test case:

$$-2\nu_s \nabla\cdot D(\boldsymbol{\eta}) - \lambda\nabla(\nabla\cdot\boldsymbol{\eta}) + \alpha\nabla p_p \quad = \quad \mathbf{f}_s \quad \text{in } \Omega^p\times(0,T)\,, \tag{10.3.3}$$

The following physical parameters are set to unity: $\rho_f = \nu_f = \alpha = 1$. Both the fluid and structure have volume forces of $\mathbf{f}_s = \mathbf{f}_f = \mathbf{0}$. The flow is driven through a parabolic fluid velocity on the left boundary of the fluid region with boundary conditions as specified in figure 10.6.

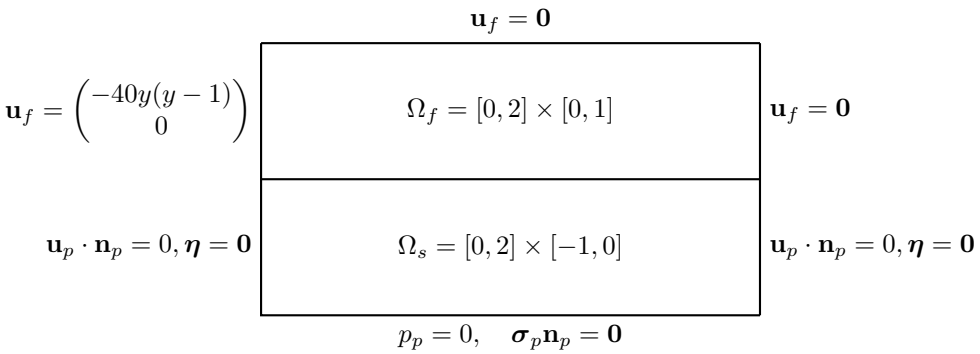

Figure 10.6: Domain and boundary conditions for Test3

We simulate this example for the final time $T_{\text{final}} = 3$ s using a time step of $\Delta t_f = 1.5\times10^{-1}$ seconds for the fluid subdomain and $\Delta t_s = 3.0\times10^{-1}$ seconds for the structure subdomain. At the interface, we set $\Delta t_\Gamma = \Delta t_s$. For the mesh discretization we set $h = 0.05$. For this test, the fluid and structure are approximated using MINI elements and $(RT1, P_1, \mathbf{P}_b)$ elements, respectively. We consider three cases with different values of κ, s_0, λ and ν_s, as described in table 10.2. We plot the velocities $\mathbf{u}_f$ and $\mathbf{u}_p + \partial_t\boldsymbol{\eta}$ (arrows) and their normal components (color) in their respective domains on the left and displacement profile in poroelastic structure on the right for each case in fig. 10.7. In case I, We note that the absence of pressure at the bottom induces the flow of fluid into the poroelastic medium, effectively emulating the influence of gravity. Further, the color plot shows the continuity of the second components of velocities at the interface. In case II, we test the model for a problem where poroelastic material has small permeability and storativity. We notice that the behavior is qualitatively similar to Case I, except the fluid flows in the poroelastic structure in

smaller amount. In case III, we increase the lame constant ν_s from unity to 10^6, representing a stiff poroelastic structure and notice that almost no fluid flows in the structure and the displacement is also very small. Furthermore, we report the interface velocity errors, $\|\mathbf{u}_f \cdot \mathbf{n}_f + \left(\frac{\partial \boldsymbol{\eta}}{\partial t} + \mathbf{u}_p\right) \cdot \mathbf{n}_p\|_\Gamma^2$ (Error 1) and $\| \sum_{j=1}^{d-1} \boldsymbol{\sigma}_f \mathbf{n}_f \cdot \mathbf{t}_j + c_{BJS} \left(\mathbf{u}_f - \frac{\partial \boldsymbol{\eta}}{\partial t}\right) \cdot \mathbf{t}_j\|_\Gamma^2$ (Error 2) for different time sizes in Table 4.7 at the final time $T = 3$ seconds. Since we set $\Delta t_\Gamma = \Delta t_p$, selecting larger time intervals for the poroelastic structure reduces the dimension of the interface problem. This offers the benefit of needing fewer GMRES iterations, thus reducing computational time, all the while preserving accuracy. We also considered a case with nonlinear fluid viscosity, ($r_f = 1.5$), and observed similar plots at final time $T_{final} = 3$ seconds using larger time steps (see Figure 10.8). The interface velocity errors are reported in Table 10.3.

Case	κ	s_0	λ	ν_s
I	1	1	1	1
II	10^{-4}	10^{-4}	10^6	1
III	10^{-4}	10^{-4}	10^6	10^6

Table 10.2: Physical parameters for the sensitivity analysis.

Accumulated Interface velocity errors						
$(\Delta t_f, \Delta t_p)$	Case I		Case II		Case III	
	Error 1	Error 2	Error 1	Error 2	Error 1	Error 2
(0.075, 0.075)	1.49e-05	1.90e-06	9.00e-04	2.00e-03	3.89e-05	1.08e-00
(0.075, 0.15)	4.08e-11	9.28e-12	1.88e-07	3.57e-06	9.84e-19	4.12e-13
(0.075, 0.30)	3.85e-11	8.92e-12	2.86e-11	2.33e-10	5.10e-20	3.28e-15

Table 10.3: Comparison of the accumulated interface velocity errors in case I, II and III for $r_f = 1.5$.

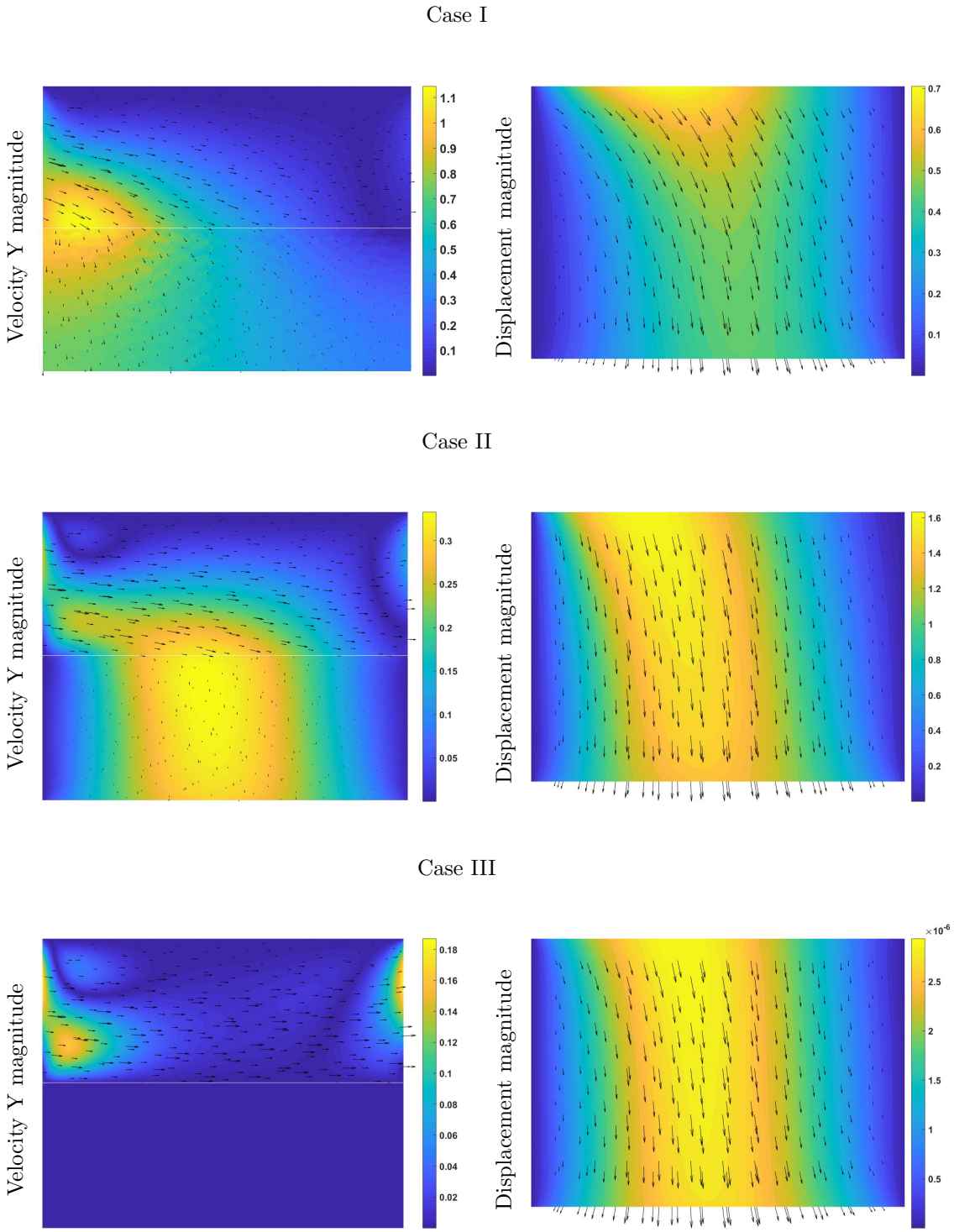

Figure 10.7: Velocities $\mathbf{u}_f$ and $\mathbf{u}_p + \partial_t \boldsymbol{\eta}$ (arrows) and their normal components (color) in their respective domains (left) and displacement profile in poroelastic structure (right) in case I, II and III respectively for $r_f = 2$.

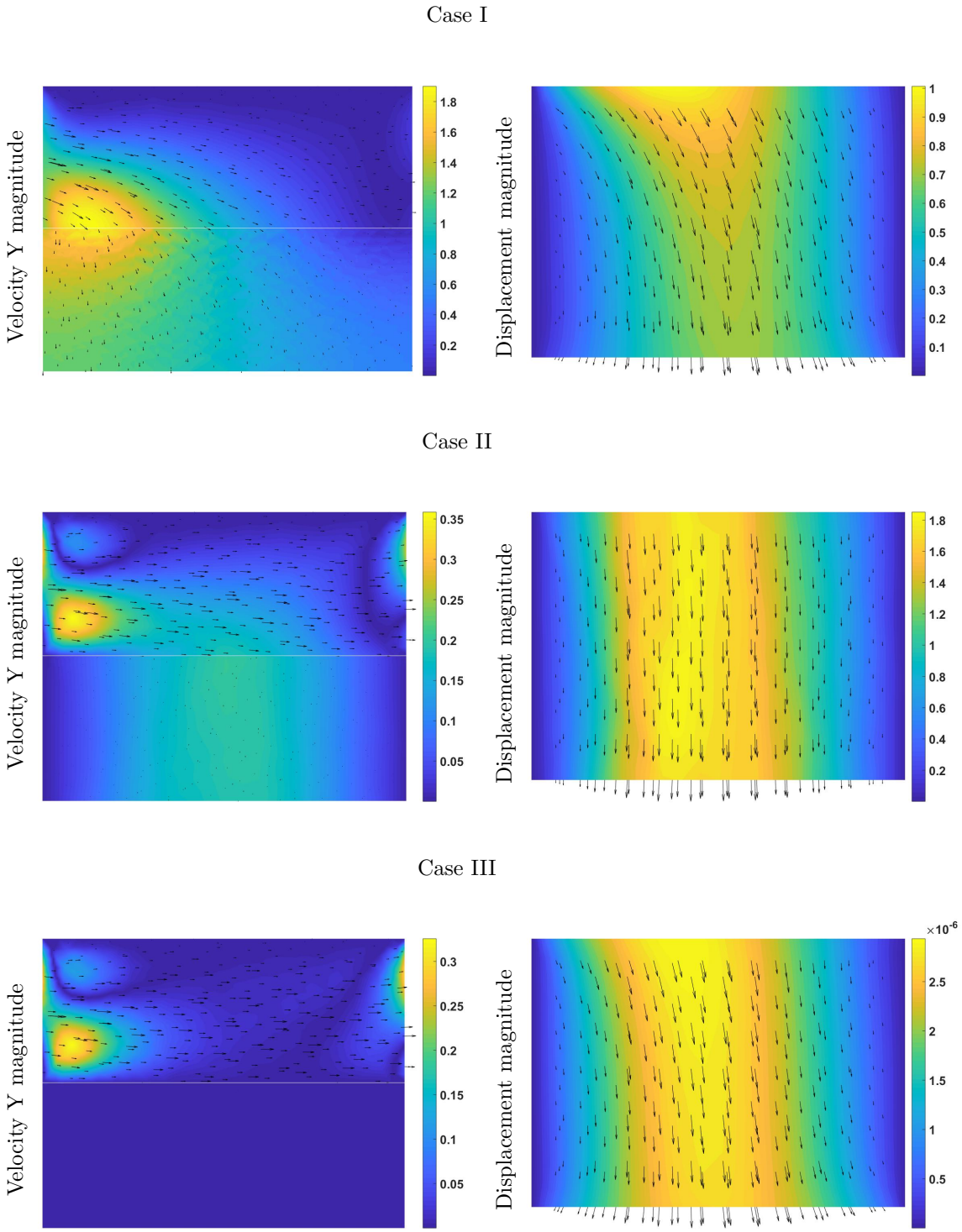

Figure 10.8: Velocities $\mathbf{u}_f$ and $\mathbf{u}_p + \partial_t \boldsymbol{\eta}$ (arrows) and their normal components (color) in their respective domains (left) and displacement profile in poroelastic structure (right) in case I, II and III respectively for $r_f = 1.5$.

Part IV

3D Fluid/2D Plate interaction system

Chapter 11

Model equations

We consider a domain $\Omega_p = \{x = (x_1, x_2, 0)\}$, and surface $S = \{x = (x_1, x_2, x_3) : x_3 \leq 0\}$ and $\Omega_f \in \mathbb{R}^3$ such that the boundary of Ω_f is $\partial\Omega_f := \overline{\Omega_p} \cup \overline{S}$. We consider the flow in Ω_f to be governed by the time-dependent Stokes equation and the plate structure is modeled by the "Euler-Bernoulli" or "Kirchhoff" equation. The fluid-plate system [5] is then written as, for $T > 0$:

$$\begin{aligned}
\mathbf{u}_t - \nu_f \Delta \mathbf{u} + \nabla p = \mathbf{f}_f \quad &\text{in } \Omega_f \times (0,T)\,, \\
\nabla \cdot \ \mathbf{u} = 0 \quad &\text{in } \Omega_f \times (0,T)\,, \\
\mathbf{u} = \mathbf{0} \quad &\text{on } S \\
w_{tt} - \rho \Delta w_{tt} + \Delta^2 w = p|_{\Omega_p} \quad &\text{in } \Omega_p \times (0,T)\,, \\
w = \frac{\partial w}{\partial \nu} = 0 \quad &\text{on } \partial\Omega_p\,, \\
\mathbf{u} = [u_1, u_2, u_3] = [0, 0, w_t] \quad &\text{on } \Omega_p \times (0,T).
\end{aligned} \tag{11.0.1}$$

where $\mathbf{u}(\mathbf{x}, t)$ and $p(\mathbf{x}, t)$ denote the fluid velocity and the fluid pressure respectively in Ω_f. And $\nu_f, \mathbf{f}_f(\mathbf{x}, t)$ denote the constant fluid viscosity, and the body force, respectively. Furthermore, $w(\mathbf{x}, t)$ is the displacement of the plate structure. The constant $\rho \geq 0$ indicates the rotational inertia parameter. Whenever $\rho = 0$, the dynamics of the plate is considered "Euler-Bernoulli" type, while for $\rho > 0$ the dynamics is considered "Kirchhoff" type. The model equations (11.0.1) are accompanied by the initial conditions $w = w_0,\ w_t = w_{t0},\ \mathbf{u} = \mathbf{u}_0 \quad \text{at } t = 0.$

Chapter 12

Weak formulation and stability analysis

Now, we derive a weak formulation of the problem using a Lagrange multiplier. We use the standard notation for Sobolev spaces and their associated norms and seminorms. We denote L^2 inner product and norm over Θ by $(\cdot,\cdot)_\Theta$ and $\|\cdot\|_\Theta$, respectively. For functions defined in Ω_f and Ω_p, we simply use $(\cdot,\cdot) = (\cdot,\cdot)_{\Omega^f}$ or $(\cdot,\cdot)_{\Omega_p}$. Define

$$\mathbf{U} := \{\mathbf{v} = (v_1, v_2, v_3) \in \mathbf{H}^1(\Omega_f) : \ v_1 = v_2 = 0 \text{ on } \Omega_p, \mathbf{v} = \mathbf{0} \text{ on } S\}, \qquad Q := L^2(\Omega_f),$$
$$W := \{z \in H^2(\Omega_p) : z = \frac{\partial z}{\partial \nu} = 0 \text{ on } \partial\Omega_p\}.$$

We also define the *div-free* space for the fluid velocity,

$$\mathbf{V} := \{\mathbf{v} \in \mathbf{U} : (q, \nabla \cdot \mathbf{v}) = 0, \forall q \in Q\}.$$

The spaces $\mathbf{V}$ and Q satisfy the inf-sup condition,

$$\inf_{q\in Q} \sup_{\mathbf{v}\in\mathbf{V}} \frac{(q, \nabla \cdot \mathbf{v})}{\|q\|\|\nabla \mathbf{v}\|} \geq \beta > 0. \tag{12.0.1}$$

The dual spaces $\mathbf{U}^*$ and $\mathbf{V}^*$ are endowed with the following dual norms

$$\|\mathbf{w}\|_{\mathbf{U}^*} := \sup_{\mathbf{v}\in\mathbf{U}} \frac{(\mathbf{w},\mathbf{v})}{\|\nabla\mathbf{v}\|}, \quad \|\mathbf{w}\|_{\mathbf{V}^*} := \sup_{v\in\mathbf{V}} \frac{(\mathbf{w},\mathbf{v})}{\|\nabla\mathbf{v}\|}\,.$$

These norms are equivalent for functions in $\mathbf{V}$ as stated in the following lemma.

Lemma 12.0.1. *Let $\mathbf{w} \in \mathbf{V}$. Then, there exists $C_* > 0$, such that*

$$C_*\|\mathbf{w}\|_{\mathbf{U}^*} \le \|\mathbf{w}\|_{\mathbf{V}^*} \le \|\mathbf{w}\|_{\mathbf{U}^*}.$$

Proof. See Lemma 1 in [53]. □

For the variational formulation, we introduce a Lagrange multiplier $g \in G := H^{-1/2}(\Omega_p)$, representing

$$g := (\boldsymbol{\sigma}_f \mathbf{n}_f)_3 \quad \text{on } \Omega_p \times (0,T), \tag{12.0.2}$$

where $\boldsymbol{\sigma}_f = \nu_f \nabla\mathbf{u} - p\mathbf{I}$ and $\mathbf{n}_f = [0\ 0\ 1]^T$. We now multiply the governing equations by appropriate test functions and use integration by parts to obtain the following continuous variational formulation: *given initial conditions, find $(\mathbf{u}, p, w, g) \in (\mathbf{U}, Q, W, G)$, for a.e. $t \in (0,T)$, such that*

$$\begin{aligned}
(\mathbf{u}_t,\, \mathbf{v}) + (\nu_f\nabla\mathbf{u}, \nabla\mathbf{v}) - (p, \nabla\cdot\mathbf{v}) &= (\mathbf{f}_f, \mathbf{v}) + \langle g, v_3\rangle_{\Omega_p} \quad \forall\mathbf{v}\in\mathbf{U}\,, && (12.0.3)\\
(q, \nabla\cdot\mathbf{u}) &= 0, \quad \forall q \in Q\,. && (12.0.4)
\end{aligned}$$

and

$$\begin{aligned}
(w_{tt},\, z) + \rho(\nabla w_{tt}, \nabla z) + (\Delta w, \Delta z) &= (p|_{\Omega_p}, z) \quad \forall z \in W\,, && (12.0.5)\\
(u_3 - w_t, \lambda) &= 0, \quad \forall\lambda \in G\,. && (12.0.6)
\end{aligned}$$

Note that (12.0.6) weakly enforces continuity of velocity at the plate structure. The existence of a solution to (11.0.1) with additional damping term Δw_t in the plate equation is established in [29] under a small data condition. The wellposedness of the 3D fluid-plate model used in [35] is established by the means of constructing for it a nonstandard semigroup generator representation in [5]. Here, we assume the well-posed nature of the variational formulation (12.0.3)-(12.0.6), and concentrate on the decoupled methodology and the numerical algorithm. In the following theorem,

we show the stability of the solution of (12.0.3)-(12.0.6).

Theorem 12.0.2. *For any $\mathbf{f}_f \in L^2(0,T,\mathbf{L}^2(\Omega_f))$ the solution to* (12.0.3)-(12.0.6)*, $(\mathbf{u}, w)$, is stable. For any $t > 0$ and $C_{PF} > 0$,*

$$\|\mathbf{u}\|^2_{\Omega_f} + \nu_f \int_0^t \|\nabla \mathbf{u}\|^2_{\Omega_f} dt + \|w_t\|^2_{\Omega_s} + \rho\|\nabla w_t\|^2_{\Omega_s} + \|\Delta w\|^2_{\Omega_s} \leq \frac{C_{PF}}{\nu_f} \int_0^t \|\mathbf{f}_f\|^2_{\Omega_f} dt + C_0, \quad (12.0.7)$$

where $C_0 = \|\mathbf{u}_0\|^2_{\Omega_f} + \|w_{t0}\|^2_{\Omega_s} + \rho\|\nabla w_{t0}\|^2_{\Omega_s} + \|\Delta w_0\|^2_{\Omega_s}$. Further, we have, for some $C_\beta > 0$,

$$\int_0^t \|p\|^2_{\Omega_f} dt \leq C_\beta \left(\int_0^t \|\mathbf{f}_f\|^2_{\Omega_f} dt + \int_0^t \|g\|^2_{\Omega_p} dt + C_0 \right).$$

Proof. Note that in Ω_p, $g = \nu_f \partial_z u_3 - p$. So using, $\nabla \mathbf{u} = 0$ on Ω_f and $\mathbf{u} = [u_1, u_2, u_3] = [0, 0, w_t]$ on Ω_p, we have $\partial_z u_3 = 0$, hence $g = -p$ [35]. Now choosing $\mathbf{v} = \mathbf{u}$ in (12.0.3), $q = p$ in (12.0.4), $z = w_t$ in (12.0.5) and $\lambda = g$ in (12.0.6), and adding together we get:

$$(\mathbf{u}_t, \mathbf{u}) + \nu_f \|\nabla \mathbf{u}\|_{\Omega_f} + (w_{tt}, w_t) + \rho(\nabla w_{tt}, \nabla w_t) + (\Delta w, \Delta w_t) = (\mathbf{f}_f, \mathbf{u})$$

Now using Cauchy-Schwarz inequality and multiplying both sides by 2, we get,

$$\frac{d}{dt}\|\mathbf{u}\|^2_{\Omega_f} + 2\nu_f \|\nabla \mathbf{u}\|^2_{\Omega_f} + \frac{d}{dt}\|w_t\|^2_{\Omega_s} + \rho\frac{d}{dt}\|\nabla w_t\|^2_{\Omega_s} + \frac{d}{dt}\|\Delta w\|^2_{\Omega_s} \leq 2\|\mathbf{f}_f\|_{\Omega_f}\|\mathbf{u}\|_{\Omega_f}$$

On integrating over (0,t) for a.e. $t \in (0,T)$, we get,

$$\begin{aligned} &\|\mathbf{u}\|^2_{\Omega_f} + 2\nu_f \int_0^t \|\nabla \mathbf{u}\|^2_{\Omega_f} dt + \|w_t\|^2_{\Omega_s} + \rho\|\nabla w_t\|^2_{\Omega_s} + \|\Delta w\|^2_{\Omega_s} \\ &\leq 2\int_0^t \|\mathbf{f}_f\|_{\Omega_f}\|\mathbf{u}\|_{\Omega_f} dt + \|\mathbf{u}_0\|^2_{\Omega_f} + \|w_{t0}\|^2_{\Omega_s} + \rho\|\nabla w_{t0}\|^2_{\Omega_s} + \|\Delta w_0\|^2_{\Omega_s} \end{aligned}$$

Now, using Young's inequality and Poincare-Friedrich's inequality, we get, for some $\epsilon > 0$ and $C_{PF} > 0$,

$$\begin{aligned} &\|\mathbf{u}\|^2_{\Omega_f} + 2\nu_f \int_0^t \|\nabla \mathbf{u}\|^2_{\Omega_f} dt + \|w_t\|^2_{\Omega_s} + \rho\|\nabla w_t\|^2_{\Omega_s} + \|\Delta w\|^2_{\Omega_s} \\ &\leq \frac{1}{\epsilon}\int_0^t \|\mathbf{f}_f\|^2_{\Omega_f} dt + \epsilon C_{PF} \int_0^t \|\nabla \mathbf{u}\|_{\Omega_f} dt + \|\mathbf{u}_0\|^2_{\Omega_f} + \|w_{t0}\|^2_{\Omega_s} + \rho\|\nabla w_{t0}\|^2_{\Omega_s} + \|\Delta w_0\|^2_{\Omega_s} \end{aligned}$$

Now setting $\epsilon = (\nu_f / C_{PF})$, we get (12.0.7). To estimate the bound of p, first, we estimate a bound for the time derivative term in (12.0.3). For $\mathbf{v} \in \mathbf{V}$ the equation (12.0.3) is written as

$$(\mathbf{u}_t, \mathbf{v}) \quad = \quad -\nu_f(\nabla \mathbf{u}, \nabla \mathbf{v}) + (\mathbf{f}_f, \mathbf{v}) + (g, v_3)_{\Omega_p} \,. \tag{12.0.8}$$

The last term on the right-hand side of (12.0.8) is bounded as

$$(g, v_3)_{\Omega_p} \leq \|g\|_{H^{-1/2}(\Omega_p)} \|\mathbf{v}\|_{H^{1/2}(\Omega_p)} \leq C \|g\|_{H^{-1/2}(\Omega_p)} \|\mathbf{v}\|_{H^1(\Omega_f)},$$

using the trace theorem. Now, using Cauchy-Schwarz inequality and Poincaré-Friedrichs inequality in (3.3.21), we have, for some constant $\widehat{C} > 0$,

$$\|\mathbf{u}_t\|_{\mathbf{V}^*} \leq \widehat{C}(\|\nabla \mathbf{u}\|_{\Omega_f} + \|\mathbf{f}_f\|_{\Omega_f} + \|g\|_{H^{-1/2}(\Omega_p)}).$$

The norm equivalence of $\|\cdot\|_{\mathbf{U}^*}$ and $\|\cdot\|_{\mathbf{V}^*}$ (see Lemma 1 in [53]) then implies, for some constant $C_* > 0$,

$$\|\mathbf{u}_t\|_{\mathbf{U}^*} \leq C_*(\|\nabla \mathbf{u}\|_{\Omega_f} + \|\mathbf{f}_f\|_{\Omega_f} + \|g\|_{H^{-1/2}(\Omega_p)}) \,. \tag{12.0.9}$$

To estimate a bound for the pressure term p, consider (3.3.8) with $\mathbf{v} \in \mathbf{U}$. We isolate the pressure term, divide by $\|\nabla \mathbf{v}\|_{\Omega_f}$, take supremum over $\mathbf{v} \in \mathbf{U}$. Then the inf-sup condition (2.1.1) and the estimate (12.0.9) yield

$$\beta \|p\|_{\Omega_f} \;\leq\; (1 + C_*)(\|\nabla \mathbf{u}\|_{\Omega_f} + \|\mathbf{f}_f\|_{\Omega_f} + \|g\|_{H^{-1/2}(\Omega_p)}) \,.$$

for some $\beta > 0$. Finally, we square both sides, integrate over $(0, t)$, use (12.0.7), to obtain

$$\int_0^t \|p\|^2_{\Omega_f} ds \;\leq\; C_\beta \left(\int_0^t \|\mathbf{f}_f\|^2_{\Omega_f} ds + \int_0^t \|g\|^2_{H^{-1/2}(\Omega_p)} ds + C_0 \right)$$

or some constant $C_\beta > 0$. □

Chapter 13

Second-order temporal discretization scheme

In this section, we discuss the second-order temporal discretization scheme for the fluid-plate system and study its stability. To discretize the above equations in time, we set for $T > 0$, let $\Delta t = T/M$, where M is a positive integer and for $n = 0, 1, 2, \cdots, M$, let $t_n = n\Delta t$. For any sufficiently smooth function $v(\mathbf{x}, t)$, both constant and vector-valued, we define $v^n(\mathbf{x}) \sim v(\mathbf{x}, t_n)$. The fluid equations are discretized in time using a second-order Crank-Nicolson scheme while the plate equations are discretized using a second-order Newmark scheme [74]. Further, we introduce an additional variable $\dot{w} \in W$, representing w_t in the plate subsystem. As a notation, we define for any function $\phi, \overline{\phi^n} = \dfrac{\phi^n + \phi^{n-1}}{2}$. The fluid-plate system [5] is then written as, for final time $T > 0$:

$$\rho_f(\mathbf{u}^n - \mathbf{u}^{n-1}) - \nu_f \Delta t \Delta \overline{\mathbf{u}^n} + \Delta t \nabla \overline{p^n} = \Delta t \overline{\mathbf{f}_f^n} \quad \text{in } \Omega_f\,, \tag{13.0.1}$$

$$\nabla \cdot \overline{\mathbf{u}^n} = 0 \quad \text{in } \Omega_f\,, \tag{13.0.2}$$

$$(\dot{w}^n - \dot{w}^{n-1}) - \rho\Delta(\dot{w}^n - \dot{w}^{n-1}) + \Delta t \Delta^2 \overline{w^n} = \Delta t \overline{p^n}|_{\Omega_p} \quad \text{in } \Omega_p\,, \tag{13.0.3}$$

$$w^n - w^{n-1} = \Delta t \overline{\dot{w}^n} \quad \text{in } \Omega_p\,, \tag{13.0.4}$$

$$\overline{u_3^n} = \overline{\dot{w}^n} \quad \text{in } \Omega_p. \tag{13.0.5}$$

In the next theorem, we show the stability of the numerical scheme.

Theorem 13.0.1. *The method* (13.0.1)-(13.0.5) *is unconditionally stable. Moreover, for some constants $C_M, C_T > 0$, and for any t_n, the following relations hold:*

$$\rho_f\|\mathbf{u}^M\|^2_{\Omega_f} + 2\nu_f\tau\sum_{n=0}^{M}\|\nabla\overline{\mathbf{u}}^n\|^2_{\Omega_f} + \|\dot{w}^M\|^2_{\Omega_p} + \|\Delta w^M\|^2_{\Omega_p} + \rho\|\nabla\dot{w}^M\|^2_{\Omega_p} \leq \frac{\tau C_M}{\nu_f}\sum_{n=0}^{M}\|\overline{\mathbf{f}_f}^n\|^2_{\Omega_f}, \tag{13.0.6}$$

$$\|w^n\|^2_{\Omega_p} \leq \frac{(C_T\tau)^2 C_M}{4\nu_f}\sum_{n=0}^{M}\|\overline{\mathbf{f}_f}^n\|^2_{\Omega_f} \tag{13.0.7}$$

Additionally, we have

$$\|\overline{p}^n\|^2_{\Omega_f} \leq C_\beta(\,\|\overline{\mathbf{f}_f}^n\|^2_{\Omega_f} + \|\overline{g}^n\|^2_{H^{-1/2}(\Omega_p)}\,) \tag{13.0.8}$$

for some $C_\beta > 0$.

Proof. For simplicity, let $\mathbf{u}_0 = \mathbf{0}$ and $w_0 = w_{t0} = 0$. Multiplying (13.0.1) and (13.0.2) by $\overline{\mathbf{u}}^n$ and $\overline{p}^n$ respectively, integrating over Ω_p, and adding the results yield

$$\frac{\rho_f}{2}\left(\|\mathbf{u}^n\|^2_{\Omega_f} - \|\mathbf{u}^{n-1}\|^2_{\Omega_f}\right) + \nu_f\tau\|\nabla\overline{\mathbf{u}}^n\|^2_{\Omega_f} \leq \tau(\overline{\mathbf{f}}^n_f, \overline{\mathbf{u}}^n)_{\Omega_f} + \tau(\overline{g}^n, \overline{u_3^n})_{\Omega_p}. \tag{13.0.9}$$

Similarly, we multiply (13.0.3) by $\overline{\dot{w}}^n$, integrate over Ω_p, and use Green's theorem and (13.0.4) to get,

$$\begin{aligned}\frac{1}{2}\left(\|\dot{w}^n\|^2_{\Omega_p} - \|\dot{w}^{n-1}\|^2_{\Omega_p}\right) + \frac{\rho}{2}\left(\|\nabla\dot{w}^n\|^2_{\Omega_p} - \|\nabla\dot{w}^{n-1}\|^2_{\Omega_p}\right)\\ +\frac{1}{2}\left(\|\Delta w^n\|^2_{\Omega_p} - \|\Delta w^{n-1}\|^2_{\Omega_p}\right) = \tau(\overline{p}^n, \overline{\dot{w}}^n)\end{aligned} \tag{13.0.10}$$

Also, multiplying (13.0.5) by $\overline{g}^n$ and integrating over Ω_p, we have

$$(\overline{u}^n_3, \overline{g}^n)_{\Omega_p} = (\overline{\dot{w}}^n, \overline{g}^n)_{\Omega_p}. \tag{13.0.11}$$

Now, use $\overline{p}^n = -\overline{g}^n$ in (13.0.10), add (13.0.9) to (13.0.10), and use (13.0.11) and Cauchy-Schwarz inequality. Then, for any $\epsilon > 0$ and for some $C_{PF} > 0$,

$$\begin{aligned}&\frac{\rho_f}{2}\left(\|\mathbf{u}^n\|^2_{\Omega_f} - \|\mathbf{u}^{n-1}\|^2_{\Omega_f}\right) + \nu_f\tau\|\nabla\overline{\mathbf{u}}^n\|^2_{\Omega_f} + \frac{1}{2}\left(\|\dot{w}^n\|^2_{\Omega_p} - \|\dot{w}^{n-1}\|^2_{\Omega_p}\right)\\ &+\frac{1}{2}\left(\|\Delta w^n\|^2_{\Omega_p} - \|\Delta w^{n-1}\|^2_{\Omega_p}\right) + \frac{\rho}{2}\left(\|\nabla\dot{w}^n\|^2_{\Omega_p} - \|\nabla\dot{w}^{n-1}\|^2_{\Omega_p}\right)\\ &\leq \tau\|\overline{\mathbf{f}}^n_f\|_{\Omega_f}\|\overline{\mathbf{u}}^n\|_{\Omega_f} \leq \frac{\tau}{2\epsilon}\|\overline{\mathbf{f}}^n_f\|^2_{\Omega_f} + \frac{\epsilon C_{PF}\tau}{2}\|\nabla\overline{\mathbf{u}}^n\|^2_{\Omega_f}\end{aligned}$$

using Young's inequality and Poincare-Friedrich's inequality. Setting $\epsilon = \nu_f/(C_{PF})$ and summing from $n = 0$ to M, we get, for some constant $C_M > 0$

$$\rho_f \|\mathbf{u}^M\|^2_{\Omega_f} + \nu_f \tau \sum_{n=0}^{M} \|\nabla \overline{\mathbf{u}}^n\|^2_{\Omega_f} + \|\dot{w}^M\|^2_{\Omega_p} + \|\Delta w^M\|^2_{\Omega_p} + \rho \|\nabla \dot{w}^M\|^2_{\Omega_p} \leq \frac{\tau C_M}{2\nu_f} \sum_{n=0}^{M} \|\overline{\mathbf{f}_f^n}\|^2_{\Omega_f} \tag{13.0.12}$$

We multiply (13.0.5) by $\overline{\ddot{w}}^n$, integrate over Ω_p, and use Cauchy-Schwarz inequality to obtain,

$$\|\overline{\ddot{w}}^n\|^2_{\Omega_p} \leq \|\overline{u_3^n}\|_{\Omega_p} \|\overline{\ddot{w}}^n\|_{\Omega_p}.$$

Applying the trace theorem and Young's inequality, for some $C_T > 0$,

$$\|\overline{\ddot{w}}^n\|^2_{\Omega_p} \leq C_T \|\nabla \overline{\mathbf{u}}^n\|_{\Omega_f} \|\overline{\ddot{w}}^n\|_{\Omega_p} \leq \frac{C_T^2}{2} \|\nabla \overline{\mathbf{u}}^n\|^2_{\Omega_f} + \frac{1}{2} \|\overline{\ddot{w}}^n\|^2_{\Omega_p},$$

which implies

$$\|\overline{\ddot{w}}^n\|^2_{\Omega_p} \leq C_T^2 \|\nabla \overline{\mathbf{u}}^n\|^2_{\Omega_f}. \tag{13.0.13}$$

Next, multiply (13.0.4) with $w^n - w^{n-1}$, integrate over Ω_p and use Cauchy-Schwarz inequality.

$$\begin{aligned} \|w^n - w^{n-1}\|^2_{\Omega_p} &\leq \tau \|\overline{\dot{w}}^n\|_{\Omega_p} \|w^n - w^{n-1}\|_{\Omega_p}, \\ \implies \frac{1}{2} \|w^n - w^{n-1}\|^2_{\Omega_p} &\leq \frac{\tau^2}{2} \|\overline{\dot{w}}^n\|^2_{\Omega_p}, \\ \implies \frac{1}{2} \|w^n\|^2_{\Omega_p} - \frac{1}{2} \|w^{n-1}\|^2_{\Omega_p} &\leq \frac{\tau^2}{2} \|\overline{\dot{w}}^n\|^2_{\Omega_p}. \end{aligned} \tag{13.0.14}$$

Finally using (13.0.13) in (13.0.14), summing from $n = 0$ to $n = m$, where $m \in \{1, 2, \cdots, M\}$, we get

$$\|w^n\|^2_{\Omega_p} \leq (C_T \tau)^2 \sum_{n=0}^{m} \|\nabla \overline{\mathbf{u}}^n\|^2_{\Omega_f} \leq (C_T \tau)^2 \sum_{n=0}^{M} \|\nabla \overline{\mathbf{u}}^n\|^2_{\Omega_f}. \tag{13.0.15}$$

For the stability of p^n, we mimic the proof of the continuous case. We isolate the pressure term in (13.0.1), multiply with $\mathbf{u}^n$, integrate over Ω_f and divide by $\|\nabla \mathbf{v}\|_{\Omega_f}$ and take supremum over $\mathbf{v} \in \mathbf{U}$. Then, the inf-sup condition (2.1.1) yields that

$$\beta \|\overline{p}^n\|_{\Omega_f} \leq (1 + C_*)(\|\nabla \overline{\mathbf{u}}^n\|_{\Omega_f} + \|\overline{\mathbf{f}_f}^n\|_{\Omega_f} + \|\overline{g}^n\|_{H^{-1/2}(\Omega_p)}) \tag{13.0.16}$$

for some $\beta, C_* > 0$. Squaring on both sides of (13.0.16), using $(a+b+c)^2 \leq 3(a^2+b^2+c^2)$ on the right side and finally using (13.0.12), we get, for some $C_\beta > 0$,

$$\|\overline{p}^n\|^2_{\Omega_f} \leq C_\beta(\|\overline{\mathbf{f}_f}^n\|^2_{\Omega_f} + \|\overline{g}^n\|^2_{H^{-1/2}(\Omega_p)}) . \tag{13.0.17}$$

(13.0.17) now implies the stability of p^n. □

Chapter 14

Working algorithm and Numerical results

For the numerical simulation of the coupled fluid-plate system, we employ a partitioning method using fixed-point iteration. In this approach, we impose the condition $u_3 = w_t$ strongly as the Dirichlet condition for the fluid problem. Each time step begins with solving the fluid subproblem, where an initial guess for $\dot{w}$ is used, followed by solving the plate equation using the pressure. The fluid and the plate subsystem are solved serially and implicitly in time using iterations that terminate when the relative residual is smaller than a chosen tolerance. However, an issue arises when solving the subsystems separately using Dirichlet conditions. Because the pressure is not uniquely determined, an appropriate shifting method needs to be developed. Note that $\int_{\Omega_p} w_t \; d\Omega_p = \int_{\Omega_p} u_3 \; d\Omega_p = \int_{\partial\Omega_f} \mathbf{u} \cdot \mathbf{n}_f \; d(\partial\Omega_f) = 0$ due to the incompressibility condition $\nabla \cdot \mathbf{u} = 0$ [11]. This additional constraint can be incorporated into the plate system to determine the correct pressure. At the k-th fixed point iteration, the pressure, $\hat{p}$ is computed with the mean zero condition. Subsequently, the plate problem is solved for the additional unknown scalar value s with the pressure p replaced by $\hat{p} - s$ in (13.0.3) and the additional constraint equation $\int_{\Omega_p} \dot{w} \; d\Omega_p = 0$. Then $\hat{p} - s$ is expected to be the pressure satisfying (13.0.1)-(13.0.5) [90]. We summarize the complete numerical algorithm in Algorithm 2.

Algorithm 2: Working algorithm

Input: $\dot{w}$ initial guess, ϵ tolerance and N_{iter} maximum number of iteration.

Output: $\dot{w}^{n,k}$

$k = 0$, error $> \epsilon$, $\dot{w}^{0,0} = 0, \mathbf{u}^{0,0} = \mathbf{0}$

for $n = 1, 2, 3, \cdots, N$

while $k < N_{\text{iter}}$ and error $> \epsilon$, **do**

1. Solve for $(\mathbf{u}^{n,k}, \hat{p}^{n,k}) \in \mathbf{U} \times Q_0$ with $u_3^{n,k} = \dot{w}^{n,k-1}$:

$$\begin{aligned} \mathbf{u}^{n,k} - \nu_f \tau \Delta \overline{\mathbf{u}}^{n,k} + \tau \nabla \overline{\hat{p}}^{n,k} &= \tau \overline{\mathbf{f}}_f^{n,k} - \mathbf{u}^{n-1,k} \quad \text{in } \Omega_f\,, \\ \nabla \cdot\ \overline{\mathbf{u}}^{n,k} &= 0 \quad \text{in } \Omega_f\,, \\ \mathbf{u}^{n,k} &= \mathbf{0} \quad \text{on } S, \\ \mathbf{u}^{n,k} = [u_1^{n,k}, u_2^{n,k}, u_3^{n,k}] &= [0, 0, \dot{w}^{n,k-1}] \quad \text{on } \Omega_p, \\ \int_{\Omega_f} \hat{p}^{n,k}\, d\Omega_f &= 0. \end{aligned} \tag{14.0.1}$$

2. Solve for $(w^{n,k}, \dot{w}^{n,k}, s^{n,k})$ in $W \times W \times R$:

$$\begin{aligned} \dot{w}^{n,k} - \rho \Delta \dot{w}^{n,k} + \tau \Delta^2 \overline{w}^{n,k} &= \tau \left(\overline{\hat{p}}^{n,k}|_{\Omega_p} - s^{n,k} \right) + \dot{w}^{n-1,k} - \rho \Delta \dot{w}^{n-1,k} \quad \text{in } \Omega_p\,, \\ w^{n,k} - w^{n-1,k} &= \tau \overline{\dot{w}}^{n,k} \quad \text{in } \Omega_p\,, \\ \int_{\Omega_p} \dot{w}^{n,k}\, d\Omega_f &= 0, \\ w^{n,k} = \frac{\partial w^{n,k}}{\partial \nu} &= 0 \quad \text{on } \partial\Omega_p\,. \end{aligned} \tag{14.0.2}$$

3. Update $\dot{w}^{n,k-1} = \dot{w}^{n,k}$.

end while

Set $p^n = \hat{p}^{n,k} - s^{n,k}$

Reset $k = 0$.

end for

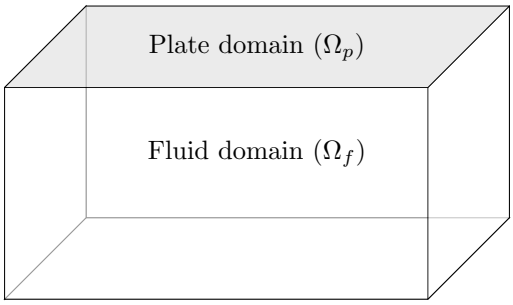

Figure 14.1: 3D Fluid and 2D plate system domain in $\mathbb{R}^3$

14.1 Numerical results

14.1.1 Test 1: Manufactured solutions

In this section, we introduce manufactured solutions for the fluid-plate system and illustrate the behavior of the method by performing the convergence with respect to space and comparing plots of finite element solution with the exact manufactured solution. All computations are performed using FreeFem++ [59]. We consider the domains $\Omega_f = [0,1]\times[0,1]\times[-1,0]$ and $\Omega_p = [0,1]\times[0,1]\times\{0\}$.

Further, the manufactured fluid velocity, pressure and displacement of the plate are considered as follows:

$$\begin{aligned}
u_1 &= (2x^3(x-1)^3(9x^2-9x+2)y^4(y-1)^4\,, \\
&\quad +(4/5)x^5(x-1)^5y^2(y-1)^2(14y^2-14y+3))(-30z^4-60z^3-30z^2)e^{-t}\,, \\
u_2 &= 0\,, \\
u_3 &= x^4(x-1)^4(2x-1)y^4(y-1)^4(-6z^5-15z^4-10z^3-1)e^{-t}\,, \\
p &= 0\,, \\
w &= x^4(x-1)^4(2x-1)y^4(y-1)^4e^{-t}.
\end{aligned}$$

Note that at $z=0, u_3 = w_t$. The right-hand side function $\mathbf{f}_f$ is evaluated using (11.0.1). For the finite elements simulation, we used $(\mathbf{P}_2, P_1, P_2\text{Morley}, P2)$ elements for $(\mathbf{u}, p, w, \dot{w})$. We set final time $T_{\text{final}} = 0.01$ and $\Delta t = 0.001$ and evaluated errors and convergence rates for different values of N (see table 14.1). We observed that the convergence rates are close to the theoretical convergence

rates [80]. Further, we plot and compare the finite element solution, w_t-FEM and u_3-FEM, with exact solutions, w_t-Exact and u_3-Exact in fig. 14.2 and fig. 14.3. The observation that both w_t and u_3 functions exhibit identical behavior in the plotted solutions indicates a strong agreement between the numerical model and the theoretical expectations.

h	$\mathbf{L}^2$(Velocity)	$\mathbf{H}^1$(Velocity)	L^2(pressure)
1/4	$1.77e-06$	$4.70e-05$	$6.58e-06$
1/6	$4.78e-04$[3.23]	$2.19e-05$[1.88]	$2.82e-06$[2.09]
1/8	$2.02e-07$[2.99]	$1.30e-05$[1.81]	$1.12e-06$[3.20]
1/10	$1.09e-07$[2.75]	$8.78e-06$[1.76]	$5.05e-07$[3.59]
1/12	$6.68e-08$[2.73]	$6.34e-06$[1.79]	$2.72e-07$[3.39]

Table 14.1: Errors and convergence rates for $\mathbf{u}$ and p functions at final time $T_{\text{final}} = 0.01$ using time-step size $\Delta t = 0.001$ for different values of h.

h	L^2(w-function)	H^1(w-function)	H^2(w-function)
1/4	$2.22e-07$	$3.13e-06$	$5.83e-05$
1/6	$8.49e-08$[2.37]	$1.40e-06$[1.99]	$4.25e-05$[0.78]
1/8	$3.28e-08$[3.31]	$7.33e-07$[2.24]	$3.15e-05$[1.04]
1/10	$2.06e-08$[2.09]	$4.87e-07$[1.83]	$2.59e-05$[0.88]
1/12	$1.48e-08$[1.80]	$3.17e-07$[2.36]	$2.10e-05$[1.16]]

Table 14.2: Errors and convergence rates for w function at final time $T_{\text{final}} = 0.01$ using time-step size $\Delta t = 0.001$ for different values of h.

While performing convergence tests in time, freefem++ did not allow us to set spatial mesh size smaller than $\frac{1}{13}$ as the problem becomes very large due to the involvement of 3D fluid equations. On using spatial mesh size $\frac{1}{12}$, we obtained that the errors evaluated for different time steps are very small; however, they are flat (see Table 14.3). We then solve only the 2D plate equation in the domain $[0,1]\times[0,1]$ using the exact solution and first-order time discretization and observed similar flat errors. This issue was addressed, and we could achieve linear convergence in time using a very large weight (10^5) in the w_{tt} term of the structure equation for spatial mesh size $\frac{1}{50}$ (see Table 14.4). With the weight the structure problem is defined as follows:

$$(\text{weight})w_{tt} - \rho\Delta w_{tt} + \Delta^2 w = f_p,$$

where f_p is the function evaluated using manufactured w function. Another interesting point we

noticed was the need for an even larger weight to achieve linear convergence in time with a smaller mesh size. This numerical finding suggests that errors are strongly dependent on a spatial mesh. However, the restriction of not being able to use a mesh finer than $\frac{1}{13}$ throughout the entire three-dimensional domain limited us from observing convergence in time.

Type	Error
L^2(w-function)	$1.90e-07$
H^2(w-function)	$1.65e-06$
H^2(w-function)	$2.45e-05$

Table 14.3: Flat errors for w function at final time $T_{\text{final}} = 0.2$ using mesh size $\frac{1}{12}$ using $\Delta t = \{0.2, 0.1, 0.05, 0.025\}$.

Δt	L^2(w-function)
0.5	$1.43e-06$
0.25	$6.97e-07$[1.04]
0.125	$3.45e-07$[1.01]
0.0625	$1.73e-07$[1.00]
0.03125	$8.75e-08$[0.99]

Table 14.4: L^2 errors and convergence rates for w function at final time $T_{\text{final}} = 4$ using mesh size $\frac{1}{50}$ for different values of Δt while solving only 2D structure problem with weight 10^5.

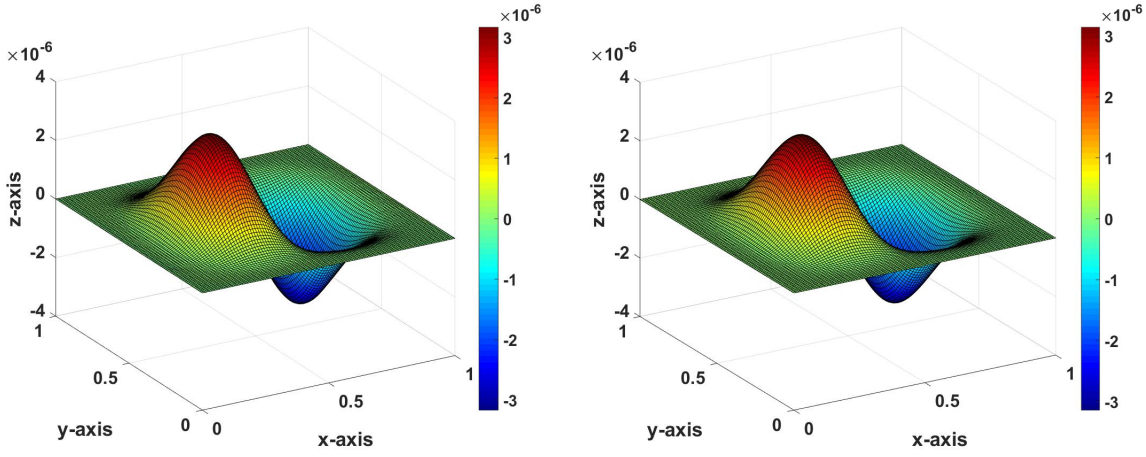

Figure 14.2: w_t-FEM (left) and w_t-Exact (right) for $h = 1/12$, $T_{\text{final}} = 0.01, \Delta t = 0.001$.

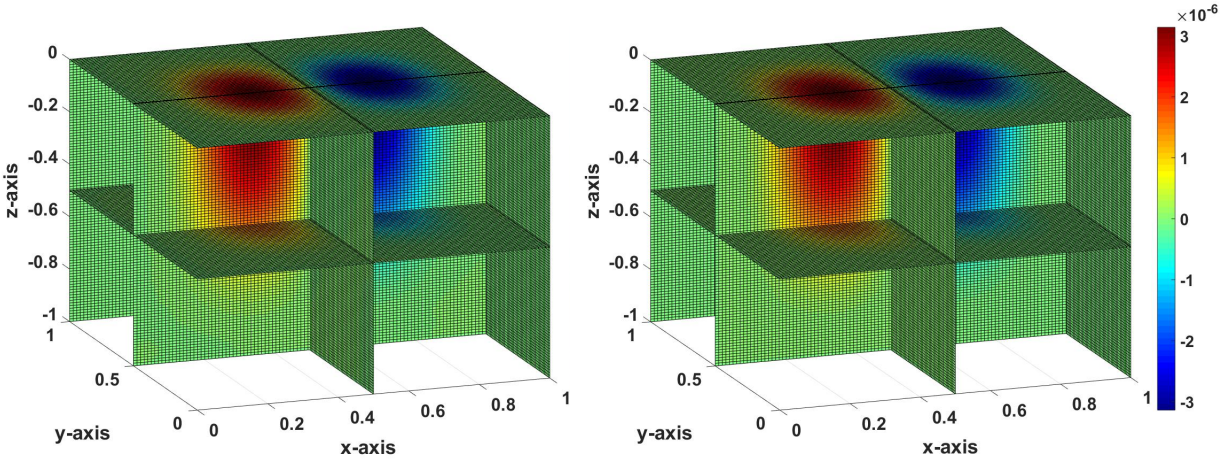

Figure 14.3: u_3-FEM (left) and u_3-Exact (right) for $h = 1/12$, $T_{\text{final}} = 0.01, \Delta t = 0.001$.

14.1.2 Test 2: Free vibration of a plate

In this test, we examine a physical scenario involving the free vibration of a plate [34]. Consider the domains $\Omega_f = [0,1] \times [0,1] \times [-1,0]$ and $\Omega_p = [0,1] \times [0,1] \times \{0\}$, set $\mathbf{f}_f = 0$ and impose $\mathbf{u} = \mathbf{0}$ on all boundary faces of Ω_f, except at $z = 0$, where we have the condition $u_3 = w_t$. Additionally, at the boundary of the plate we set $w = \frac{\partial w}{\partial \mathbf{n}} = \frac{\partial w}{\partial t} = 0$. We use additional parameters and rewrite the plate structure as follows:

$$\rho_p w_{tt} - \rho \Delta w_{tt} + D\Delta^2 w = f_p \quad \text{in } \Omega_p \times (0,T),$$

where ρ_p is the density, $D := Yh^3/(12(1-\nu))$ is the flexural rigidity with ν and Y being the Poisson's ratio and Young's modulus, respectively. In this experiment we consider $\rho_p = 2.7, D = 6.4527$ and $\rho = 0$. By setting $D \neq 0$ and $f_p = \rho = 0$, the model reduces to the classical Kirchhoff-Love model with only the bending dynamics accounted. For the numerical experiment, we set mesh size $h = 1/12$, $T_{\text{final}} = 0.01$ seconds and $\tau = 0.001$ seconds. Initially, we set $\mathbf{u}(\mathbf{x}, 0) = \mathbf{0}, p(\mathbf{x}, 0) = 0$ and set the plate in the free vibration by introducing, for some integers m and n,

$$w_t(\mathbf{x}, 0) = \sin(m\pi x) \sin(n\pi y).$$

We plot u_3 in the fluid domain and w_t in the plate domain for different values of m and n. The plots show that the vibration in the plate gets transmitted to the fluid dynamics, affecting the vertical velocity component of the fluid (u_3). Furthermore, we observed that the plot of w_t is the same as the standing wave solution mentioned in [34]. We also present the plot of u_3 for the $(m, n) = (1, 2)$ case on the $x = 0.5$ plane (see Figure 14.4), which provides a clearer representation of u_3 in the fluid domain.

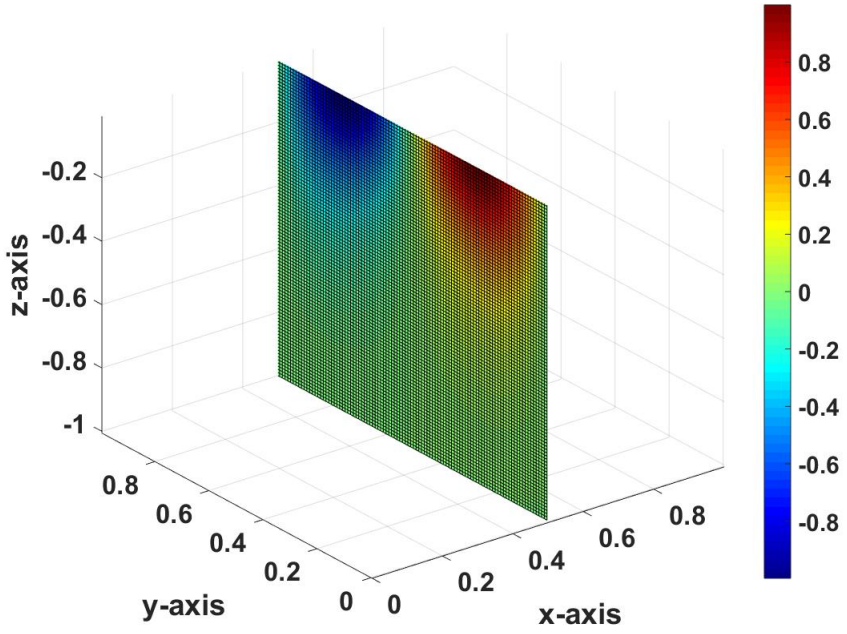

Figure 14.4: u_3 for $h = 1/12$, $T_{\text{final}} = 0.01, \tau = 0.001$ in $x = 0.5$ plane.

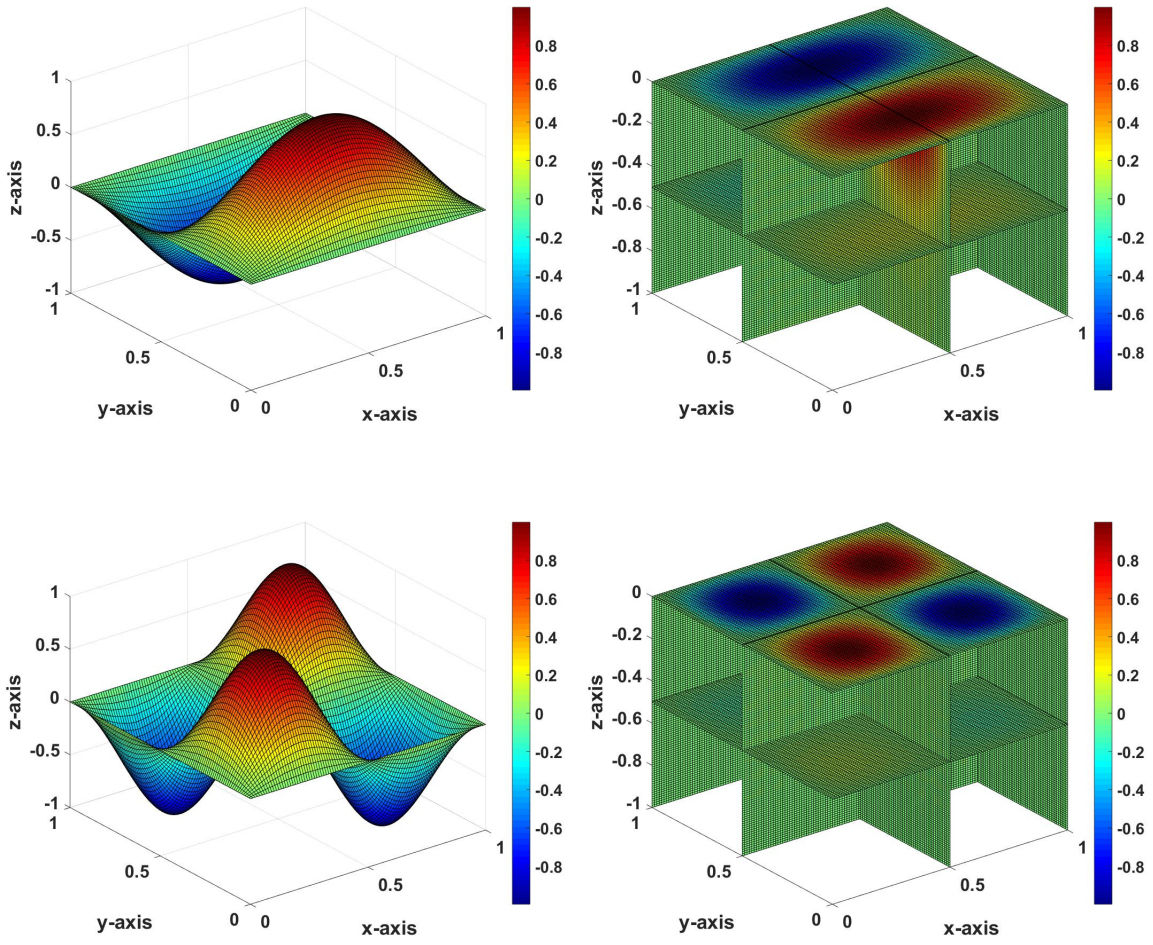

Figure 14.5: w_t(left) and u_3(right) for $h = 1/12$, $T_{\text{final}} = 0.01, \tau = 0.001$, $(m, n) = (1, 2)$ (top) and $(m, n) = (2, 2)$ (bottom).

Chapter 15

Conclusions

We introduced global-in-time domain decomposition methods for fluid-structure interaction problems involving elastic, porous, or poroelastic structure by formulating two interface problems, based on the Steklov-Poincaré operator and Robin transmission conditions, respectively. In these methods, the fluid and the structure subproblems are time-dependent and solved independently using local solvers. This allows for the use of nonconforming time grids and different time-stepping algorithms for local problems.

For the case where the elastic structure is involved, we implemented both methods. The SWR algorithm was introduced and analyzed in continuous and semi-discrete settings. We performed numerical tests on two examples. First including a non-physical problem where we tested with various mesh sizes and time steps to verify convergence rates. The use of non-conforming time grids resulted in better accuracy within similar computational times compared to results obtained using conforming coarse grids. Secondly, for the physical benchmark problem from a hemodynamic application, we implemented the Steklov-Poincaré method and observed similar results reported in the literature.

In the problem involving porous structure, we investigated the Robin method. This approach can easily handle problems with discontinuous media represented by model equations with discontinuous coefficients. Also, problems with a large difference in local time scales, e.g., low permeability in the porous region, can be efficiently solved by the method. In our numerical tests, we observed that using nonconforming time grids significantly improves the efficiency, still yielding the desired accuracy. The robustness of this global-in-time DD approach was also partially verified while

being tested on the test case of low permeability porous medium. However, it was noticed that the Darcy velocity among all variables is most sensitive to a choice of Robin parameters for its accuracy. A theoretical framework for the optimal choice of Robin parameters in the SWR method has not been established for time-dependent multiphysics problems; therefore, the parameters used for the presented numerical results were chosen completely based on numerical experiments. For the method to be practical and more robust, further studies are needed for Robin transmission conditions about the convergence of iterative schemes and the accuracy of numerical solutions.

Finally, we implemented Steklov-Poincare to the nonlinear fluid-poroelastic interaction system. The scheme is an implicit type that requires iterations between fluid and poroelastic subsystems. We performed numerical tests on three kinds of problems. First, we used a manufactured solution and tested the convergence behavior of the algorithm with respect to space and time. Secondly, we chose a problem from hemodynamic application and observed the propagation of pressure in the artery. Finally, we considered a problem from a geoscience application and performed sensitivity analysis by varying physical parameters of Biot equations. Numerical results show that the algorithm efficiently simulates the model problem, preserving accuracy.

Using local time stepping makes our research approach efficiently applicable to multiphysics problems, where local problems are in different time scales. As a future work, this method can be extended to other multiphysics problems that include cases where more than two subdomains need to be considered, fractured models. Further, the theoretical framework that explains topics such as the relation between Robin parameters and convergence of SWR algorithm, and the choice of optimal Robin parameters can be studied. The work can also be extended to the multiphysics problems that involve moving domain settings where time-dependent domains are considered and time-dependent bijective mapping, known as arbitrary Lagrangian–Eulerian (ALE) mapping is used to exchange information between fixed reference domain and physical domain.

Additionally, we presented a temporal numerical discretization scheme for the 3D fluid - 2D plate structure interaction system and showed the stability of this scheme. We proposed a numerical algorithm that sequentially solves the fluid and plate subsystems through an effective decoupling approach. The numerical complexity due to the presence of the biharmonic operator in plate structure is handled using $P2$Morley elements in the structure subproblem. The numerical results presented for the test that uses time-dependent manufactured solutions and the test that considers the free vibration of the plate showed the performance of the algorithm.

Bibliography

[1] I. Ambartsumyan, V. J. Ervin, T. Nguyen, and I. Yotov. A nonlinear Stokes-Biot model for the interaction of a non-newtonian fluid with poroelastic media. *arXiv*, page 1803.00947, 2019.

[2] I. Ambartsumyan, E. Khattatov, I. Yotov, and P. Zunino. A lagrange multiplier method for a Stokes-Biot fluid-poroelastic structure interaction model. *Numerische Mathematik*, 140:513–553, 2018.

[3] T. Arbogast and D.S. Brunson. A computational method for approximating a Darcy–Stokes system governing a vuggy porous medium. *Comput.Geosci.*, 11:207–218, 2007.

[4] T. Arbogast and M. Gomez. A discretization and multi grid solver for a Darcy–Stokes system governing a vuggy porous medium. *Comput.Geosci.*, 13:331–348, 2009.

[5] G. Avalos and T. Clark. Mixed variational formulation for the wellposedness and numerical approximation of a pde model arising in a 3-d fluid-structure interaction. *Evolution Equations and Control Theory*, 3:557, 2014.

[6] F.P.T. Baaijens. A fictitious domain/mortar element method for fluid-structure interaction. *Int. J. Numer. Methods Fluids*, 35:743–761, 2001.

[7] I. Babuska and G.N. Gatica. A residual-based a posteriori error estimator for the Stokes-Darcy coupled problem. *SIAM J. Numer. Anal.*, 48:498–523, 2010.

[8] S. Badia, A. Quaini, and A. Quarteroni. Splitting methods based on algebraic factorization for fluid-structure interaction. *SIAM Journal on Scientific Computing*, 30:1778–1805, 2008.

[9] S. Badia, A. Quaini, and A. Quateroni. Coupling Biot and Navier-Stokes equations for modeling fluid-poroelastic media interaction. *Journal of Computational Physics*, 228:7986–8014, 2009.

[10] F. Ballarin, G. Rozza, and Y. Maday. Reduced-order semi-implicit schemes for fluid-structure interaction problems in model reduction of parameterized systems. *Springer*, pages 149–167, 2017.

[11] Y. Bazilevs, V. M. Calo, T.J.R. Hughes, and Y. Zhang. Isogeometric fluid-structure interaction: theory, algorithms, and computations. *Computational Mechanics*, 43:3–37, 2008.

[12] J. Bear. In *Dynamics of fluids in porous media*. Dover Publications, 1988.

[13] E.A. Bergkamp, C.V. Verhoosel, J.J.C. Remmers, and D.M.J. Smeulders. A staggered finite element procedure for the coupled Stokes-Biot system with fluid entry resistance. *Comput. Geosci.*, 24:1497–1522, 2020.

[14] C. Bernardi, T.C. Rebollo, F. Hecht, and Z. Mghazli. Mortar finite element discretization of a model coupling Darcy and Stokes equations. *Math. Model. Numer. Anal*, 42:375–410, 2008.

[15] D. Boffi and L. Gastaldi. A fictitious domain approach with lagrange multiplier for fluid-structure interactions. *Numer. Math.*, 135:711–732, 2017.

[16] Y. Boubendir and S. Tlupova. Stokes-Darcy boundary integral solutions using preconditioners. *J. Comput. Phys.*, 228:8627–8641, 2009.

[17] J. Boujot. Mathematical formulation of fluid–structure interaction problems. *Modelisation Math´ematique et Analyse Numerique*, 21:239–260, 1987.

[18] M. Bukac, W. Layton, M. Moraiti, H. Tran, and C. Trenchea. Analysis of partitioned methods for the Biot system. *Numerical Methods for Partial Differential Equations*, 31:1769–1813, 2015.

[19] M. Bukac, I. Yotov, R. Zakerzadeh, and P. Zunino. Partitioning strategies for the interaction of a fluid with a poroelastic material based on a nitsche's coupling approach. *Computer Methods in Applied Mechanics and Engineering*, 292:138–170, 2015.

[20] E. Burman, R. Durst, and J. Guzmán. Stability and error analysis of a splitting method using robin–robin coupling applied to a fluid-structure interaction problem. *Numer. Methods Partial Differ. Eq.*, 38:1396–1406, 2022.

[21] E. Burman, R. Durst, A. Fernández M, and J. Guzmán. Fully discrete loosely coupled robin-robin scheme for incompressible fluid–structure interaction: stability and error analysis. *Numer. Math.*, 151:807–840, 2022.

[22] E. Burman and M.A. Fernandez. Stabilization of explicit coupling in fluid-structure interaction involving fluid incompressibility. *Computer Methods in Applied Mechanics and Engineering*, 198:766–784, 2009.

[23] M. Cai, M. Mu, and J. Xu. Numerical solution to a mixed Navier–Stokes/Darcy model by the two-grid approach. *SIAM J. Numer. Anal.*, 47:3325–3338, 2009.

[24] V.M. Calo, N.F. Brasher, Y.Bazilevs, and T.J.R. Hughes. Multiphysics model for blood flow and drug transport with application to patient-specific coronary artery flow. *Comput. Mech.*, 43:161–177, 2008.

[25] S. Canic, A. Mikelic, and J. Tambaca. A two-dimensional effective model describing fluid–structure interaction in blood flow: analysis, simulation and experimental validation. *Comptes Rendus Mécanique*, 333:867–883, 2005.

[26] Y. Cao, M. Gunzburger, X. He, and X. Wang. Robin–robin domain decomposition methods for the steady-state Stokes–Darcy system with the beavers–joseph interface condition. *Numer. Math.*, 117:601–629, 2011.

[27] Y. Cao, M. Gunzburger, X. He, and X. Wang. Parallel, non-iterative, multi-physics domain decomposition methods for time-dependent Stokes-Darcy systems. *Math. Comput.*, 83:1617–1644, 2014.

[28] S. Caucao, T. Li, and I. Yotov. A multipoint stress-flux mixed finite element method for the Stokes-Biot model. *Numer. Math.*, 152:411–473, 2022.

[29] A. Celik and M. Kyed. Fluid-plate interaction under periodic forcing. *arXiv*, page 2103.00795, 2021.

[30] A. Cesmelioglu. Analysis of the coupled Navier Stokes/Biot problem. *J. Math. Anal. Appl.*, 456:970–991, 2017.

[31] A. Cesmelioglu, H. Lee, A. Quaini, K. Wang, and S.Y. Yi. Optimization-based decoupling algorithms for fluid-poroelastic system. *In Topics in Numerical Partial Differential Equations and Scientific Computing*, 160:137–176, 2016.

[32] A. Cesmelioglu and B. Riviere. Primal discontinuous galerkin methods for time dependent coupled surface and subsurface flow. *J. Sci. Comput.*, 40:115–140, 2009.

[33] W. Chen, M. Gunzburger, F. Hua, and X. Wang. A parallel robin-robin domain decomposition method for the Stokes-Darcy system. *SIAM J. Numer. Anal.*, 49:1064–1084, 2011.

[34] J. Chrispell and L. Fauci. Peristaltic pumping of solid particles immersed in a viscoelastic fluid. *Mathematical Modelling of Natural Phenomena*, 6:67–83, 2011.

[35] I. Chueshov and I. Ryzhkova. A global attractor for a fluid-plate interaction model. *Communications on Pure and Applied Analysis*, 12:1635–1656, 2013.

[36] M.M. Dehkordi. A fully coupled porous media and channels flow approach for simulation of blood and bile flow through the liver lobules. *Comput. Methods Biomech. Biomed. Engin.*, 22:901–915, 2019.

[37] M. Discacciati. *Domain decomposition methods for the coupling of surface and ground- water-flows*. PhD thesis, Ecole Polytechnique Federale de Lausanne, 2004.

[38] M. Discacciati and L. Gerardo-Giorda. Optimized schwarz methods for the Stokes–Darcy coupling. *IMA J. Numer. Anal.*, 38:1959–1983, 2018.

[39] M. Discacciati, E. Miglio, and A. Quarteroni. Mathematical and numerical models for coupling surface and groundwater flows. *Appl. Numer. Math.*, 43:57–74, 2002.

[40] M. Discacciati, A. Quarteroni, and A. Valli. Robin-robin domain decomposition methods for the Stokes–Darcy coupling. *SIAM J. Numer. Anal.*, 45:1246–1268, 2007.

[41] V.J. Ervin, E.W. Jenkins, and H. Lee. Approximation of the Stokes-Darcy system by optimization. *J. Sci. Comput.*, 59:775–794, 2014.

[42] V.J. Ervin, E.W. Jenkins, and S. Sun. Coupled generalized nonlinear Stokes flow with flow through a porous medium. *SIAM J. Numer. Anal.*, 47:929–952, 2009.

[43] M. Fernandez. Coupling schemes for incompressible fluid-structure interaction: implicit, semi-implicit and explicit. *SeMA Journal: Boletin de la Sociedad Española de Matem'atica Aplicada*, 55:59–108, 2011.

[44] M. Fernandez, J. Gerbeau, and C. Grandmont. A projection semi-implicit scheme for the coupling of an elastic structure with an incompressible fluid. *INRIA Technical Report RR-5700*, 2005.

[45] J.A. Fiordilino. On pressure estimates for the Navier-Stokes equations. https://arxiv.org/abs/1803.04366, 2018.

[46] D. Gallistl. Morley finite element method for the eigenvalues of the biharmonic operator. *arXiv*, page 1406.2876, 2014.

[47] J. Galvis and M. Sarkis. Feti and bdd preconditioners for Stokes-mortar-Darcy systems. *Comm. App. Math. Comp. Sci.*, 5:1–30, 2010.

[48] M.J. Gander, L. Halpern, and F. Nataf. Optimal schwarz waveform relaxation for the one dimensional wave equation. *SIAM J. Numer. Anal.*, 41:1643–1681, 2003.

[49] M.J. Gander and T. Vanzan. On the derivation of optimized transmission conditions for the Stokes-Darcy coupling. in: Haynes r. et al., editor. *Domain Decomposition Methods in Science and Engineering XXV. DD 2018*, 2020.

[50] B. Ganis, R. Liu, B. Wang, M.F. Wheeler, and I. Yotov. Multiscale modeling of flow and geomechanics. *Radon Series on Computational and Applied Mathematics*, pages 165–204, 2013.

[51] B. Ganis, D. Vassilev, C. Wang, and I. Yotov. A multiscale flux basis for mortar mixed discretizations of Stokes-Darcy flows. *Comput. Methods Appl. Mech. Engrg.*, 313:259–278, 2017.

[52] G.N. Gatica, S. Meddahi, and R. Oyarzua. A conforming mixed finite element method for the coupling of fluid flow with porous media flow. *IMA J. Numer. Anal.*, 29:86–108, 2009.

[53] K.J. Gavin. New subgrid artificial viscosity galerkin methods for the Navier-Stokes equations. *Comput. Methods Appl. Mech. Engrg.*, 200:242–250, 2011.

[54] G. Gigante and C. Vergara. On the choice of interface parameters in robin–robin loosely coupled schemes for fluid–structure interaction. *Fluids*, 6:213, 2021.

[55] L. Guo and W. Chen. Decoupled modified characteristic finite element method for the time-dependent Navier–Stokes/Biot problem. *Numerical Methods for Partial Differential Equations*, 38:1684–1712, 2021.

[56] L. Guo and W. Chen. A decoupled stabilized finite element method for the time–dependent Navier–Stokes/Biot problem. *Mathematical Methods in the Applied Sciences*, 17:10749–10774, 2022.

[57] N.S. Hanspal, A.N. Waghode, V. Nassehi, and R.J. Wakeman. Numerical analysis of coupled Stokes/Darcy flows in industrial filtrations. *Transp. Porous Media*, 64:1573–1634, 2006.

[58] N. Haritos. Introduction to the analysis and design of offshore structures – an overview. *Electronic Journal of Structural Engineering*, 7:55–65, 2007.

[59] F. Hecht. New development in freefem++. *J. Numer. Math.*, 20:251–265, 2012.

[60] M. Heil. An efficient solver for the fully coupled solution of large-displacement fluid–structure interaction problems. *Comput. Methods Appl. Mech. Eng.*, 193:1–23, 2004.

[61] C. Hesch, A.J. Gil, A. Carreno, J. Bonet, and P. Betsch. A mortar approach for fluid-structure interaction problems: Immersed strategies for deformable and rigid bodies. *Comput. Methods Appl. Mech. Eng.*, 278:853–882, 2014.

[62] J. J. Heys, T. A. Manteuffel, S. F. McCormick, and J.W. Ruge. First order system least squares (fosls) for coupled fluid–elastic problems. *Journal of Computational Physics*, 195:560–575, 2004.

[63] T.T.P. Hoang, J. Jaffré, C. Japhet, M. Kern, and J.E. Roberts. Space-time domain decomposition methods for diffusion problems in mixed formulations. *SIAM J. Numer. Anal.*, 51:3532–3559, 2013.

[64] T.T.P. Hoang, J. Jaffre, C. Japhet, M. Kern, and J.E. Roberts. Space-time domain decomposition methods for diffusion problems in mixed formulations. *SIAM J. Numer.Anal.*, 51:3532–3559, 2013.

[65] T.T.P. Hoang, C. Japhet, M. Kern, and J.E. Roberts. Space-time domain decomposition for reduced fracture models in mixed formulation. *SIAM J. Numer. Anal.*, 54:288–316, 2016.

[66] T.T.P. Hoang, H. Kunwar, and H. Lee. Nonconforming time discretization based on robin transmission conditions for the Stokes–Darcy system. *Applied Mathematics and Computation*, 413:126602, 2022.

[67] T.T.P. Hoang and H. Lee. A global-in-time domain decomposition method for the coupled nonlinear Stokes and Darcy flows. *J. Sci. Comput.*, 87, 2021.

[68] J. Hron and S. Turek. A monolithic fem/multigrid solver for an ale formulation of fluid-structure interaction with applications in biomechanics, in fluid-structure interaction. *Springer*, pages 146–170, 2006.

[69] W. Jager and A. Mikelic. On the interface boundary condition of beaver, joseph and saffman. *SIAM J. Appl. Math.*, 60:1111–1127, 2000.

[70] M. Jayadharan, M. Kern, M. Vohralík, and I. Yotov. A space-time multiscale mortar mixed finite element method for parabolic equations. *SIAM Journal on Numerical Analysis*, 61:675–706, 2023.

[71] R. Kamakoti and W. Shyy. Fluid–structure interaction for aeroelastic applications. *Progress in Aerospace Sciences*, 40:535–558, 2004.

[72] M. Kubacki and M. Moraiti. Analysis of a second-order, unconditionally stable, partitioned method for the evolutionary Stokes-Darcy model. *Int. J. Numer. Anal. Model.*, 12:704–730, 2015.

[73] P. Kuberry and H. Lee. A decoupling algorithm for fluid–structure interaction problems based on optimization. *Comput. Methods Appl. Mech. Engrg.*, 267:594–605, 2013.

[74] H. Kunwar, H. Lee, and K. Seelman. Second-order time discretization for a coupled quasi-newtonian fluid-poroelastic system. *Internat. J. Numer. Methods Fluids*, 92:687–702, 2020.

[75] W.J. Layton, F. Schieweck, and I. Yotov. Coupling fluid flow with porous media flow. *SIAM J. Numer. Anal.*, 40:2195–2218, 2003.

[76] M. Li, X Guan, and S Mao. New error estimates of the morley element for the plate bending problems. *J Comput Appl Math*, 263:405–416, 2014.

[77] T. Li, S. Caucao, and I. Yotov. An augmented fully mixed formulation for the quasistatic Navier–Stokes–Biot model. *IMA Journal of Numerical Analysis*, 2023.

[78] T. Li and I. Yotov. A mixed elasticity formulation for fluid–poroelastic structure interaction. *ESAIM: Mathematical Modelling and Numerical Analysis*, 56:1–40, 2022.

[79] R.V. Loon, P.D. Anderson, J. de Hart, and F.P.T Baaijens. A combined fictitious domain/adaptive meshing method for fluid-structure interaction in heart valves. *Int J. Numer. Methods Fluids*, 46:533–544, 2004.

[80] S. Mao, S. Nicaise, and C.Z. Shi. Error estimates of morley triangular element satisfying the maximal angle condition. *International Journal of Numerical Analysis and Modeling*, 7(4):639–655, 2010.

[81] M. Mayr, T. Klöppel, W.A. Wall, and M.W. Gee. A temporal consistent monolithic approach to fluid–structure interaction enabling single field predictors. *SIAM J. Sci. Comput.*, 37:30–59, 2015.

[82] M. Mayr, M.H. Noll, and M.W. Gee. A hybrid interface preconditioner for monolithic fluid-structure interaction solvers. *Adv. Model Simul. Eng. Sci.*, 7:1–33, 2020.

[83] W. Ming and J. Xu. The morley element for fourth order elliptic equations in any dimensions. *Numer Math*, 103:155–169, 2006.

[84] L.S.D. Morley. The triangular equilibrium element in the solution of plate bending problems. *Aero Q*, 19:149–169, 1968.

[85] M. Mu and J. Xu. A two-grid method of a mixed Stokes-Darcy model for coupling fluid flow with porous media flow. *SIAM J. Numer. Anal.*, 45:1801–1813, 2007.

[86] M. Mu and X. Zhu. Decoupled schemes for a non-stationary mixed Stokes-Darcy model. *Math. Comput.*, 79:707–73, 2010.

[87] M. A. Murad, J. N. Guerreiro, and A. F. D. Loula. Micromechanical computational modeling of secondary consolidation and hereditary creep in soils. *Comput. Methods. Appl. Mech. Engrg.*, 190:1985–2016, 2001.

[88] C.M. Murea and S. Sy. A fast method for solving fluid-structure interaction problems numerically. *International Journal for Numerical Methods in Fluids*, 60:1149–1172, 2009.

[89] N.Koshiba, J.Ando, X.Chen, and T.Hisada. Multiphysics simulation of blood flow and LDL transport in a porohyperelastic arterial wall model. *J. of Biomech. Eng.*, 129:374–385, 2007.

[90] F. Nobile. *Numerical approximation of fluid-structure interaction problems with application to haemodynamics*. PhD thesis, EPFL. Switzerland, 2001.

[91] F. Nobile and C. Vergara. An effective fluid-structure interaction formulation for vascular dynamics by generalized robin conditions. *SIAM Journal on Scientific Computing*, 30:731–763, 2008.

[92] M. Nonino, F. Ballarin, and G. Rozza. A monolithic and a partitioned, reduced basis method for fluid–structure interaction problems. *Fluids*, 6:229–263, 2021.

[93] J.R. Ramirez. *Time-dependent Stokes-Darcy flow with deposition*. PhD thesis, Clemson University, 2017.

[94] K. Rife and H. Lee. Least squares approach for the time-dependent nonlinear Stokes-Darcy system. *Comput. Math. Appl.*, 67:1806–1815, 2014.

[95] B. Riviere. Analysis of a discontinuous finite element method for the coupled Stokes and Darcy problems. *J. Sci. Comput.*, 22:479–500, 2005.

[96] R. Ruiz-Baier, M. Taffetani, H.D. Westermeyer, and I. Yotov. The Biot-Stokes coupling using total pressure: formulation, analysis and application to interfacial flow in the eye. *Comput. Methods Appl. Mech. Eng.*, 389:e114384, 2022.

[97] L. Shan, H. Zheng, and W.J. Layton. A decoupling method with different sub-domain time steps for the nonstationary Stokes-Darcy model. *Numer. Methods Partial Differ. Equ.*, 29:549–583, 2013.

[98] J.P. Sheldon, S.T. Miller, and J.S. Pitt. A hybridizable discontinuous galerkin method for modeling fluid–structure interaction. *J. Comput. Phys.*, 326:91–114, 2016.

[99] P. Tallec and S. Mani. Numerical analysis of a linearised fluid-structure interaction problem. *Numerische Mathematik*, 87:317–354, 2000.

[100] S. Tlupova and R. Cortez. Boundary integral solutions of coupled Stokes and Darcy flows. *J. Comput. Phys.*, 228:158–179, 2009.

[101] B. Tully and Y.Ventikos. Coupling poroelasticity and cfd for cerebrospinal fluid hydrodynamics. *IEEE Transactions on Biomedical Engineering*, 56(6):1644–1651, 2009.

[102] X. Wang and H. Rui. A semi-decoupled mac scheme for the coupled fluid-poroelastic material interaction. *Computers and Mathematics with Applications*, 139:118–135, 2023.

[103] X. Wang, Y. Zhang, and H. Rui. A stable pressure-correction mac scheme for the fluid-poroelastic material interaction problem. *International Journal of Computer Mathematics*, 100:1683–1701, 2023.

[104] H.K. Wilfrid. Nonconforming finite element methods for a Stokes/Biot fluid–poroelastic structure interaction model. *Results Appl. Math.*, 7:100–127, 2020.